

THE ANALYSIS OF CURRENT AND FUTURE CLIMATE PROJECTIONS OF
TÜRKİYE AND THE LARGE-SCALE EASTERN MEDITERRANEAN BLACK
SEA REGION IN THE COARSE AND HIGH RESOLUTIONS

A THESIS SUBMITTED TO
THE GRADUATE SCHOOL OF NATURAL AND APPLIED SCIENCES
OF
MIDDLE EAST TECHNICAL UNIVERSITY

BY

SONER ÇAĞATAY BAĞÇACI

IN PARTIAL FULFILLMENT OF THE REQUIREMENTS
FOR
THE DEGREE OF DOCTOR OF PHILOSOPHY
IN
CIVIL ENGINEERING

MARCH 2023

Approval of the thesis:

**THE ANALYSIS OF CURRENT AND FUTURE CLIMATE PROJECTIONS
OF TÜRKİYE AND THE LARGE-SCALE EASTERN MEDITERRANEAN
BLACK SEA REGION IN THE COARSE AND HIGH RESOLUTIONS**

submitted by **SONER ÇAĞATAY BAĞÇACI** in partial fulfillment of the requirements for the degree of **Doctor of Philosophy in Civil Engineering, Middle East Technical University** by,

Prof. Dr. Halil Kalıpçılar
Dean, Graduate School of **Natural and Applied Sciences** _____

Prof. Dr. Erdem Canbay
Head of the Department, **Civil Engineering** _____

Prof. Dr. İsmail Yücel
Supervisor, **Civil Engineering, METU** _____

Examining Committee Members:

Assoc. Prof. Dr. Mustafa Tuğrul Yılmaz
Civil Engineering, METU _____

Prof. Dr. İsmail Yücel
Civil Engineering, METU _____

Assoc. Prof. Dr. Koray Kamil Yılmaz
Geological Engineering, METU _____

Prof. Dr. Ömer Lütfi Şen
Climate and Marine Sciences, Istanbul Technical University _____

Prof. Dr. Nermin Şarлак
Civil Engineering, Konya Technical University _____

Date: 03.03.2023

I hereby declare that all information in this document has been obtained and presented in accordance with academic rules and ethical conduct. I also declare that, as required by these rules and conduct, I have fully cited and referenced all material and results that are not original to this work.

Name Last name : Soner aęatay Baęcacı

Signature :

ABSTRACT

THE ANALYSIS OF CURRENT AND FUTURE CLIMATE PROJECTIONS OF TÜRKİYE AND THE LARGE-SCALE EASTERN MEDITERRANEAN BLACK SEA REGION IN THE COARSE AND HIGH RESOLUTIONS

Bağcı, Soner Çağatay
Doctor of Philosophy, Civil Engineering
Supervisor : Prof. Dr. İsmail Yücel

March 2023, 116 pages

This thesis mainly focuses on climatic change over Türkiye and the Eastern Mediterranean Black Sea (EMBS) region with three-legged studies utilizing cutting-edge global climate models (GCMs) and reanalysis. The first study unfolds the future projections of Türkiye under the medium and high emission scenarios by the latest Coupled Model Intercomparison Project Phase 6 (CMIP6) GCMs. The second study conducts sensitivity tests with a 60-model physics combination of the Weather Research and Forecasting (WRF) model over Türkiye for 2020. The final study utilizes the Pseudo Global Warming (PGW) approach to dynamically downscale the CMIP6 GCMs ensemble under the high-emission range to a high resolution (4 km) over the EMBS. The main findings show that winter precipitation is expected to decrease over Türkiye's southwest and increase over Türkiye's northeast, all of which are statistically significant under both scenarios. On the other hand, convectivity caused by warmer projections under the high-emission scenario partly offset summer precipitation decrease over Türkiye. The daily precipitation correlation values are between 0.5 and 0.65 in the sensitivity study, which range was improved in the long-term simulations. The WRF model perfectly captured the winter and spring

precipitation anomalies and large-scale low-level circulation anomalies over the EMBS in whole seasons. The heat-low development in summer and its trace in fall were also generally well captured by WRF. However, the main contradiction appears especially in summer precipitation anomalies over the Caucasus and nearby regions, which was discussed with the additional simulation by reasoning the sea-surface temperature anomalies of the Caspian Sea.

Keywords: Coupled Model Intercomparison Project Phase 6, Global Climate Model, Eastern Mediterranean Black Sea Region, Pseudo Global Warming, Weather Research and Forecast Model

ÖZ

TÜRKİYE VE GENİŞ ÖLÇEKTE DOĞU AKDENİZ KARADENİZ BÖLGESİNİN KABA VE YÜKSEK ÇÖZÜNÜRÜLÜKLERDEKİ MEVCUT VE GELECEK İKLİM PROJEKSİYONLARININ ANALİZİ

Bağcı, Soner Çağatay
Doktora, İnşaat Mühendisliği
Tez Yöneticisi: Prof. Dr. İsmail Yücel

Mart 2023, 116 sayfa

Bu tez temel olarak, son teknoloji küresel iklim modelleri (GCM'ler) ve yeniden analiz verileri kullanan üç ayaklı çalışmalarla Türkiye ve Doğu Akdeniz Karadeniz (EMBS) bölgesindeki iklim değişikliğine odaklanmaktadır. İlk çalışma, en son çıkan Akuple Model Karşılaştırma Projesi Aşama 6 (CMIP6) GCM'lerinin orta ve yüksek emisyon senaryolar altında Türkiye'ye yönelik gelecek projeksiyonlarını gözler önüne sermektedir. İkinci çalışma, Hava Durumu Araştırma ve Tahmin (WRF) modelinin 60 fizik kombinasyonunun 2020 yılı için Türkiye üzerinde kullanılmasıyla gerçekleştirilmiştir. Son çalışma, yüksek emisyon senaryosu altındaki CMIP6 GCM'ler topluluğunu EMBS bölgesinde yüksek çözünürlüğe (4 km) dinamik olarak çıkarmak için Sözde Küresel Isınma (PGW) yaklaşımını kullanır. Temel bulgular, her iki senaryo altında istatistiksel anlamlı olarak Türkiye'nin güneybatı kesiminde kış yağışlarının azalmasını, kuzeydoğu kesiminde ise artmasını öngördüğünü göstermektedir. Öte yandan, yüksek emisyon senaryosunda daha sıcak projeksiyonlarının neden olduğu konvektivite, Türkiye'deki yaz yağış düşüşlerini kısmen dengelemektedir. Duyarlılık çalışmasında günlük yağış korelasyon değerleri 0,5 ile 0,65 arasındadır ve bu aralık uzun döneme ait geçmiş

yönelik simülasyonlarda geliştirilmiştir. WRF modeli, EMBS bölgesindeki kış ve ilkbahar yağış anomalilerini ve tüm mevsimlerde büyük ölçekli düşük seviyeli sirkülasyon anormalliklerini mükemmel bir şekilde yakalamıştır. Yazın termal-alçak gelişimi ve bunun sonbahardaki izi de genellikle WRF tarafından iyi bir şekilde yakalanmıştır. Ancak asıl çelişki, özellikle Kafkasya ve yakın bölgelerdeki yaz yağışı anomalilerinde ortaya çıkmakta ve bu durum Hazar Denizi'nin deniz-yüzey sıcaklık anomalileri gerekçelendirilerek ek simülasyon yardımıyla tartışılmaktadır.

Anahtar Kelimeler: Akuple Model Karşılaştırma Projesi Aşama 6, Küresel İklim Modeli, Doğu Akdeniz Karadeniz Bölgesi, Sözde Küresel Isınma, Hava Durumu Araştırma ve Tahmin Modeli

To the ambiguous meaning of life

ACKNOWLEDGMENTS

First and foremost, I would like to express my sincere thanks to my supervisor Prof. Dr İsmail Yücel, and my thesis monitoring committee member Assoc. Prof. Dr Mustafa Tuğrul Yılmaz, for not only paving the way for me but also for trusting me at critical moments. Prof. Dr İsmail Yücel patiently trained me in climate modelling with his great fund of knowledge, which enabled me to grasp the literature and contribute to it in this field. Assoc. Prof. Dr Mustafa Tuğrul Yılmaz taught me a lesson that any complex-apparent problem could be easily coded by concerning a little bit with it.

I would like to thank Prof. Dr Nermin Şarlak for encouraging me to do a PhD at Middle East Technical University and become a well-educated academician. I also would like to thank Prof. Dr Ömer Lütfi Şen, whom I look up to, for his contributions throughout my PhD studies.

I would like to give special thanks to the Turkish High Performance and Grid Computing Center (TÜBİTAK ULAKBİM) and its referred National e-Science e-Infrastructure (TRUBA) unit in collaboration with the EURO-CC project. Their support was invaluable in terms of not only providing us national HPC facilities but also helping us when running into a problem. I also would like to appreciate the World Climate Research Programme and its operation team on coupled modelling, arranging and supporting CMIP6. I also appreciate the climate modelling teams around the world for ensuring and presenting their outputs openly, the Earth System Grid Federation (ESGF) for archiving the data and maintaining accession, and the several funding agencies, that promote CMIP6 and ESGF. Finally, I am grateful to the Turkish General Directorate of Meteorology for enabling us to ensure accession to meteorological data along Türkiye and the World Meteorological Organization for the data outside Türkiye.

TABLE OF CONTENTS

ABSTRACT.....	v
ÖZ.....	vii
ACKNOWLEDGMENTS	x
TABLE OF CONTENTS.....	xi
LIST OF TABLES	xiii
LIST OF FIGURES	xiv
LIST OF ABBREVIATIONS	xx
CHAPTERS	
1 INTRODUCTION	1
1.1 Introduction.....	1
1.2 Significance of the study.....	9
1.3 Objectives and scope of the study.....	10
1.4 Description of the thesis	10
2 LITERATURE REVIEW	13
2.1 Studies conducted around Türkiye	13
2.2 Studies conducted around the world.....	16
2.2.1 WRF sensitivity studies	16
2.2.2 WRF GCM dynamic downscaling studies.....	20
3 MATERIALS AND METHODS.....	27
3.1 Study area	27
3.2 Datasets.....	29
3.3 Methodology.....	33

3.3.1	Performance metrics for evaluation of the CMIP5 and CMIP6.....	33
3.3.2	Regional climate model (RCM): WRF	34
3.3.3	WRF configurations	37
3.3.4	PGW process	39
3.3.5	Model verification with the PGW retrospective simulations	41
4	RESULTS.....	43
4.1	Results of the GCM evaluation and future projections	43
4.1.1	Validation of ERA5 temperature and precipitation.....	43
4.1.2	Performance assessment of the CMIP5 and CMIP6	45
4.1.3	Biases in the ensemble means of the CMIP5 and CMIP6.....	47
4.1.4	Future projections.....	49
4.1.4.1	Precipitation	49
4.1.4.2	Near-surface temperature	52
4.1.4.3	Assessment of the annual changes	54
4.2	Results of the sensitivity of the WRF physics parameterizations	60
4.3	Results of the PGW-based dynamic downscaling.....	62
4.3.1	Validation	62
4.3.2	Seasonal precipitation change	65
4.3.3	“Dynamic” and “thermodynamical” factors.....	69
4.3.4	Additional simulation.....	80
5	DISCUSSION	89
6	CONCLUSION	95
	REFERENCES	97
	CURRICULUM VITAE	115

LIST OF TABLES

TABLES

Table 3.1 Ensemble members, data availability, and spatial resolutions of CMIP5 GCMs employed in the study. Checkmarks for future simulations indicate at least one of RCPs (Bağçacı et al., 2021).	30
Table 3.2 Ensemble members, data availability, and spatial resolutions of CMIP6 GCMs employed in the study. Checkmarks for future simulations indicate at least one of SSPs (Bağçacı et al., 2021).	31
Table 3.3 Ensemble members, variant label (ens. used), and horizontal resolutions of CMIP6 GCMs used in the PGW-based dynamic downscaling study.....	33
Table 3.4 Mandatory data fields in the PGW perturbation to force RCM (WRF).	40
Table 4.1 Annual means and standard deviations of precipitation simulations of the best-performing available CMIP6 GCMs and their counterparts in the CMIP5 for Türkiye based on the RCP8.5 and SSP5-8.5. In the table, statistically significant anomalies at the $p=0.05$ level are expressed with bold characters (Bağçacı et al., 2021).	58
Table 4.2 Annual means and standard deviations of the near-surface temperature simulations of the best-performing available CMIP6 GCMs and their counterparts in CMIP5 for Türkiye based on the RCP8.5 and SSP5-8.5. All the near-surface temperature anomalies in CMIP5 and CMIP6 GCMs are statistically significant at the $p=0.05$ level (Bağçacı et al., 2021).	60
Table 4.3 SST availability across the CMIP6 GCMs. Cnbu refers to “could not be used”.	81

LIST OF FIGURES

FIGURES

Figure 3.1. Study area (EMBS) elevation map. The first two studies, i.e., GCMs evaluation and their future projections and WRF sensitivity tests were conducted focusing the central Türkiye domain. The third study, i.e., PGW-based dynamic downscaling, was performed over the whole domain presented in the figure.	28
Figure 3.2. The data consistency/availability throughout the validation period of the first study	29
Figure 3.3. The summary flowchart of the WRF modelling	36
Figure 3.4. WRF physics parameterizations interactions. We adapted this figure directly from Skamarock et al. (2019).....	36
Figure 3.5. The PGW methodology flowchart	41
Figure 4.1. Comparison of the ERA5 reanalysis and station a) monthly precipitation, b) monthly mean precipitation, c) monthly near-surface temperature, d) monthly mean near-surface temperature. The related statistics are given in the figure, and more detailed information can be found in the original article of Bağçacı et al. (2021).	44
Figure 4.2. Comparison of the best four- and worst four-performing CMIP6 and CMIP5 GCMs with ERA5 for precipitation (Bağçacı et al., 2021).	46
Figure 4.3. Comparison of the best four- and worst four-performing CMIP6 and CMIP5 GCMs with ERA5 for near-surface temperature (Bağçacı et al., 2021).....	47
Figure 4.4. The mean biases in a) near-surface temperature and b) precipitation. The CMIP5 is in the first and CMIP6 in the second rows. The ensemble members are regridded to the coarsest-resolution GCM's horizontal resolution, and then seasonal means are taken in the historical periods of the CMIP5 and CMIP6 individually (Bağçacı et al., 2021).....	48
Figure 4.5. SSP2-4.5 precipitation anomaly a) in the near b) medium c) long terms. In the figure, statistically significant changes at the $p=0.05$ level are expressed with the hatched rasters (Bağçacı et al., 2021).	51

Figure 4.6. SSP5-8.5 precipitation anomaly a) in the short b) medium c) long terms. In the figure, statistically significant changes at the $p=0.05$ level are expressed with the hatched rasters (Bağçacı et al., 2021)..... 52

Figure 4.7. SSP2-4.5 near-surface temperature anomaly a) in the short b) medium c) long terms. All the near-surface temperature anomalies in the SSP2-4.5 and SSP5-8.5 are statistically significant at the $p=0.05$ level; thus, no hatching is drawn for the clarity (Bağçacı et al., 2021). 53

Figure 4.8. SSP5-8.5 near-surface temperature anomaly a) in the short b) medium c) long terms. All the near-surface temperature anomalies in the SSP2-4.5 and SSP5-8.5 are statistically significant at the $p=0.05$ level; thus, no hatching is drawn for the clarity (Bağçacı et al., 2021). 54

Figure 4.9. Comparison of the precipitation and near-surface temperature anomalies acquired from CMIP5 and CMIP6 under the highest-emission scenarios over Türkiye on an annual basis (Bağçacı et al., 2021). 56

Figure 4.10. The daily mean precipitation statistics of the ground observations and 60 WRF configurations. The first box denotes station statistics. The dashed line belongs to the median value of the stations. The mean values of the boxes are shown with red points, and the median values are shown with the black lines in the boxes. 61

Figure 4.11. The WRF simulations configurations-wide precipitation statistics. The daily precipitation correlations (the left axis with the light pink box) and RMSEs (the right axis with the turquoise box). The black points denote the mean values of the correlations and RMSE. 62

Figure 4.12. The WRF simulations precipitation statistics: a) The monthly precipitation correlation (the left axis with the blue lines) and RMSE (the right axis with the red lines). The solid line denotes the WRF-ground observation statistics, dashed line denotes the WRF-GPCC statistics, dot dashed line denotes WRF-GPCC HOAPS statistics, and dotted line denotes WRF-EOBS statistics. b) As in a, but for daily precipitation statistics between WRF and ground observations. c) The spatial

daily precipitation correlations between WRF and ground observations for 1995-2014 in Türkiye domain. d) As in c, but for the wet season (NDJFM)..... 64

Figure 4.13. The WRF simulations near-surface temperature statistics: The daily and monthly correlation (the left axis with the blue lines) and the daily and monthly RMSE (the right axis with the red lines). The solid line denotes the daily WRF-ground observation statistics, dashed line denotes the monthly WRF-CRU statistics, dot dashed line denotes the daily WRF-EOBS statistics, and dotted line denotes the monthly WRF-ground observation statistics. 65

Figure 4.14. The seasonal precipitation change (in the units of mm) between 2071-2100 (future SSP5-8.5 scenario) and 1985-2014 (historical) retrieved from 13 CMIP6 GCM model ensemble. The statistically significant changes at $p \leq 0.05$ level are hatched. 66

Figure 4.15. The seasonal precipitation change between 1995-2014 and the corresponding pseudo future period in the units of mm obtained from the WRF simulations for the EMBS domain. 67

Figure 4.16. The large-scale low-level (850 hPa) circulation (winds as vectors) and SLP (shadings) change signal of the PGW forcing between 2071-2100 (future SSP5-8.5 scenario) and 1985-2014 (historical) retrieved from 13 CMIP6 GCM model ensemble. The wind vectors are in the units of m/s and sea-level pressure is in the units of pascal. The reference vector is presented in the upper left. 69

Figure 4.17. The low-level (850 hPa) circulation (winds as vectors) and SLP (shadings) change between 1995-2014 and the corresponding pseudo future period for each season obtained from the WRF simulations for the EMBS domain. The wind vectors are in the units of m/s and sea-level pressure is in the units of pascal. The reference vector is presented in the upper left. 70

Figure 4.18. The low-level (850 hPa) circulation (winds as vectors) and SLP (shadings) change signal of the PGW forcing between 2071-2100 (future SSP5-8.5 scenario) and 1985-2014 (historical) retrieved from 13 CMIP6 GCM model ensemble for the extended EMBS domain. The wind vectors are in the units of m/s

and sea-level pressure is in the units of pascal. The reference vector is presented in the upper left.	71
Figure 4.19. The near-surface (at 10-meter for the winds and 2-meter for the specific humidity) wind pattern (vectors) and specific humidity (shadings) change between 1995-2014 and the corresponding pseudo future period for each season obtained from the WRF simulations for the EMBS domain. The wind vectors are in the units of m/s and specific humidity in the units of g/kg. The reference vector is presented in the upper left.	73
Figure 4.20. The low-level (850 hPa) specific humidity change between 1995-2014 and the corresponding pseudo future period in the units of g/kg for each season obtained from the WRF simulations for the EMBS domain.....	73
Figure 4.21. The vertical pressure velocity (omega) change between 1995-2014 and the corresponding pseudo future period in the units of hPa/hr for each season obtained from the WRF simulations for the EMBS domain. The omega changes are presented in 200 hPa (in the top), 500 hPa (in the middle), and 850 hPa (in the bottom) pressure levels.	74
Figure 4.22. The near-surface temperature (at the top) and dew-point depression (at the bottom) change between 1995-2014 and the corresponding pseudo future period in the units of °C for each season obtained from the WRF simulations for the EMBS domain. The dew-point depression was averaged with the values between the near-surface and 700 hPa pressure level.	74
Figure 4.23. The near-surface temperature change signal of the PGW forcing between 2071-2100 (future SSP5-8.5 scenario) and 1985-2014 (historical) retrieved from 13 CMIP6 GCM model ensemble for the extended EMBS domain in the units of °C.	75
Figure 4.24. The vertical pressure velocity (omega) change signal between 2071-2100 (future SSP5-8.5 scenario) and 1985-2014 (historical) retrieved from 13 CMIP6 GCM model ensemble for the extended EMBS domain in the units of hPa/hr. It should be noted that legend is one-tenth of the WRF simulations.	75

Figure 4.25. The specific humidity change signal of the PGW forcing between 2071-2100 (future SSP5-8.5 scenario) and 1985-2014 (historical) retrieved from 13 CMIP6 GCM model ensemble for the extended EMBS domain in the units of g/kg. The first row shows the near-surface (at 2m) changes, and the second row shows the low-level (at 850 hPa) changes..... 76

Figure 4.26. The long-term (between 2071-2100 (future SSP5-8.5 scenario) and 1985-2014 (historical) periods) seasonal mean warming differences: a) between sea-surface temperature and skin temperature of all available GCMs, b) between three GCMs (CMCC-CM2-SR5, CMCC-ESM2, HadGEM3-GC31-MM) SST and all available GCM ensemble SST (three GCMs SST increase minus full ensemble SST increase). The coastal regions exhibit a blocky cooler appearance due to the bilinear interpolation process from coarse to fine resolution. It was avoided in the interpolation step of the WRF-preprocess. 82

Figure 4.27. The low-level (850 hPa) circulation (winds as vectors) and SLP (shadings) change between 1995-2004 and the corresponding pseudo future period for each season obtained from the WRF simulations for the Caucasus and nearby regions. The wind vectors are in the units of m/s and sea-level pressure is in the units of pascal. The reference vector is presented in the upper left. 83

Figure 4.28. The near-surface temperature (at the top) and dew-point depression (at the bottom) change between 1995-2004 and the corresponding pseudo future period in the units of °C for each season obtained from the WRF simulations for the Caucasus and nearby regions. The dew-point depression is averaged with the values between the near-surface and 700 hPa pressure level. 84

Figure 4.29. The vertical pressure velocity (omega) change between 1995-2004 and the corresponding pseudo future period in the units of hPa/hr for each season obtained from the WRF simulations for the Caucasus and nearby regions. The omega changes are presented in 200 hPa (in the top), 500 hPa (in the middle), and 850 hPa (in the bottom) pressure levels. 84

Figure 4.30. The near-surface (2-meter; at the top) and low-level (850 hPa; at the bottom) specific humidity change between 1995-2004 and the corresponding pseudo

future period in the units of g/kg for each season obtained from the WRF simulations for the Caucasus and nearby regions. 85

Figure 4.31. The seasonal precipitation change between 1995-2004 and the corresponding pseudo future period in the units of mm obtained from the WRF simulations for the Caucasus and nearby regions. 85

LIST OF ABBREVIATIONS

ABBREVIATIONS

ACM2	Asymmetric Convective Model with non-local upward mixing and local downward mixing
AR6	IPCC Assessment Report 6
AWOS	Automated Weather observation systems
CFSR	Climate Forecast System Reanalysis
CMIP	Coupled Model Intercomparison Project
CONF	Configuration
CPC	Climate Prediction Centre
CRU	Climatic Research Unit
EA/WR	Eastern Atlantic-Western Russia teleconnection
ECMWF	European Centre for Medium-Range Weather Forecasts
ECS	Equilibrium climate sensitivity
EMBS	Eastern Mediterranean Black Sea Region
DECK	Diagnostic, Evaluation and Characterization of Klima
ENSO	El Niño/Southern Oscillation
FNL	Final Global Analysis
GCM	Global climate/circulation model
GDM	General Directorate of Meteorology
GFS	Global Forecast System

GHG	Greenhouse gases
GPCP	Global Precipitation Climatology Project
GPS	Global positioning system
KGE	Kling-Gupta efficiency
LCC	Lamber conformal conic
MAE	Mean absolute error
MD	Modified index of agreement
MME	Multi-model ensemble
MMEA	Multi-model ensemble average
MODIS	Moderate Resolution Imaging Spectroradiometer
MORRISON2	Morrison double-moment
MPE	Multi-sensor Precipitation Estimates
MR	Comprehensive Rating Metric
MYJ	Mellor-Yamada-Janjic
NAO	North Atlantic Oscillation
NCAR	National Center for Atmospheric Research
NRMSE	Normalized root mean square error
NWP	Numerical weather prediction
PBL	Planetary boundary layer
PGW	Pseudo Global Warming
RCM	Regional Climate Model
RCP	Representative Concentration Pathways

RMSE	Root mean square error
RRTMG	Rapid Radiative Transfer Model
ScenarioMIP	Scenario Model Intercomparison Project
SE _a	Standard error of interception
SE _b	Standard error of slope
SE _r	Residual standard error
SLP	Sea-level pressure
SNAO	Summer North Atlantic Oscillation
SPAEF	Spatial Efficiency
SSP	Shared Socioeconomic Pathways
SST	Sea-surface temperature
UNEP	United Nations Environment Programme
U10	Eastward wind component at 10-meter
V10	Northward wind component at 10-meter
VTABLE	Variable table
WEHY	Watershed Environment Hydrology Model
WPS	WRF preprocessing system
WRF	Weather Research and Forecasting
WSM6	WRF-Single-Moment 6-Class
YSU	Yonsei University

CHAPTER 1

INTRODUCTION

1.1 Introduction

The Coupled Model Intercomparison Project is recently in the sixth phase (CMIP6), which presents a set of build-ups on its predecessor (CMIP5) primarily in the sense of distribution of the radiative forcing elements stemming from the natural or anthropogenic processes (Eyring et al., 2016; Stouffer et al., 2017; Wyser et al., 2020). Accordingly, quantification of greenhouse gases (GHG), presentment of aerosol forcing (containing optical features) and land-use alterations, all of which are used in forcing to models, show variation with the CMIP6 (Eyring et al., 2016; Wyser et al., 2020). The CMIP6 models can be divided into two main groups: 1) The Diagnostic, Evaluation and Characterization of Klima (DECK) and historical simulation experiments, which are common and mandatory for model providers; 2) CMIP-Endorsed Model Intercomparison Projects (MIPs) in coordination with DECK and historical simulations (Eyring et al., 2016). The Scenario Model Intercomparison Project (ScenarioMIP) is among the major actions within the MIPs, which is operated by latest emission and land-use scenarios beneath latest circumstances of social progress, namely the Shared Socioeconomic Pathways (SSPs) (O'Neill et al., 2016). The CMIP6 SSPs follow the latest emission tendencies, updating their equivalent in CMIP5 (the Representative Concentration Pathways, RCPs) (O'Neill et al., 2016; Bağçaci et al., 2021).

On the other hand, a set of CMIP6 models exhibit more equilibrium climate sensitivity (ECS), which is described as the worldwide mean temperature increase response when the world's climate system hits the equilibrium phase by doubling CO₂ (Stouffer et al., 2017; Grose et al., 2020). Even though the CMIP5 and CMIP6 GCMs are nominally forced by the identical radiation beneath the equivalent

scenarios, the CMIP6 present more ECS and warmer projections through the end of this century than the CMIP5 (Grose et al., 2020; Wyser et al., 2020). Wyser et al. (2020) analyzed the reason and stated that weights and dispersions of prescribed GHG are fundamental factors in the warmer projection for the EC-Earth3-Veg GCM. Concerning the latest circumstances of GHGs in CMIP6 and aerosol-cloud interplays, the more resistant cloud feedback may be the underlying factor of warmer projections and more ECS (Eyring et al., 2016; Gettelman et al., 2019; Forster et al., 2020; Grose et al., 2020). Sellar et al. (2020) remarked that inconsistency between the model thermodynamics and prescribed ozone exists in the GCMs which do not handle ozone simulations interactively. They added that, in this way, the ECS estimation might be impressed by %10. In regional aspects, future projections would not be the same even though an equal amount of radiative forcing is present in RCPs and SSPs equivalents since RCPs were developed based on the former conditions (van Vuuren et al., 2011; O'Neill et al., 2016; Bağçaci et al., 2021).

Due to its expected high response to the increasing radiative forcing associated with GHG emission scenarios, the Mediterranean region is one of the main climate change hotspots (Giorgi, 2006). A sharp decrease in mean precipitation and an increase in variability (tending to show more extremes) concomitant with increasing temperatures make the region vulnerable to natural disasters, i.e., floods, desertification, and wildfires. Recent studies have shown that the Eastern Mediterranean Black Sea (EMBS; here, we define between ~ 22-53 °E and 33-45 °N) region's southern and western parts are among the hotspot's most seriously affected areas (Yilmaz and Yazicigil, 2011; Barcikowska et al., 2018; Tuel and Eltahir, 2020). The region is highly populated, and people here rely upon the water resources on-the-spot in drinking water, agriculture, and industry. On the other hand, the northeastern EMBS has high annual precipitation totals, and an expected increase in the amount and extremes may amplify existing flood risks (Bağçaci et al., 2021). In the east, the climatic change effects even now felt are expected to alter the snowmelt runoff timings of the Euphrates–Tigris basin, which has two main snow-fed transboundary rivers supplying southeastern Türkiye, Syria, and Iraq (Sen et al.,

2011; Yucel et al., 2015). An increase in temperature and a decrease in precipitation over the upstream highland areas cause shrinkage in snow cover area and snow water equivalent, ultimately resulting in earlier snowmelt and a decrease in annual runoff totals (Bozkurt and Sen, 2013). It is vital for the water-stressed people living already in civil war conditions like in Syria (Tuel and Eltahir, 2020). All these make the EMBS's current and future climate scientifically attractive, which needs to be investigated with state-of-the-art tools focusing on the most recent global climate models (GCMs) involving their dynamically downscaled and high-resolution projections. The spring and fall seasons are transitional between winter and summer over the EMBS, i.e., fall season months show late summer and the spring season shows late winter features (Lionello et al., 2006); therefore, the summer and winter climatology will be sketched out in the following.

The summer (JJA) climatology over the EMBS is mainly driven by stabilizing effect of the cold air advection by low level consistent northerly flow, i.e., Etesians and adiabatic warming of mid and upper tropospheric subsidence winds (Ziv et al., 2004; Poupkou et al., 2011; Tyrlis and Lelieveld, 2013; Barcikowska et al., 2019). The former is characterized by the large-scale sea-level pressure dipole between Middle East and the central and southeastern Europe (Anagnostopoulou et al., 2014). The resulting low-level circulations intersect over the Aegean Sea with the funnelling effect and strengthen by mid and upper-tropospheric subsidence (Rodwell and Hoskins, 2001; Barcikowska et al., 2019). The latter is part of the Indian summer monsoon desert mechanism (Rodwell and Hoskins, 1996; Barcikowska et al., 2019), suppressing precipitation with a strong ridge over the western EMBS, including most Anatolian plateau. However, the Northeastern Anatolia and the Caucasus mountainous regions and their Black Sea coasts (in the northeastern EMBS) are located in a buffer zone of the subsidence with a weak ascent at the mid (500 hPa) troposphere level (Simpson et al., 2015). Unlike the typical Mediterranean climate, these regions are all-year rainy and show smoothed seasonality. Barcikowska et al. (2019) investigated the effect of summer season surface warming on the local circulation over the region encompassing EMBS by comparing 300 warmest and

coolest events. They showed that surface warming leads to mid-tropospheric subsidence development over the northeastern Anatolia and the Caucasus, which wipe the buffer zone out suggested by Simpson et al. (2015). According to the authors, surface warming also leads to deepening heat low over the Eastern Mediterranean and Arabian Peninsula. Meanwhile, enhanced sea level pressure over the Balkans and the Black Sea suppresses relative humidity and precipitation over those regions. However, they did not focus on sea-surface temperature and did employ a relatively low-resolution model (GFDL CM2.5 with approximately 50 km horizontal resolution), which are obstructive to gain comprehensive insight on complex terrain induced precipitation over the regions mentioned above. The authors also underline that surface warming overcomes the counterbalancing effects of Etesians and a teleconnection, summer North Atlantic Oscillation (SNAO), over the EMBS. Therefore, the local circulation response of the EMBS region to the thermal originating “dipole-like” formation mentioned above needs to be further investigated with a fine-scale climate model.

In winter (DJF) or the wet season (NDJFM), the North Atlantic Oscillation (NAO), El Niño/Southern Oscillation (ENSO), Eastern Atlantic-Western Russia (EA/WR) teleconnections, and a remote link between East Asian and Mediterranean troughs affect the climate regime of the EMBS (Kadioğlu et al., 1999; Kutiel and Benaroch, 2002; Xoplaki, 2002; Alpert et al., 2006; Trigo et al., 2006; Duzenli et al., 2018; Sen et al., 2019; Tuel and Eltahir, 2020). The NAO is the most studied and well-documented for the Mediterranean winter climate. The large-scale seesaw in the atmospheric mass between Iceland’s low and Azores’ high, the NAO, determines the direction of the prevailing wind patterns over the EMBS. The increased (decreased) Iceland pressure leads to the southwesterlies (northeasterlies) that moisten (dry) the western and southern parts of the region with ascending (descending) warm (cold) air (Eshel and Farrell, 2000; Xoplaki et al., 2004; Türkeş and Erlat, 2006). In a changing climate, the expected northward shift of the mid-latitude storm track and the intensification of the NAO associated with its positive phase favour the anomalous ridge over the Mediterranean and dry the western and southern EMBS by

the northeasterlies (Ulbrich et al., 2006; Giorgi and Lionello, 2008; Barcikowska et al., 2018; Tuel and Eltahir, 2020; Bağçaci et al., 2021). Therefore, the new conditions of the North Atlantic synoptic systems are expected to suppress cyclogenesis, thus precipitation over the region, which hosts one of the three most cyclone-active seas in the Mediterranean, i.e., the Aegean Sea (Trigo et al., 2002; Lionello et al., 2006; Tuel and Eltahir, 2020). Such conditions do not seem to decrease precipitation but rather further increase existing heavy rains over the northern and northeastern EMBS, which hosts another of the most cyclone-active seas, the Black Sea. (Trigo et al., 2002; Lionello et al., 2006; Şen et al., 2015; Barcikowska et al., 2018). The frequent cyclones are triggered here in association with the vorticity advection from a westerly positioned upper trough (Mastrantonas et al., 2021). The prevailing wind patterns favour the upslope lifting towards the region's steep orography (Önol, 2012). However, Tuel and Eltahir (2020) have shown that a decrease in the land-sea temperature contrast, expected with the high emission scenario, may produce an anticyclone and suppress precipitation over the region. Apart from regional impacts, the thermodynamic contribution to cyclones can be higher than the dynamical and may also reflect the changes in the lifecycle and/or invigorating cyclones through latent heating. Despite the controversy, the authors agree that one needs to employ high-resolution climate models to simulate this picture adequately. The studies mentioned above investigating the current and future climate of the EMBS have used no finer than 27 km horizontal resolution.

There is a number of GCMs released with the latest CMIP6, some of which have been designated with the higher horizontal resolutions and number of vertical levels than counterpart GCMs in CMIP5 (i.e. IPSL-CM5A-LR has 3.8x1.9 horizontal resolution and 39 vertical levels in CMIP5 while IPSL-CM6A-LR has 2.5x1.3 horizontal resolution and 79 vertical layers) (Boucher et al., 2020). Nevertheless, CMIP6 GCMs still have coarse resolutions (no finer than 50 km and most of them under 100 km nominal resolution) to simulate cloud formation, soil moisture exchange, and convection and orography induced processes which are key components in the basin-scale hydrologic cycles (Gorguner et al., 2019). Therefore,

downscaling GCMs with appropriate methods, such as dynamic or statistical, is required. The statistical downscaling method is based on the transfer function, which associates the regional observations with GCM outputs and uses this relation for the future climate projections (Fujihara et al., 2008; Guo et al., 2018; Gorguner et al., 2019; Garrido et al., 2020). Although the statistical downscaling method is computationally cheap, stationary climate assumption and the absence of physical rules weaken the method (Fujihara et al., 2008; Guo et al., 2018; Gorguner et al., 2019). On the other hand, a dynamic downscaling method with RCMs is developed in a similar model physical dynamic structure of the parent GCMs and the method enables resolving small scale process such as orographic precipitation (Fujihara et al., 2008; Guo et al., 2018; Garrido et al., 2020). It provides a non-stationary explicit solution to obtain high-resolution climate data with a physically and dynamically coherent way (Fujihara et al., 2008; Gorguner et al., 2019).

However, the dynamically downscaling process of GCMs is computationally expensive; thus, one may need to reduce multi-model ensemble size by evaluating the performances of GCMs or having other sampling strategies avoiding to eliminate individual GCMs (McSweeney et al., 2015; Ahmed et al., 2019). This is a hard challenge in climate modelling studies since a set of uncertainties accompany by GCMs such as natural variability of the climate system, emission scenario extents and model discrepancies (i.e., model physics parameterization) between CMIP GCMs (Overland et al., 2011). McSweeney et al. (2015) argued that elimination of poorly performing GCMs and selection of those that are highly performing problematic since one cannot be sure whether poorly performing models will be failed at the future projections (see also Knutti, 2010; Knutti and Sedláček, 2013). On the other hand, from the Bayesian approach, a poorly performing model in the historical period has less chance to be successful in the future period; but, the likelihood of success of highly performing models in the past is more (Overland et al., 2011). However, the authors agreed that selection method is more reasonable in particular regions and approaches in the case that critical features of model behaviour can be recognized and evaluated (Overland et al., 2011; McSweeney et al., 2012).

To avoid limiting the number of GCMs as far as uncertainty concerned, one may employ the pseudo global warming method (PGW). The PGW has recently been used in various dynamically downscaling studies, increasing the number of GCMs in a computationally efficient manner (Fujihara et al., 2008; Lauer et al., 2013; Dutheil et al., 2020; Hunt et al., 2020; Yu et al., 2020). At its simplest, the method computes monthly averages of the mean differences between future and current climate data of GCMs and adds them on present-day forcing data (the process is also called perturbing present-day forcing data) (Fujihara et al., 2008). Therefore, it extends the GCM pool easier than individually dynamic downscaling, thus reducing uncertainties by taking climate change signals from different GCM sources. It can be generalized that there are two major advantages and one major disadvantage with the PGW approach against individually dynamic downscaling of GCMs. As mentioned before, the first advantage is that the PGW approach is computationally cheap and allows one to consider sizeable individual GCM projections, thus reducing uncertainties by giving more extensive climate estimates over the region of interest (Fujihara et al., 2008; Lauer et al., 2013; Hunt et al., 2020). The second one is that the PGW approach is based on perturbing the present climate data with the climate change signals from employed GCMs and downscaling those perturbed data; therefore, the bias correction in GCM boundary conditions is unnecessary (Lauer et al., 2013; Dutheil et al., 2020; Hunt et al., 2020). The disadvantage is that the PGW approach does not consider the nonlinear relations between the local weather patterns and variabilities (such as mesoscale circulations and interannual variability) and climate change, leaving boundary conditions unchanged (Lauer et al., 2013; Yu et al., 2020). Because of similar reasons, Rasmussen et al. (2011) attributed their PGW-based study as an “imposed” warming analysis rather than robust scenario-based climate change analysis (Yu et al., 2020).

Before starting any dynamical downscaling study with a regional climate model (RCM, herein Weather Research and Forecasting model, WRF), the optimal model configuration should be ensured based on the observations to specify credibility of the model (Argüeso et al., 2011; Flaounas et al., 2011). The model configuration

includes selecting some physical parameterization schemes in a combinational manner. It helps to understand how sensitive physical options is to the region of interest and which physical mechanisms dominate the others. It can provide a basis for long-term climate change studies (Flaounas et al., 2011; Meyer and Jin, 2017; Gorguner and Kavvas, 2020). However, it is somewhat tricky since the similar argument from McSweeney et al. (2015) can be mounted here: how can one be sure that today's atmospheric physics options are valid in the future? The best thing to do here is to extend the simulation period as much as possible to introduce various regional climate conditions to the model (Flaounas et al., 2011; Klein et al., 2015). Similar to the downscaling of GCM-scale simulations, some uncertainties come from "imperfect" forcing and reference datasets (Flaounas et al., 2013; Klein et al., 2015). The downscaling resolution is also a source of some uncertainties, especially whether convection parameterization is used; however, more information will be provided in the "Review of the Literature" section to keep it concise.

In consideration of the novelties of CMIP6 (Annan et al., 2020), it is important to reevaluate the most likely exposed regions to the climate change effects, such as the EMBS, by centring the Türkiye domain. Specifically, Türkiye is situated in the Mediterranean macroclimatic region of the subtropical zone (Patrick, 2017). The United Nations Environment Program (UNEP) set forth that desertification threatens Türkiye on a large scale with high potential, and its impacts are already felt there (Pinkerton and Rom, 2014). The future climate projections obtained from former versions of the CMIP6 (i.e., CMIP3 and CMIP5) show that the situation would become harder with boosted warm and dry circumstances over Türkiye and the EMBS on a larger scale (Ulbrich et al., 2006; Önol and Semazzi, 2009; Ozturk et al., 2015; Demircan et al., 2017; Barcikowska et al., 2019; Tuel and Eltahir, 2020; Bağçacı et al., 2021). The significance of this thesis is further explained in the next section.

1.2 Significance of the study

Anthropogenic climate change is a nonhomogeneous nature response to human-induced activities such as GHGs emissions and land-use changes. Therefore, alongside the natural climate variability, these human-induced activities should be well represented to obtain credible projections, especially in hot spots like the Mediterranean. It is important to see whether these hot spots would remain human-habitable regions from the socioeconomical and climatological perspective (i.e., water scarcity, economic loss, weather extremes, natural hazards) since human migration movements might become highly dependent on climate change. There is a scarce number of studies in the literature tackling the climate change projections for Türkiye and large-scale EMBS. Besides, most of these studies utilize the former version of the CMIPs in which recent emission trends and land-use changes are not updated according to the latest conditions. This thesis fills the gap in the literature, focusing on the latest CMIP6 GCMs both in the coarse-resolution and fine-resolution scales.

The possible improvements of the CMIP6 over its predecessor CMIP5 are investigated in a comprehensive performance comparison study (Bağçacı et al., 2021), which is made for the first time over the Türkiye domain to our knowledge. This study is also prominent through including recent GHGs emission-based future projections for Türkiye under medium and high-range scenarios, SSP2-4.5 and SSP5-8.5. The second study of this thesis also has novel features, especially for the Türkiye domain. A large number of RCM physics options are tested over the country through dynamic downscaling of the state-of-the-art ERA5 reanalysis as a parent model. The outputs of the second study (the best-performing configurations time and region-specific) are very precious not only for long-term climate simulations but also for short-term weather forecasts. The final study forms the backbone of the thesis, in which the highest-resolution climate simulations so far (to our knowledge) are run with an RCM over the EMBS where Türkiye is centred. This study also contains the firsts from other perspectives as the dynamic downscaling of the CMIP6 GCM

ensemble (it is also one of the first studies around the world) for the future period and dynamic downscaling of the ERA5 reanalysis for the retrospective period.

1.3 Objectives and scope of the study

The main objectives and scope of this dissertation can be summarized as below:

- Specifying performance amelioration of the CMIP6 GCMs according to the CMIP5 GCMs over the Türkiye domain, using the large-size model pools.
- Revealing performance ranks of the CMIP6 GCMs in simulating precipitation and near-surface temperature through temporal and spatial metrics.
- Projecting future climate and exhibiting statistically significant changes over the Türkiye domain under the medium (SSP2-4.5) and high (SSP5-8.5) emission ranges in a coarse resolution.
- Performing a WRF sensitivity analysis with the ERA5 reanalysis forcing dataset to obtain optimal model configuration considering the relatively long period, the year 2020.
- Obtaining a high-resolution retrospective climate dataset (with the 6-hour boundary update and hourly high-resolution, 4 km, output) with the WRF model.
- Obtaining ensemble-based high-resolution future climate projections over the large-scale EMBS relied on the CMIP6 SSP5-8.5 scenario in the context of PGW (the performance rankings of the first study are also considered when composing a GCM ensemble to be dynamically downscaled).

1.4 Description of the thesis

This thesis composes three-legged interrelating studies:

The first study investigates the performance of the latest CMIP6 GCMs in simulating monthly near-surface temperature and precipitation for the Türkiye domain compared to their former counterparts (CMIP5 GCMs). A large GCMs pool was utilized to conduct this comparative performance analysis, i.e., 36 CMIP5 GCMs and 33 CMIP6 GCMs. Secondly, the four best-performing CMIP6 GCMs were selected for forming an ensemble. The climatic change signals over Türkiye under the medium (SSP2-4.5) and high (SSP5-8.5) emission scenarios were assessed by taking multiyear seasonal mean differences of the ensembles between the three future periods (2030-2050, 2050-2070, and 2070-2100) and the baseline period (1995-2014). The extreme tendencies of the variables were also assessed for both CMIP GCMs comparatively. The first study was published in the Atmospheric Research Journal in 2021 (Bağçaci et al., 2021).

The second study performs a WRF sensitivity analysis with the ERA5 reanalysis forcing dataset to obtain optimal model physics configuration considering the relatively long period. A total of 60 model physics of the microphysics, cumulus, and planetary boundary layer schemes were employed in a combination manner over the Türkiye domain in 2020. The optimal physics combination was used in the PGW-based dynamic downscaling studies later on.

The final study carries out the PGW-based WRF dynamic downscaling over the EMBS. The thirteen relatively high-resolution GCMs (including the best-performing ones according to the first study) were employed in PGW-forcing dataset for the future period based on the SSP5-8.5 emission scenario. The retrospective WRF simulations were forced with the ERA5 reanalysis data.

CHAPTER 2

LITERATURE REVIEW

This section comprises the following subsections: “Studies conducted around Türkiye”, and “Studies conducted around the world”. “Studies conducted around the world” section divides into the following subsections: “WRF sensitivity studies” and “WRF GCM downscaling studies”, while “Studies conducted around Türkiye” also comprises such studies but not divided into the subsections.

2.1 Studies conducted around Türkiye

Fujihara et al. (2008) assessed hydro-climate change impacts over Seyhan Basin by hydrology and reservoir models. They utilized the PGW approach in downscaling NCEP/NCAR reanalysis data to 8.3-km horizontal resolution with the perturbation of SRES A2 scenario simulations of two CMIP3 GCMs. Later on, they used the downscaled data as input to the hydrology and reservoir models and developed a water use scenario to examine water availability. According to the authors, the basin's water resources would be sufficient if the water demand will not grow. However, if the irrigation area grows, they expect water scarcity to occur in the region.

Bozkurt et al. (2012) dynamically downscaled and evaluated three GCMs under CMIP3 over the eastern Mediterranean and the Black Sea regions for 1961-1990. They also downscaled NCEP/NCAR reanalysis data as a reference dataset in the regional climate model evaluation. They employed the RegCM3 model to dynamically downscale the reanalysis and GCMs to 27-km horizontal resolution and evaluated downscaled-GCM with CRU and the Turkish State Meteorological Service climate data. The authors stated that performance evaluation of the GCMs

with their downscaled outputs would increase the reliability and fidelity of the climate change projections on a regional basis. They concluded that all employed GCMs are substantially capable of simulating winter precipitation and temperature, while two of them show similar summer performance. They suggested downscaling outcomes of ECHAM5, CCSM3 and HadCM3 GCMs used in the study for future climate change impact studies over the region.

Bozkurt and Sen (2013) conducted a hydro-climate change impact assessment study over Euphrates-Tigris Basin, especially focusing on winter season changes between 2071-2099 and 1961-1990. They downscaled the scenario simulations of the identical GCMs as in their previous study to the identical horizontal resolution (Bozkurt et al., 2012). They projected a statistically significant increase in temperature and a decrease in snow-water equivalent in the basin. Accordingly, they predicted that surface runoff predates between 18 and 39 days in the headwaters of the basin.

Yucel et al. (2015) evaluated ten flash flood events in the Western Black Sea Region using the WRF-Hydro model. They obtained precipitation estimates from the numerical weather prediction model (WRF) with and without data assimilation (Yucel and Onen, 2014) and the EUMETSAT Multi-sensor Precipitation Estimates (MPEs). They calibrated the WRF-Hydro model with two events and evaluated the model performance with the remaining events. They found out that streamflow simulations are improved with the WRF model simulations, more prominently with the data assimilated one, due to their better representation of the storm precipitation characteristics. They added that MPE-based streamflow simulations perform poorly due to their dry bias in precipitation. As a result, they stated that calibrated WRF-Hydro runoff simulations reduced RMSE by around %22 with the WRF precipitation simulations. Further reduction in the RMSE was around %37 when used with the data assimilated one.

Gorguner et al. (2019) explored the future climate change impacts on the water resources in Gediz Basin by dynamically downscaling four CMIP5 GCMs with

Weather Research and Forecasting model (WRF) and putting upon outputs of the downscaled climate data as input to the Watershed Environmental Hydrology model (WEHY). They used the RCP4.5 and RCP8.5 scenarios of each four GCMs for future projections. They claimed that the ensemble approach would enhance the credibility of the future projections albeit not clarify why selected GCMs were preferred. They found large inter-model variability between parent models (GCMs) affecting the projected future inflows to the reservoir in the basin and concluded that the ensemble average of the projected outputs shows an increase in annual average inflows with decreasing trend throughout this century.

Gorguner and Kavvas (2020) further extended their study (Gorguner et al., 2019) to investigate future changes in the reservoir-storage levels and water demands over the Gediz Basin with a dynamic water balance model. They employed the outputs of their RCM (WRF-downscaled) and hydrological model (WEHY) simulations (Gorguner et al., 2019) as input to the dynamic water balance model. Besides, they utilized the FAO56 Penman-Monteith method (Allen et al., 1998) to estimate crop evapotranspiration and reservoir evaporation, which are the reservoir outflow components. They expected that irrigation-based water demands in the region would significantly increase, especially under the RCP8.5 scenario with a higher evapotranspiration rate. The authors concluded that reservoir-storage levels would not meet the irrigation requirements towards the end of this century, particularly in summers taken as the irrigation season.

Duzenli et al. (2021) conducted a sensitivity analysis of WRF model parameterization schemes and forcing datasets in reproducing eight distinct extreme precipitation events over Türkiye's Eastern Black Sea and Mediterranean regions. They used ERA5 and Global Forecast System (GFS) data as the initial and lateral boundary conditions and downscaled them to 9 km and 3 km horizontal resolution with two nested domains. According to certain performance criteria, the authors selected sub-ensemble members and validated the model by four of eight events. As a result, they stated that precipitation simulations in autumn are most sensitive to microphysics schemes. They added that the planetary boundary layer and cumulus

schemes mainly govern the precipitation events' timing and position. They found out that downscaled GFS simulations outperform downscaled ERA5 simulations in the Mediterranean region, while in the Eastern Black Sea region vice versa. The authors concluded that improving the resolution of the ERA5 reanalysis yielded better estimates of the precipitation, especially in the rugged regions.

The studies referenced above focusing on long-term climate simulations have been performed using previous versions of CMIP6 at a coarser resolution than the convection-permitting scale (4 km) for the Türkiye domain. Those using higher resolution have been conducted for short periods. This thesis provides long term very high-resolution climate simulations not only for Türkiye but also for EMBS. Due to these reasons, this thesis is a first in the literature in terms of providing long-term, very high-resolution climate simulations dynamically downscaling the latest GCMs not only for Türkiye but also for EMBS.

2.2 Studies conducted around the world

2.2.1 WRF sensitivity studies

Flaounas et al. (2011) analyzed the sensitivity of three convective parameterization schemes and two planetary boundary layer schemes of the WRF model to simulate the 2006 summer West African monsoon. They utilized final global analysis (FNL) with 1° spatial resolution as the forcing dataset and downscaled it to 50 km horizontal resolution, which was updated in six-hour intervals. They validated the optimal model configuration according to ground observations, radiosondes, GPS stations, and satellite data. The authors concluded that temperature, precipitation, and humidity simulations have the highest sensitivity to the planetary boundary layer scheme. On the other hand, the variability of the precipitation is mostly affected by the convection parameterization scheme. Specifically, they suggested that the Kain-Fritsch (in convection parameterization) and Mellor-Yamada-Janjic (in planetary

boundary layer parameterization) schemes combinations due to their better representation of the West African monsoon's temporal variability.

Pohl et al. (2011) performed a comprehensive sensitivity analysis of the WRF model parameters, including physical schemes, radiation and land surface schemes, and lateral and vertical boundary conditions over Equatorial East Africa with 1999 data. They have run the model for 58 different combination experiments in the four-set and downscaled ERA-Interim and ERA40 reanalysis data to 36 km resolution parent domain and later on 12 km resolution nested domain for each experiment. The authors employed ground observations and Global Precipitation Climatology Project (GPCP) datasets in the model configuration evaluation process. They found that uncertainties arising from different WRF model configurations are more significant than the biases. They concluded that precipitation simulations' accuracy is mainly governed by short-wave radiation scheme and less affected by cloud microphysics and planetary boundary layer schemes to a seasonal extent.

Argüeso et al. (2011) assessed the sensitivity of the cumulus, microphysics, and planetary boundary schemes in combinations, over Andalusia. They forced the WRF model by ERA-40 reanalysis data with six-hourly boundary conditions to obtain 10 km horizontal resolution climate data belonging to 1990-1999. The authors used numerous ground observations both to assess the model sensitivity results and climatically regionalize precipitation and temperature. They concluded that precipitation simulations by WRF are highly sensitive to the planetary boundary layer and cumulus schemes. In contrast, the microphysics scheme does not have a remarkable effect on the precipitation simulations. On the other hand, they found similar results in projecting temperature with all combinations; but, added that the planetary boundary layer scheme selection affects minimum values. As a result, they underlined that the WRF downscaling simulations on their own improve the climate illustration of the region.

Li et al. (2014) explored the sensitivity of WRF model physical parameterization schemes and downscaling resolutions, in simulating the southeastern United States

summer rainfall. They selected 01 August 15, 2009, as a simulation period by optimization criterion to reproduce long-term climatology over the region. The authors employed climate forecast system reanalysis (CFSR) data with 0.5° spatial and six-hour temporal resolutions and downscaled it to 3 km and 15 km for convection-permitting and convection-parameterized experiments, respectively. They utilized gridded observations of the climate prediction center (CPC) in comparison and evaluation processes. They stated that WRF simulations are more (less) affected by cumulus scheme parameterization (microphysics scheme parameterization). Interestingly, they found out that convection-permitting simulations do not significantly overperform convection-parameterization simulations with the Zhang-McFarlane scheme.

Similar to Flaounas et al. (2011), Klein et al. (2015) investigated the sensitivity of the three WRF model physical schemes over West African monsoon, but for the 1999 rainy season. They used three parameterizations for each scheme with the ensemble and sub-ensemble approaches and forced the model by ERA-Interim reanalysis data in six-hourly temporal and 0.75° horizontal resolution. The authors employed satellite and observation data in the comparison and validation processes of downscaled ERA-Interim data to 24 km horizontal resolution. In conclusion, they propounded that microphysics and planetary boundary layer schemes mainly affect the spread of total rainfall. They asserted that the more sophisticated microphysics scheme causes higher precipitation due to enhanced latent heat release. On the other hand, they added that the planetary boundary layer scheme governs the rainband position, while the cumulus scheme governs the position of the extreme rainfall.

Karki et al. (2017) analyzed the performance of the convection-parameterized and convection-permitting WRF simulations for a one-year experiment (between 2014 and 2015) over the central Himalayan region by downscaling ERA-Interim data to 25, 5, and 1 km horizontal resolution. They turned off the cumulus parameterization scheme for 1 km, and 5 km resolution even though the latter falls into the gray zone of the convection (Molinari and Dudek, 1992; Klein et al., 2015; Karki et al., 2017). The authors mainly focused on the diurnal and seasonal pattern of precipitation

(including monsoonal) and temperature over the region. According to the authors, 1-km resolution simulations outperform the others in projecting monsoonal rainfall, albeit all simulations overestimate western disturbances-induced rainfall over the region. They stated that all simulations mostly project temperature well; nevertheless, all have a cold (warm) bias in high (low) altitude regions. They added that 1-km resolution simulations also outperform the others in reproducing seasonal and diurnal precipitation patterns and their peak timings.

Posada-Marín et al. (2019) explored the sensitivity of the convective-parameterized and convection-permitting simulations over the Colombian Andes. They downscaled ERA-Interim data to 30 km and 10 km with two nested domains for the individual ENSO phases between 1998-2012. They increased the resolution up to 3.3 km for the 2009-2010 El Niño event for convection-permitting simulations. The authors employed ground and gridded observations to evaluate the model configuration process; besides, they employed original ERA-Interim data (non-downscaled) to see whether improvements exist in the downscaling process. The authors stated that ERA-Interim reanalysis is incapable of reproducing precipitation and has positive biases during the dry season of El-Niño. They attributed that such incapability is due to poor representation of the topography and can be eliminated with downscaling to some degree. They also stated that low sensitivity exists in selecting the convection parameterization scheme, and convection-permitting simulations improve the spatial representation of the precipitation.

Kouadio et al. (2020) made a sensitivity analysis of the WRF model parameterization schemes over the 2014 West African monsoon, mainly focusing on the Guinean coast and vicinity regions. Differently from the previously referred papers dealing with the West African monsoon, the authors also tested and compared convection-permitting (downscaling up to 4 km horizontal resolution) and convection-parameterized simulations. They utilized ERA-Interim reanalysis data in the two nested domains where inner domains both have 4 km horizontal resolution while outer domains have 20 and 24 km horizontal resolutions, in their two experiments. Finally, they compared the fine-resolution outputs of WRF with ground

observations, satellite, and reanalysis data. They concluded that convection-permitting simulations mostly better represent extreme rainfall events over the region than convective-parameterized simulations do. They added that the planetary boundary layer scheme affects rainfall distribution more than the microphysics scheme in convective-parameterized simulations; however, only one microphysics scheme was tested. On the other hand, they remarked that both schemes have less effect on the convection-permitting simulations.

The referred studies above have utilized former versions of the reanalysis as parent models, which were upgraded at the time of progress. We have a better opportunity to aim for higher resolutions in our dynamic downscaling studies with the help of state-of-the-art supercomputers. Moreover, long-term, high-resolution sensitivity studies have not been encountered for the Türkiye domain at the time of writing. To our knowledge, the sensitivity tests within this thesis present very high resolution and a large number of combinations of model physics for the first time for Türkiye.

2.2.2 WRF GCM dynamic downscaling studies

Lauer et al. (2013) conducted a comparative study with the PGW approach to evaluate uncertainties between the average of individually downscaled climate simulations perturbed by 10 CMIP5 GCMs and only one downscaled climate simulation perturbed by multi-model ensemble of the same GCMs. Their study area is the Hawaii region, and they used the Hawaii regional climate model, a specially configured version of the WRF model to simulate the Hawaiian climate. They improved resolution to 15 km and used RCP4.5 and RCP8.5 scenarios for future simulations. As a result, they stated that despite the higher intermodel variability in simulating precipitation changes and 10-m wind speed, averaged individual simulations and ensemble simulations are in good agreement in simulating those variables in addition to 2-m temperature. They also stated that high scalability exists between RCP4.5 and RCP8.5 scenarios in simulating 2-m temperature, which is not the case for precipitation and 10-m wind speed.

Flaounas et al. (2013) evaluated cyclones and surface winds over the Mediterranean with ERA-Interim reanalysis, IPSL-CM5 GCM (under CMIP5), and their 50-km downscaled simulations using the WRF model. According to the authors, improving the model resolution enables better representation of the steady topographic features and thus provides significant added value in representing the region's topography-induced cyclogenesis activities. However, they added that underestimated cyclogenesis activities with the IPSL-CM5 propagate into its downscaling simulations mainly because the studied region is relatively small and affected by “inaccurate” large-scale circulations of the parent model in the downscaling process.

Hong and Ahn (2015) studied future (2071-2100) early summer rainfall expectations over northeast Asia by downscaling two scenario projections of the HadGEM2-AO model (under CMIP5) to 12.5 km resolution with WRF. Their simulations show that extreme precipitation will enhance and meridionally migrating rainband will manifest itself ten days earlier over the Korean peninsula. They investigated the source of the increase in the total rainfall over the peninsula and vicinity regions by splitting the rainfall types into two categories: 1) Convective, and 2) Non-convective. According to the authors, convective precipitation dominates the non-convective one in the total increase. This is because the moist poleward flow and the moist static instability will increase while the change in the stationary front linked to the non-convective precipitation will be insignificant.

Wang and Kotamarthi (2015) searched future rainfall projections of North America by two scenarios of CCSM4 under CMIP5 representative concentration pathways (RCPs). They utilized bias-corrected and uncorrected variants of the CCSM4 in the downscaling process of WRF to check whether any improvement exists. According to the authors, no matter which variant is used, WRF downscaling simulations generally reduce biases and upgrade the spatial representation of the rainfall. Their future projections demonstrate a reduction (increment) of the rainfall intensity across the southwestern (the eastern) USA. They concluded that expected summer rainfall changes are significantly diverse between the parent model (CCSM4) and WRF model outputs.

Chang et al. (2016) investigated the spatio-temporal characteristics of rainstorms, including size, intensity, duration and frequency over the US and their “compensation mechanism” in response to the expected change in precipitation due to climate change. They employed the WRF model to downscale CCSM4 historical (1995-2004) and RCP8.5-based future (2085-2094) simulations to 12 km horizontal resolution. Like the PGW approach but with more complexity, they developed a model that combines NCEP Stage IV analysis data (in this study used as observations) with statistically defined changes in the precipitation characteristics derived from the RCP8.5 projection. They also developed an approach for determining and tracking rainstorms based on a clustering algorithm and concluded that the primary “compensating mechanism” is the decrease in the storm size; therefore, flood impacts would be to a smaller extent than those by intensity alone.

Meyer and Jin (2017) compared future projections of the CCSM4 RCP6.0 with its 1) downscaled and 2) bias-corrected and downscaled outputs in North American monsoon for 2068-2099. They employed the WRF model, which was previously calibrated with optimal physical parameterization by Meyer and Jin (2016), to downscale both outputs to 20 km horizontal resolution. According to the authors, increasing the resolution overcomes the suppressed-convection environment of a warmer troposphere through extra surface evaporation. Besides, it enhances the land-sea temperature gradient hence increasing moisture conveyance via higher potent southerly winds. As for bias-correction results, they concluded that it represents the seasonality of the atmospheric thermodynamics more properly and yields a stronger monsoon signal over the region.

Erler and Peltier (2017) conducted a climate change impact study over two basins in western Canada using the WRF model in downscaling the CESM model with different three initialization. They employed two WRF model configurations for each initialization and constructed ensembles of them. They set the horizontal resolution to 10 km and 30 km with two nested domains and utilized the RCP8.5 scenario for future projections. As a result, they stated that a shift from snow to rainfall to a large extent, weaker spring freshet and drier summers prevails in the

coast's basins due to warming. They added that the shift in runoff seasonality is a risk-increasing factor for floods in autumn over the same region.

Zhang and Colle (2018) explored the effect of the dynamical downscaling process on extratropical cyclones across eastern North America and the western Atlantic. They employed the WRF model to downscale two CMIP5 GCMs to 1° and 0.2° horizontal resolutions in reproducing historical (1986-2005) and future (2080-2099) winter projections. The authors asserted that the position and rate of the cyclones' occurrence are GCM-dependent (i.e. related to the far-reaching circulation), thus remaining nearly the same in the downscaling process. On the other hand, they found out that increasing the model resolution via a RCM (herein WRF) reduces bias in the cyclone intensity.

Zhang et al. (2019) analyzed the moisture flux fragmentally over the Tibetan Plateau employing the WRF model in downscaling the CCSM4 for the historical period (1980-2005) and CCSM4 RCP4.5 and RCP8.5 for the future period (2010-2100). They set the downscaling resolution (horizontal) to 30 km and used the GLDAS and ERA-Interim reanalysis data as a reference. They found out that improving resolution better represents precipitation and evaporation spatially, further yielding more accurate results for a seasonal mean of the annual average. The authors also found out that the dynamic component is governing the difference between precipitation and evaporation with the WRF in historical and future projections. In contrast, they asserted that the thermodynamic component governs the parent model's future projections, concluding that WRF simulations are less sensitive to warming.

Dutheil et al. (2020) explored the future precipitation conditions (2080-2100) over New Caledonia by employing the PGW approach to CMIP5 multi-model ensemble under the RCP8.5 scenario. They used the WRF model in simulating present-day climate (2000-2016) and downscaling NCEP2 reanalysis to 21 km and 4.2 km horizontal resolutions, respectively. To avoid sea surface temperature (SST) biases, they utilized the “emergent constraint” method, which relates current precipitation

biases and SST changes by a statistical approach. According to the authors, their simulations predict a %18 decrease in precipitation, contrary to the CMIP5 models that do not estimate any significant precipitation alterations over the region. On the other hand, they argued that bias-correction of the SST does not lead to an adjustment of the rainfall projections over New Caledonia in qualitative aspects.

Hunt et al. (2020) investigated the past, present and future of the western disturbances by dealing with specific 40 events over the western Himalayas with the convection-permitting WRF simulations. They followed the PGW approach and perturbed ERA-Interim reanalysis data with the climate change signals derived by RCP4.5 and RCP8.5 scenarios of the multi-model ensemble of 32 CMIP5 GCMs. They observed that net precipitation was unchanged between their pre-industrial and control experiments, however precipitation form shifts from snow to rainfall in the control runs. They added that net precipitation would increase and the mean freezing layer would climb 660 m more (in altitude) between present-day and RCP8.5 runs. In conclusion, the authors asserted that moistening of the tropical atmosphere, thus enhancing moisture flux entrance to the region may overwhelm attenuation in the western disturbances and contribute to net total precipitation increase.

Zhao et al. (2020) conducted a two-stage climate projection study over California for summertime. The first stage contains an adjustment of the CMIP5 CESM model biases (based on the NARR reanalysis data as ground truth) with the “improved linear bias correction method”. Afterwards, they downscaled the CESM data (by WRF) with and without bias correction and validated bias-corrected model outputs. The second stage contains a climate change impact study with bias-corrected and downscaled outputs of the CESM RCP6.0 for the future period, 2046-2055. The authors concluded that bias-corrected and downscaled outputs of the CESM model mostly reduce biases of the surface variables, i.e., surface temperature, relative humidity, and vertical variables, i.e., mean temperature, and wind speed. As for the future, they expect that mean temperature, water vapor mixing ratio, heat waves, and marine air penetration will increase throughout the region.

The referred studies for climate change projections worldwide have utilized the former versions of emission scenarios. Moreover, these studies generally underline that using high-resolution is crucial, especially over topographically complex regions. The PGW method has been preferred to represent uncertainty ranges in an ensemble form in the ultimate dynamically-downscaled outputs. The third study of this thesis is one of the first studies worldwide, perturbing the latest ERA5 reanalysis with the latest CMIP6 GCMs ensemble (PGW) to obtain km-scale resolution over the topographically complex region, EMBS.

CHAPTER 3

MATERIALS AND METHODS

3.1 Study area

The Mediterranean portrays its climate type between the arid subtropics and mild midlatitudes: warm to hot, dry summers and mild, wet winters. However, the Mediterranean region occupies a vast area with varied climatic features due to the presence of wide-ranging geographical features, i.e., the peninsulas, steep orography, gulfs, and islands of various sizes. For example, suppose the Marmara, the Aegean and the Black Sea are members of the Mediterranean region. In that case, the Anatolian Peninsula and surrounding regions represent a climatic transition zone. The Mediterranean and Aegean coasts show a typical Mediterranean climate, while the midland peninsula shows a continental semi-arid climate, i.e., hot and dry summers and cold and snowy winters. On the other hand, the Black Sea coasts and the Caucasus located in the northeast are four-season rainy. Subarctic climate prevails under the Siberian high in the peninsula's east, and high mountain ridges cause prolonged cold winters and short cool summers. All those regions described above are located in the Eastern Mediterranean Black Sea region (Fig. 3.1. EMBS; here, we define between ~ 22 - 53 °E and 33 - 45 °N). Locating in the centre of the EMBS, the geographic and climatic features of Türkiye, which is the region of interest of the first and second studies, were focused more elaborated in the following:

Surrounding by the Aegean, Mediterranean and Black Seas, Türkiye consists of two main peninsulas. The first peninsula is located in the eastern European territories, while the second and large one is located in western Asia (also referred to as Anatolian Peninsula or Asia Minor). Türkiye has $783,562$ km² of acreage between 36° N- 42° N and 26° E- 45° E coordinates. Along with the temperate mid-

latitude Mediterranean climate characteristics, considerably distinct climate types (i.e., continental and oceanic) are present with the effect of complex topography and high-mountain ranges. The mountain ranges in the south and north prevent passing through the marine effect to the inner regions. It leaves the inner regions under the continental climate with restricted precipitation. The maximum annual precipitation is measured over the eastern Black Sea Region with around 2200 mm. On the other hand, Türkiye's highest-acreage province, Konya, takes only around 320 mm precipitation yearly. The southern part of the country enjoys more temperatures than the other regions during the year. General Directorate of Meteorology (GDM) of Türkiye measured the highest (lowest) yearly mean temperature in Hatay-İskenderun (Kars-Sarıkamış) district with 21.3 °C (-0.2 °C) in 1962 (1960). The yearly mean temperature (precipitation) of Türkiye between 1970 and 2019 is 13.2 °C (623.7 mm) (GDM, 2019; Bağçacı et al., 2021).

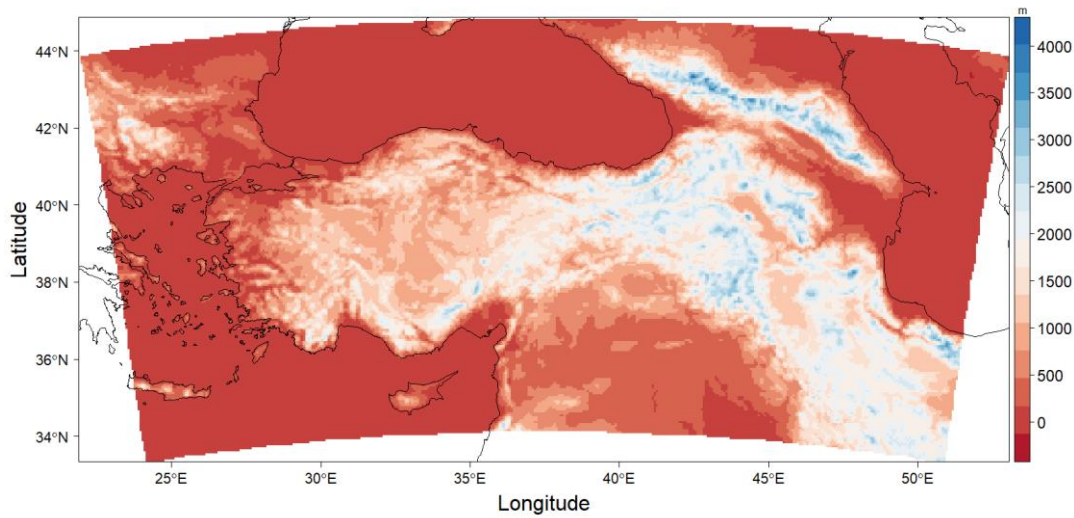


Figure 3.1. Study area (EMBS) elevation map. The first two studies, i.e., GCMs evaluation and their future projections and WRF sensitivity tests were conducted focusing the central Türkiye domain. The third study, i.e., PGW-based dynamic downscaling, was performed over the whole domain presented in the figure.

3.2 Datasets

The first study utilizes a total of 33 CMIP6 GCMs (Eyring et al., 2016) and 36 CMIP5 GCMs (Taylor et al., 2012), which are accessible to the public (<https://esgf-node.llnl.gov/projects/cmip5/> and <https://esgf-node.llnl.gov/projects/cmip6/>), in their comparative performance analysis. The model names, ensemble numbers (realizations, initializations, physics, and forcings), data availability, and horizontal resolutions are given in Table 3.1 and Table 3.2. Please see the Appendix of (Bağçacı et al., 2021) for further information and references of the data providers. The CMIP GCMs' performances are revealed by comparing them with the ERA5 reanalysis according to certain performance metrics. Before doing so, the validation of the ERA5 reanalysis data is performed with the ground measurements over the Türkiye domain. A total of 1045 relatively homogeneously distributed stations' monthly precipitation and near-surface temperature data were utilized in the validation (Bağçacı et al., 2021). Fig. 3.2 shows these stations' data availability/consistency, averaged to the nearest grid points.

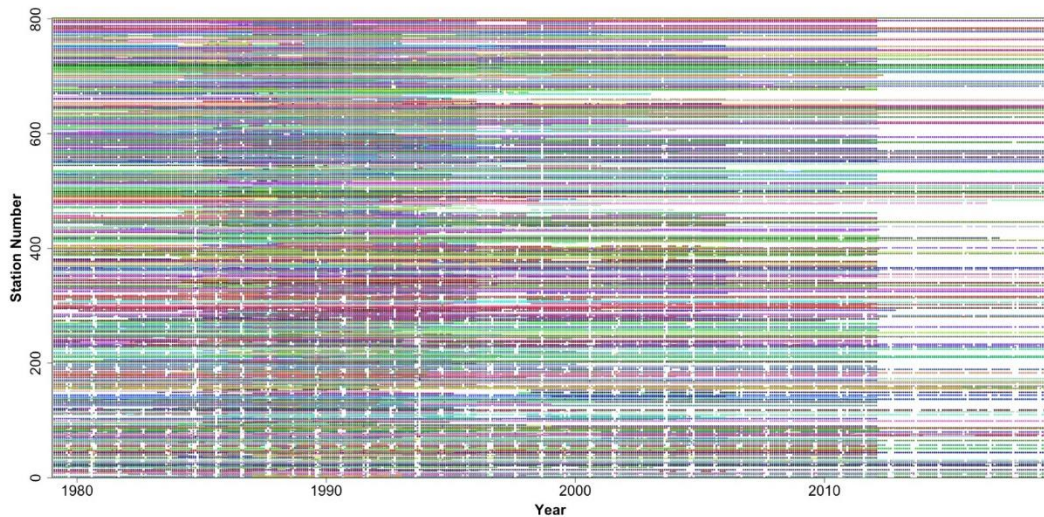


Figure 3.2. The data consistency/availability throughout the validation period of the first study

Table 3.1 Ensemble members, data availability, and spatial resolutions of CMIP5 GCMs employed in the study. Checkmarks for future simulations indicate at least one of RCPs (Bağçaci et al., 2021).

CMIP5 GCM	Ens. used	Historical sim.	Future sim.	Resolution (x°,y°)
ACCESS1.0	r1i1p1	√	√	1.9x1.3
ACCESS1.3	r1i1p1	√	√	1.9x1.3
BCC-CSM1.1	r1i1p1	√	√	2.8x2.8
BCC-CSM1.1(m)	r1i1p1	√	√	2.8x2.8
CanCM4	r1i1p1	√	√	2.8x2.8
CanESM2	r1i1p1	√	√	2.8x2.8
CESM1(BGC)	r1i1p1	√	√	1.3x0.9
CESM1(CAM5)	r1i1p1	√	√	1.3x0.9
CESM1(FASTCHEM)	r1i1p1	√	x	1.3x0.9
CESM1(WACCM)	r1i1p1	√	√	2.5x1.9
CNRM-CM5	r1i1p1	√	√	1.4x1.4
CNRM-CM5-2	r1i1p1	√	x	1.4x1.4
GFDL-CM3	r1i1p1	√	√	2.5x2.0
GISS-E2-H	r1i1p1	√	√	2.5x2.0
GISS-E2-H-CC	r1i1p1	√	√	2.5x2.0
GISS-E2-R	r1i1p1	√	√	2.5x2.0
GISS-E2-R-CC	r1i1p1	√	√	2.5x2.0
HadCM3	r1i1p1	√	√	3.8x2.5
HadGEM2-AO	r1i1p1	√	√	1.9x1.3
HadGEM2-CC	r1i1p1	√	√	1.9x1.3
HadGEM2-ES	r1i1p1	√	√	1.9x1.3
INM-CM4	r1i1p1	√	√	2.0x1.5
IPSL-CM5A-LR	r1i1p1	√	√	3.8x1.9
IPSL-CM5A-MR	r1i1p1	√	√	2.5x1.3
IPSL-CM5B-LR	r1i1p1	√	√	3.8x1.9
MIROC4h	r1i1p1	√	√	0.6x0.6
MIROC5	r1i1p1	√	√	1.4x1.4
MIROC-ESM	r1i1p1	√	√	2.8x2.8
MIROC-ESM-CHEM	r1i1p1	√	√	2.8x2.8
MPI-ESM-LR	r1i1p1	√	√	1.9x1.9
MPI-ESM-MR	r1i1p1	√	√	1.9x1.9
MPI-ESM-P	r1i1p1	√	x	1.9x1.9
MRI-CGCM3	r1i1p1	√	√	1.1x1.1
MRI-ESM1	r1i1p1	√	√	1.1x1.1
NorESM1-M	r1i1p1	√	√	2.5x1.9
NorESM1-ME	r1i1p1	√	√	2.5x1.9

Table 3.2 Ensemble members, data availability, and spatial resolutions of CMIP6 GCMs employed in the study. Checkmarks for future simulations indicate at least one of SSPs (Bağçaci et al., 2021).

CMIP6 GCM	Ens. used	Historical sim.	Future sim.	Resolution (x°,y°)
ACCESS-CM2	r1i1p1f1	√	√	1.9x1.3
ACCESS-ESM-1-5	r1i1p1f1	√	√	1.9x1.3
BCC-CSM2-MR	r1i1p1f1	√	√	1.1x1.1
BCC-ESM-1	r1i1p1f1	√	√	2.8x2.8
CAMS-CSM1-0	r1i1p1f1	√	√	1.1x1.1
CanESM5	r1i1p1f1	√	√	2.8x2.8
CESM2	r1i1p1f1	√	√	1.3x0.9
CESM2-WACCM	r1i1p1f1	√	√	1.3x0.9
CNRM-CM6-1	r1i1p1f2	√	√	1.4x1.4
CNRM-CM6-1-HR	r1i1p1f2	√	√	0.5x0.5
CNRM-ESM2-1	r1i1p1f2	√	√	1.4x1.4
EC-Earth3	r1i1p1f1	√	√	0.7x0.7
EC-Earth3-Veg	r1i1p1f1	√	√	0.7x0.7
GFDL-ESM4	r1i1p1f1	√	√	1.3x1.0
GISS-E2-1-G	r1i1p1f1	√	√	2.5x2.0
HadGEM3-GC31-LL	r1i1p1f3	√	√	1.9x1.3
HadGEM3-GC31-MM	r1i1p1f3	√	x	0.8x0.6
INM-CM4-8	r1i1p1f1	√	√	2.0x1.5
INM-CM5-0	r1i1p1f1	√	√	2.0x1.5
IPSL-CM6A-LR	r1i1p1f1	√	√	2.5x1.3
MCM-UA-1-0	r1i1p1f1	√	x	3.8x2.2
MIROC6	r1i1p1f1	√	√	1.4x1.4
MIROC-ES2L	r1i1p1f2	√	√	2.8x2.8
MPI-ESM-1-2-HAM	r1i1p1f1	√	√	1.9x1.9
MPI-ESM1-2-HR	r1i1p1f1	√	√	0.9x0.9
MPI-ESM1-2-LR	r1i1p1f1	√	√	1.9x1.9
MRI-ESM2-0	r1i1p1f1	√	√	1.1x1.1
NESM3	r1i1p1f1	√	√	1.9x1.9
NorESM2-LM	r1i1p1f1	√	√	2.5x1.9
NorESM2-MM	r1i1p1f1	√	√	1.3x0.9
UKESM1-0-LL	r1i1p1f2	√	√	1.9x1.3

The second study utilizes ERA5 reanalysis, which is the latest release of the European Centre for Medium-Range Weather Forecast (ECMWF), as a parent model for the WRF. ERA5 reanalysis presents higher horizontal and vertical resolutions (31 km, $\sim 0.25^\circ$; 137 vertical levels topped at one hPa) than its predecessor, ERA-Interim (79 km, $\sim 0.75^\circ$; 60 vertical levels topped at ten hPa). The radiative forcings, i.e., GHGs' and aerosols' progressively spread, are also taken into account with the ERA5 reanalysis, as similar to the CMIP GCMs (Hersbach et al., 2019). Accordingly, climatic change (i.e., global warming effects in the Arctic region) is observable with the ERA5 reanalysis between its operational period, 1979 to the present day. The atmospheric data assimilation, where a larger size and higher quality of observations (more satellite and radar data included) is employed, is performed with an ensemble. The higher quality of observations, also including, of course, traditional ground measurements, enables the more consistent 'maps without gaps' with the state-of-the-art specification, calibration, and process of the data (Hersbach et al., 2019; Bağçacı et al., 2021). These are some improvements of the ERA5 reanalysis according to the ERA-Interim, which enable more realistic meteorological outputs, especially precipitation.

The retrieved data at the atmospheric vertical level from the ERA5 reanalysis are geopotential height, air temperature, wind components (U and V), and relative humidity. These data are also retrieved at the near-surface level (except geopotential height), besides dew-point temperature, surface pressure, sea-level pressure, sea-surface temperature, water equivalent of the accumulated snow depth, physical snow depth, snow density and sea-ice fraction. The soil moisture and temperature are also retrieved at the vertical ground level.

In the third study, 13 CMIP6 GCMs under the SSP5-8.5 emission scenario (Table 3.3) were utilized in an ensemble in the perturbation process. These 13 were selected according to their performances (Bağçacı et al., 2021) and relatively high resolution, among other GCMs. We have selected GCMs not exceeding four times ERA5 spatial resolution as far as possible to alleviate information loss in the bilinear interpolation.

The retrospective dynamic downscaling simulations were performed using the ERA5 reanalysis as a parent model.

Table 3.3 Ensemble members, variant label (ens. used), and horizontal resolutions of CMIP6 GCMs used in the PGW-based dynamic downscaling study.

CMIP6 GCM	Ens. used	Resolution (x°,y°)
AWI-CM-1-1-MR	r1i1p1f1	0.94x0.94
BCC-CSM2-MR	r1i1p1f1	1.10x1.10
CMCC-CM2-SR5	r1i1p1f1	1.25x0.94
CMCC-ESM2	r1i1p1f1	1.25x0.94
CNRM-CM6-1-HR	r1i1p1f2	0.50x0.50
EC-Earth3	r1i1p1f1	0.70x0.70
EC-Earth3-CC	r1i1p1f1	0.70x0.70
EC-Earth3-Veg	r1i1p1f1	0.70x0.70
FGOALS-f3-L	r1i1p1f1	1.25x1.00
GFDL-ESM4	r1i1p1f1	1.30x1.00
HadGEM3-GC31-MM	r1i1p1f3	0.80x0.60
MPI-ESM1-2-HR	r1i1p1f1	0.90x0.90
MRI-ESM2-0	r1i1p1f1	1.13x1.12

3.3 Methodology

3.3.1 Performance metrics for evaluation of the CMIP5 and CMIP6

The modified index of agreement (md), normalized root mean square error (nRMSE), Kling-Gupta efficiency (KGE), and spatial efficiency (SPAEF) metrics were utilized to reveal the individual model performance rankings of the retrospective CMIP5 and CMIP6 GCMs simulations in the context of the first study. The comprehensive performance metric (MR) (Jiang et al., 2015) was computed based on the GCMs prioritization for both near-surface temperature and precipitation

data. The top four best-performing GCMs in each CMIP5 and CMIP6 are distinguished to compose multi-model ensembles (MMEs) for precipitation and near-surface temperature separately. The more detailed explanation and formulas of the performance metrics can be found in the author's published study (Bağçacı et al., 2021).

3.3.2 Regional climate model (RCM): WRF

This thesis uses the WRF model (Skamarock et al., 2008) as a regional climate model (RCM). Although it is a numerical weather prediction system (NWP) widely used in operational weather forecasts, it is also used in atmospheric research fields, including climate prediction. As a new generation of the fifth Mesoscale Model (MM5, Grell et al., 1994), the WRF model offers higher-order numerics, conservative solutions, and parallel computing, which are required in the smaller atmospheric scales (Powers et al., 2017). Besides the improvement on the dynamical solver (cores), the WRF model also has a wide range of physics schemes contributed by researchers around the world. Basically, WRF has two components to run a simulation: 1) Preprocess of the model domain, preparation of the input data (including data interpolation), and transition between data types, 2) Generation of initial and boundary conditions and running the WRF model. The first item is under the umbrella of the WRF Preprocessing System (WPS), which has geogrid, ungrib, and metgrid steps. The second item is composed of the real and run steps in the climate modelling (the running can be also an ideal case for research purposes). The following items explain these steps (the first three indicate WPS steps, while the last two indicate WRF steps) in more detail and Fig. 3.3 shows a summary flowchart of the WRF modelling.

i) Geogrid: In the first step of WPS, the geogrid executable is run to interpolate terrestrial data (geographical information) to the model domain. This data broadly consists of orography, topography, soil type, land use, albedo (including snow), land area index, the variance of subgrid-scale orography, and vegetation fraction. The geographic data is taken from the Moderate Resolution Imaging Spectroradiometer

(MODIS). The WRF model allows studying with nested domains. The map projection options of the WPS are 1) polar stereographic, 2) Lambert-Conformal, 3) Mercator, and 4) latitude-longitude. Here we have chosen Lambert-Conformal-Conic (LCC) projection type since it is suggested for the mid-latitudes.

ii) Ungrib: This executable reads and extracts meteorological fields from GRIB-formatted files with a single processor and writes them to the intermediate file format. The GRIB-formatted files come from another RCM or GCM as a parent model to the WRF. The WRF model converts these GRIB-formatted data according to the variable table (Vtable). The composed intermediate files are later on read by metgrid executables.

iii) Metgrid: This executable horizontally interpolates intermediate meteorological data extracted from the GRIB format on the study domain. The interpolation method and mask options are written in the METGRID.TBL. The metgrid executable writes the data in various formats; however, we have selected the NetCDF option to easily monitor outputs.

iv) Real: This executable creates a final form of the data, which has initial and boundary conditions, just prior to running WRF. The vertical data interpolation is performed in this step. If the sea-surface temperature (SST) update and spectral nudging options are switched on, this step also prepares the files related to these options. We have switched on the SST update option in the sensitivity and PGW-based dynamic downscaling, while spectral nudging was only switched on in the latter study. This is because spectral nudging is generally recommended for larger domain sizes than the Türkiye domain.

v) WRF: This executable ultimately conducts dynamic downscaling of the initial conditions. Once the initial condition has been downscaled, WRF creates its own initial conditions by updating the data in the indicated time steps. The physics options, i.e., cumulus, microphysics, planetary boundary layer, radiation, and surface, are interactively operated to obtain the new state of the meteorological variables (Skamarock et al., 2019). Fig. 3.4 shows this interaction, where cloud and

precipitation processes are mainly governed by microphysics and cumulus parameterization schemes. In the lower atmospheric levels, PBL and surface physics handle the new state of the near-surface atmospheric variables. Precipitation directly affects the surface, and clouds directly affect radiation, while radiation both affects the surface (via downward shortwave and longwave radiation) and is affected by the surface (surface emission and albedo).

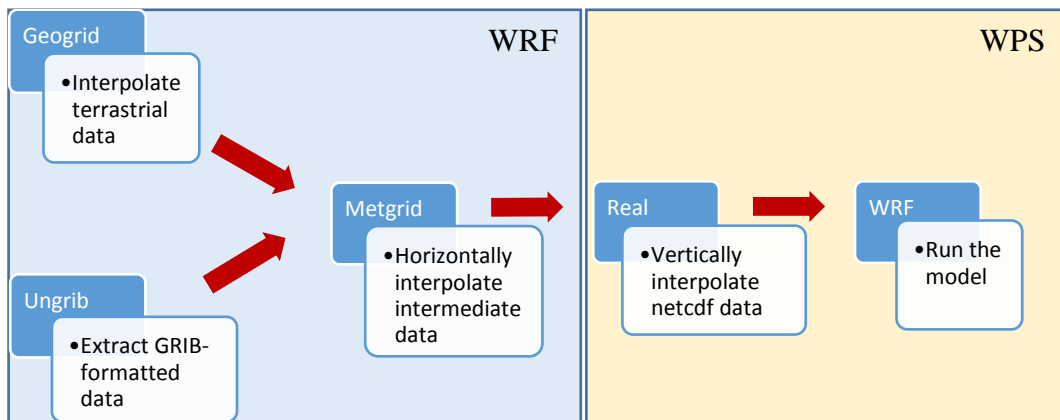


Figure 3.3. The summary flowchart of the WRF modelling

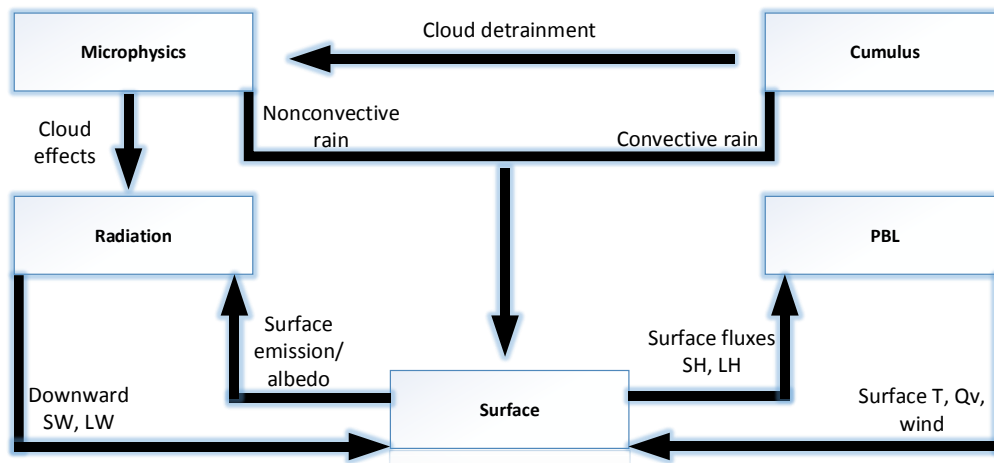


Figure 3.4. WRF physics parameterizations interactions. We adapted this figure directly from Skamarock et al. (2019).

3.3.3 WRF configurations

The second study utilizes the ERA5 reanalysis data as a parent model in the WRF dynamic downscaling-based sensitivity tests. The WRF model was configured with the unique five microphysics schemes, four cumulus schemes, and three planetary boundary layer schemes in a combination manner. Accordingly, a total of 60 different combined physics options were used for running WRF. The utilized microphysics schemes are Kessler (Kessler, 1969), Lin et al. (Lin Purdue) (Lin et al., 1983), WRF Single-Moment 6-class (WSM6) (Lim and Jade, 2006), New Thompson et al. (Thompson) (Thompson et al., 2008), and Morrison double-moment (Morrison 2-mom) (Morrison et al., 2009). The utilized cumulus schemes are Kain-Fritsch (Kain and Kain, 2004), Betts-Miller-Janjic (Janjic, 1994; Janjić, 2000), Tiedtke (Tiedtke, 1989; Zhang et al., 2011). The cumulus scheme option was switched off as the fourth option. The utilized planetary boundary layer schemes are Yonsei University (YSU) (Hong et al., 2006), Mellor-Yamada-Janjic (MYJ) (Janjic, 1994), and Asymmetric Convective Model with non-local upward mixing and local downward mixing (ACM2) (Pleim, 2007a, 2007b).

In the context of the sensitivity study, the Weather Research and Forecasting (WRF) model Version 4.3 was configured for the Türkiye domain, which has 420 x 222 corresponding grid points with 4 km horizontal grid spacing. The total domain size is 1680 km in the west-east direction and 888 km in the south-north direction. There are 40 vertical levels topped at 50 hPa. The time step for integration is 24 s. Besides the parameterization schemes mentioned above, the Rapid Radiative Transfer Model (RRTMG) (Iacono et al., 2008) and the Noah land surface model (Chen and Dudhia, 2001) were employed. The WRF simulations were performed for the year 2020, whereas the simulations were started two months before the one-year periods as model spinups, which were discarded later. The model was forced with the 6-hourly $\sim 0.25^\circ$ ERA5 reanalysis data to obtain the targeted 4-km resolution. This resolution was found suitable for directly dynamic downscaling $\sim 0.7^\circ$ ERA-Interim data without the need for any extra intermediate coarse grid in a one-way

nested configuration (Liu et al., 2017; Li et al., 2019; Ikeda et al., 2021). Therefore, we have not utilized any intermediate domain with a coarser resolution than 4 km between ERA5 reanalysis and the WRF domain. It should be noted that sea-surface temperature was updated in the 6-hourly periods. We have utilized a total of 836 stations, which are mostly Automated Weather Observing Systems (AWOS), in the validation and sensitivity of the WRF-sensitivity configurations.

In the PGW-based dynamic downscaling (the third study), the WRF model Version 4.3 was used as an RCM. The GHGs concentration based on the latest released CMIP6 SSP5-8.5 was obtained from Version 4.3.1. The WRF model was configured for the domain covering Bulgaria, eastern Greece, Türkiye, Cyprus, northern Syria, northern Iraq and northern Iran, Armenia, Georgia, Azerbaijan, and Russian territory near the Caucasus (Fig. 3.1). The domain also covers the Aegean Sea, Black Sea, northeastern Mediterranean Sea, and most Caspian Sea. To remind, we called this domain EMBS, which has 625 x 300 corresponding grid points with 4-km horizontal grid spacing. The total domain size is 2500 km in the west-east direction and 1200 km in the south-north direction. There are 40 vertical levels topped at 50 hPa. Spectral nudging was performed with a wavenumber 2 in the x-direction and 1 in the y-direction, corresponding to 1250 and 1200 km wavelengths, respectively. The relatively weak nudging coefficients (0.0003 s^{-1}) was used to do not dominantly intervene the model to evolve freely. The geopotential, temperature and horizontal wind components were nudged above the planetary boundary layer (PBL). The time step for integration is 24 s. The utilized parameterization schemes are the new Thompson microphysics scheme (Thompson et al., 2008), the Yonsei University (YSU) planetary boundary layer scheme (Hong et al., 2006), the Rapid Radiative Transfer Model (RRTMG) (Iacono et al., 2008), and the Noah land surface model (Chen and Dudhia, 2001). Here we switched on the cumulus parameterization option with the Tiedtke scheme (Tiedtke, 1989; Zhang et al., 2011) since this option has yielded better precipitation results than convection-permitting simulations over the Türkiye domain in 2020.

3.3.4 PGW process

Two 20-year WRF simulations were performed based on the IPCC assessment report (AR6) baseline period, 1995-2014, and the corresponding pseudo future period. Both simulations were started one year before the 20-year periods as model spinups, which were discarded later. In the first experiment, the model was forced with the 6-hourly $\sim 0.25^\circ$ ERA5 reanalysis data to obtain retrospective simulations in the targeted 4-km resolution.

The second experiment is based on the perturbation of the ERA5 reanalysis data with the climate change signal derived from GCM ensemble (13 CMIP6 GCMs) under the SSP5-8.5 emission scenario to obtain pseudo future period simulations. The following formula can simply explain the general picture of the PGW forcing:

$$PGW_{forcing} = ERA5_{1995-2014} + \Delta CMIP6_{SSP585-historical} \quad (11)$$

where $\Delta CMIP6_{SSP585-historical}$ is the 30-year CMIP6 MME mean monthly differences:

$$\Delta CMIP6_{SSP585-historical} = CMIP6_{2071-2100} - CMIP6_{1985-2014} \quad (12)$$

The perturbation was made for both surface and pressure levels after the step, where monthly MME mean differences were interpolated to 6-hourly periods. The mandatory data fields in the PGW perturbation to force the WRF model are shown in Table 3.4. The perturbed surface variables are the near-surface humidity and temperature, eastward and northward wind components at 10 m, sea-level and surface pressures, skin, sea-surface, and soil temperatures. In the pressure level, relative humidity, eastward and northward wind components, air temperature, and geopotential of the GCMs were first vertically interpolated to ERA5 levels and then used for the perturbation in the MME context. Fig. 3.5 shows the more detailed step-by-step procedure of the PGW methodology, where the first step is the combination of the first two equations. Initially, the vertical (linear) and horizontal (bilinear) interpolation was made to equate the vertical and horizontal resolution of GCMs to

those of ERA5, respectively. Afterwards, the monthly means of the GCMs were calculated both for the historical (1985-2014) and future (2071-2100) period, where the period means were later used in the construction of MMEs. Then, Δ_change (difference between future and historical period MMEs) were obtained and interpolated to 6-hourly periods (time interpolation). In the last step, the perturbation (adding time interpolated Δ_change to 6-hourly ERA5 reanalysis) was made for both surface and pressure levels to construct PGW-forcing dataset. The perturbed surface variables are the near-surface humidity and temperature, eastward and northward wind components at 10 m, sea-level and surface pressures, skin, sea-surface, and soil temperatures. In the pressure level, these variables are relative humidity, eastward and northward wind components, air temperature, and geopotential.

Table 3.4 Mandatory data fields in the PGW perturbation to force RCM (WRF).

Surface level	Near-surface relative humidity	Pressure level	Relative humidity
	Near-surface temperature		
	U10 (eastward wind)		Eastward wind
	V10 (northward wind)		Northward wind
	Sea-level pressure		
	Surface pressure		
	Skin temperature		Air temperature
	Sea-surface temperature		
	Soil temperature		Geopotential height

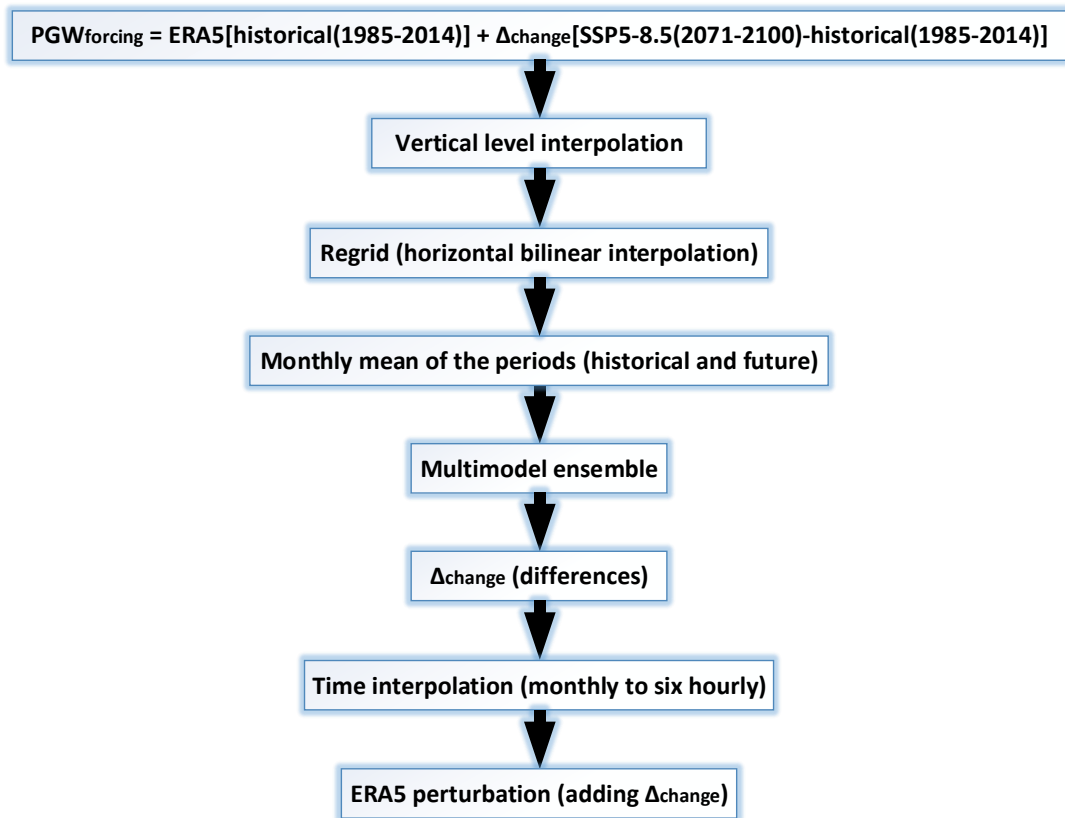


Figure 3.5. The PGW methodology flowchart

3.3.5 Model verification with the PGW retrospective simulations

We have employed ground observations and three gridded datasets to verify precipitation, and the ground observations and two gridded data sets to verify near-surface temperature results of the WRF retrospective simulation. The ground observations were retrieved from Türkiye's General Directorate of Meteorology (GDM) for the Türkiye domain, covering a considerable amount of the study area's land surface. There are 273 station data records for the daily and 614 station data records for the monthly precipitation validation in Türkiye. For the near-surface temperature validation, these numbers are 417 and 1506, respectively. Besides, the 119 station data records, which were retrieved from the World Meteorological Organization (WMO), were used in the near-surface temperature validation for the stations outside Türkiye. We have also utilized the Global Precipitation Climatology

Centre (Schneider et al., 2022) monthly precipitation dataset in 0.25 ° resolution, HOAPS/GPCC (Schröder et al., 2019) global daily precipitation data record in 0.5 ° resolution, E-OBS (Cornes et al., 2018) daily precipitation and the near-surface temperature product in 0.1 ° resolution, and the Climate Research Unit at the University of East Anglia (CRU version 3.22, 1901–2013; Harris et al. (2014)) monthly near-surface temperature product in 0.5 ° resolution. The WRF simulations were regridded to each gridded product's native resolution in validation. The gridded observation datasets cover entire EMBS domain except E-OBS, which ends up grids at 45 ° E. Nevertheless, it gives observation over the most of the domain. We have taken the monthly mean of the gridded daily precipitation in validation since the measurements of 24-hour time period precipitation may largely vary (midnight to midnight or morning to morning measurement) across the countries (ECMWF, 2020).

CHAPTER 4

RESULTS

4.1 Results of the GCM evaluation and future projections

4.1.1 Validation of ERA5 temperature and precipitation

Fig. 4.1 shows the monthly and monthly average statistics of precipitation and near-surface temperature between 1979 and 2019. According to the month-to-month comparison of ground observations and ERA5 reanalysis nearest that observation, the correlation value of precipitation is 0.81 (Fig. 4.1 a). The standard deviations of the ERA5 reanalysis and ground observations are 54.6 mm and 56.6 mm, respectively. It offers that extremes are more likely for the ground observations, which are not quite strictly captured by ERA5 reanalysis, having more consistent data. This situation manifests itself in precipitation values, especially higher than 600 mm, which ERA5 underestimates them. The linear regression line equation shows more spread views, and the residual standard error (SE_r) is higher with the value of 32.36 mm than the monthly average statistics.

The ERA5 reanalysis performs better in monthly averaged precipitation regarding superior correlation (0.83) and fewer SE_r (23.33 mm) (Fig. 4.1 b). The standard deviations for ERA5 reanalysis and ground observations are 41.8 mm and 40.2 mm, respectively. In the monthly average case, the standard deviation of the ERA5 reanalysis is closer to the ground observations, even a little bit higher than it. It shows that the extremes are compensated with the lower values. On the other hand, it should be underlined that stations' data consistency throughout the validation period (Fig. 3.2). For example, the red point in Fig. 4.1 b belongs to a station, which only contributes to the observations with the data between 1984 and 1986. This station is situated in the Taurus mountains, where orographic precipitation prevails.

This precipitation type should be validated with more observations and frequent ground observation networks. However, these are lacking, which grows the error (in terms of precipitation statistics) in the comparison process between the station and ERA5 reanalysis.

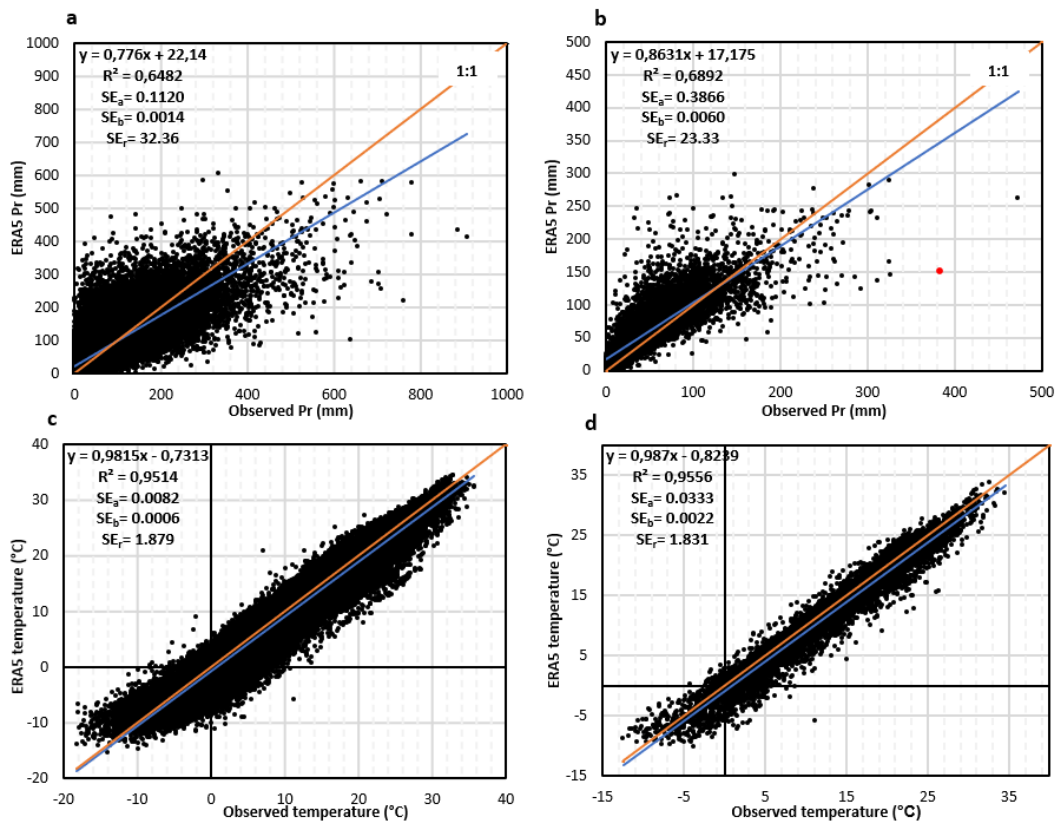


Figure 4.1. Comparison of the ERA5 reanalysis and station a) monthly precipitation, b) monthly mean precipitation, c) monthly near-surface temperature, d) monthly mean near-surface temperature. The related statistics are given in the figure, and more detailed information can be found in the original article of Bağcıci et al. (2021).

The monthly (month-to-month) and monthly mean near-surface temperature correlations are 0.98, while SEr values are 1.88 °C and 1.83 °C, respectively, between ERA5 reanalysis and ground observations (Fig. 4.1 c and Fig. 4.1 d). It shows a bias pattern which is spatiotemporally focused in one of the following sections. In addition to this, standard deviations are closer to each other (differences are below 0.1 °C) than those of precipitation, showing that extremes in near-surface

temperatures are quite reasonably captured by ERA5. Overall, ERA5 reanalysis demonstrates reasonably satisfying success for both variables. Henceforth, the ERA5 reanalysis will be employed as base-data in the performance assessment of the CMIP5 and CMIP6 GCMs (Bağçacı et al., 2021).

4.1.2 Performance assessment of the CMIP5 and CMIP6

Concerning the temporal and spatiotemporal metrics, i.e., md, nRMSE, SPAEF, and KGE, we have assessed the CMIP5 and CMIP6 GCMs performances based on the ERA5 reanalysis over the Türkiye domain. Results show that different climate modelling groups' GCMs dominate CMIP5 and CMIP6 according to the ultimate MR ranks. For example, MIROC4h, MIROC5, CESM1 (FASTCHEM), CESM1 (BGC) outperform in precipitation simulations in CMIP5, while HadGEM-GC31-MM, GFDL-ESM4, ACCESS-CM2, and EC-Earth3 are best-performing GCMs in CMIP6. The best-performing GCMs in simulating near-surface temperatures are CESM1 (CAM5), MIROC4h, IPSL-CM5A-MR, MRI-ESM1, and MPI-ESM1-2-HR, CNRM-ESM2-1, NorESM2-MM, MRI-ESM2-0, in CMIP5 and CMIP6, respectively. These show the importance of reevaluation of the GCMs with updated versions of the CMIPs since, alongside the dominance of different climate groups, there is also an increase in the performance of the top-performing models in CMIP6 over those in CMIP5. This performance increase is pronounced for precipitation simulations, while it is indistinctive for near-surface temperature simulations. The complete performance ranks can be found in the original article of Bağçacı et al. (2021). With the four-best-performing models mentioned above, we composed the near-surface temperature and precipitation ensembles individually; however, for the SSP2-4.5 scenario, we used the CNRM-CM6-1-HR model instead of HadGEM-GC31-MM due to the missing data.

The CMIP6 GCMs show less inter-model variability than CMIP5 GCMs in simulating precipitation. Fig. 4.2 affirms this fact in the ensemble members' precipitation simulations and worst-performing GCMs in CMIP5 and CMIP6. With

the more consistent simulations, the CMIP6 also shows improvement in the mean absolute error (MAE) with 2 mm (~ 16 mm for CMIP6 and ~ 18 mm for CMIP5). However, a major improvement is in the R^2 value, with nearly ten percent (0.68 for CMIP6 and 0.59 for CMIP5). Underestimation and overestimation of precipitation extremes are largely reduced with the CMIP6 GCMs compared to the CMIP5, which is already reflected in the statistical values.

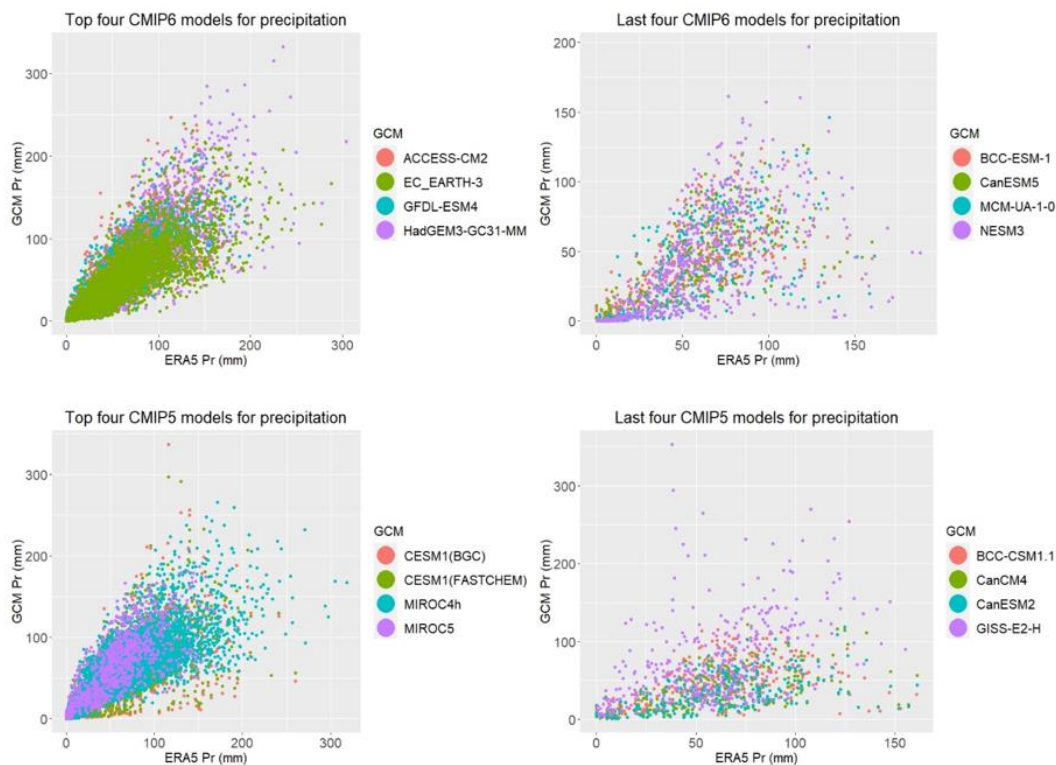


Figure 4.2. Comparison of the best four- and worst four-performing CMIP6 and CMIP5 GCMs with ERA5 for precipitation (Bağçaci et al., 2021).

Fig. 4.3 illustrates the same as in Fig. 4.2 but for near-surface temperature. Since uncertainties in simulating near-surface temperature are far less than precipitation and it can be more accurately simulated, the performance improvement is not substantial with the CMIP6 GCMs compared to the CMIP5. The same R^2 values are present with 0.96 value, while improvement with the CMIP6 is only 0.1 °C in MAE (~ 1.4 °C for CMIP6 and ~ 1.5 °C for CMIP5). The error value gap is similar in the worst-performing GCMs; however, R^2 statistics six percent better in favor of CMIP6

(0.87 for CMIP6 and 0.81 for CMIP5). Moreover, the worst-performing CMIP5 GCMs have a more dispersed view than the CMIP6, affirming that CMIP6 GCMs simulations show more consistency with less intermodel variability, similar to precipitation simulations.

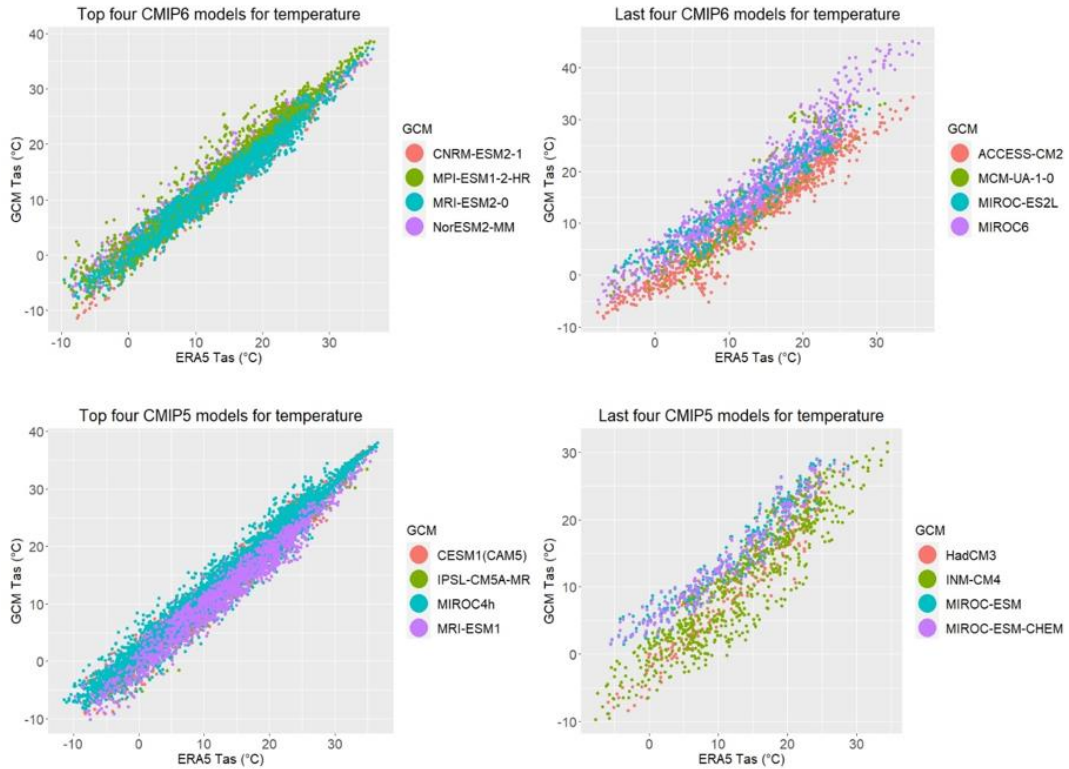


Figure 4.3. Comparison of the best four- and worst four-performing CMIP6 and CMIP5 GCMs with ERA5 for near-surface temperature (Bağçacı et al., 2021).

4.1.3 Biases in the ensemble means of the CMIP5 and CMIP6

In the territories of Türkiye, mostly a cold bias exists in all seasons, while a warm bias exists over the Black Sea in the winter and spring seasons and the Aegean Sea in summer, both with the CMIP5 and CMIP6 MME (Fig. 4.4). The cold bias up to 2 °C greatly reduces with the CMIP6 in the fall season (around 1 °C), while reduction in the winter season is still pronounced, though not as much in fall. There is a significant winter temperature bias with the CMIP6 in the Eastern Black Sea region

of Türkiye (around 3.2 °C), which reduces the land-sea temperature contrast. If the same GCMs were used in the ensembles, this result could affect the orographic precipitation in the region. As for precipitation, a wet bias prevails over most of Türkiye with both CMIPs. A dry bias is present over the Eastern Black Sea region of Türkiye in the summer and fall seasons and the Mediterranean coasts and southeastern regions of the country in winter, where its magnitude is potent in summer and winter with the CMIP5 MME. The wet bias substantially reduces in winter (up to 50 mm), while other seasons show also large reduction, though not as much in winter. These results affirm a performance improvement of the CMIP6 in a spatiotemporal manner.

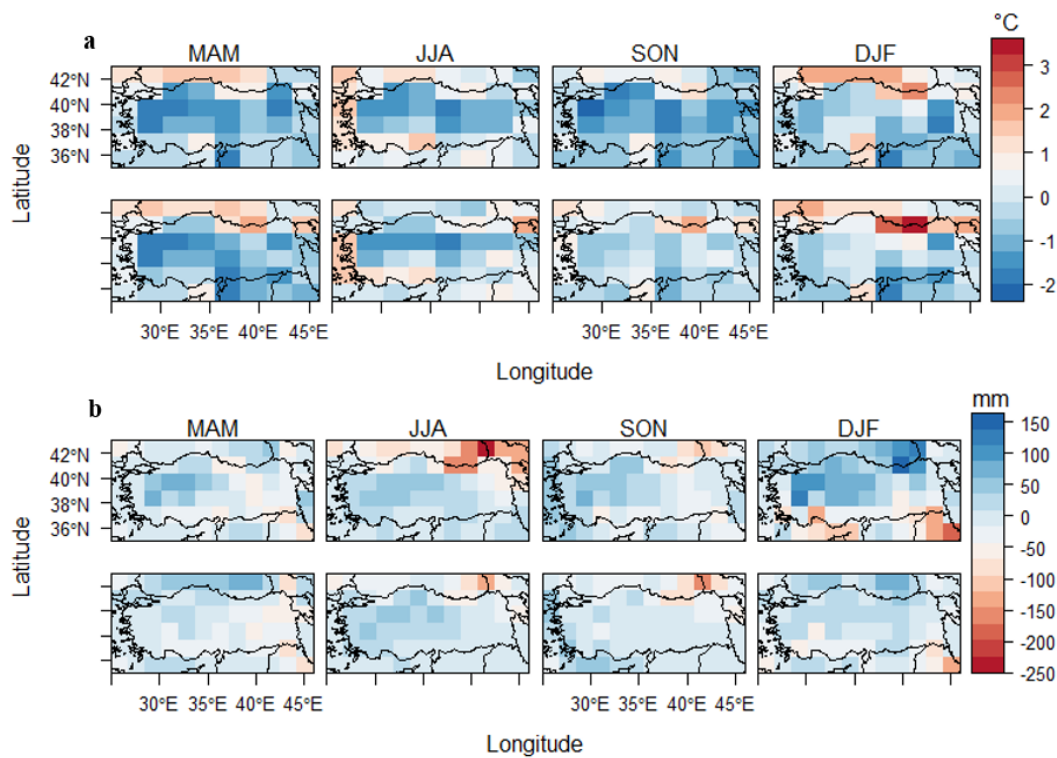


Figure 4.4. The mean biases in a) near-surface temperature and b) precipitation. The CMIP5 is in the first and CMIP6 in the second rows. The ensemble members are regridded to the coarsest-resolution GCM's horizontal resolution, and then seasonal means are taken in the historical periods of the CMIP5 and CMIP6 individually (Bağçacı et al., 2021).

4.1.4 Future projections

To put forth possible future changes in the near-surface temperature and precipitation, we have used the 1995-2014 period (GCMs' means are computed in this historical period) as a baseline according to the IPCC assessment report (AR6) and three future periods, i.e., near- (2030-2050), mid- (2050-2070), and long-term (2070-2100) with the SSP2-4.5 and SSP5-8.5 of CMIP6. The seasonal mean changes projections are obtained for the near-surface temperature and precipitation individually with their four-model-ensembles which were selected according to their performances mentioned above. The following gives the results of these changes between future projections and historical simulations.

4.1.4.1 Precipitation

The expected seasonal precipitation changes in winter closely resemble each other between SSP2-4.5 and SSP5-8.5 over the Türkiye domain in the long-term (Fig. 4.5 c and Fig. 4.6 c). The decrement in the south and increment in the north are both statistically significant at $p=0.05$ level. Moreover, except in southwestern Türkiye, which shows a decrease, and northwestern Türkiye, which shows an increase, no changes are statistically significant in the near term (Fig. 4.5 a and Fig. 4.6 a). The southern regions partly show a significant decrease with SSP2-4.5, while this decrease is more widespread and more potent with SSP5-8.5 in the medium term (Fig. 4.5 b and Fig. 4.6 b). The northern country has a statistically significant precipitation increase with the SSP2-4.5, while there are no significant changes with the SSP5-8.5 in the same term. It should be noted that Southeastern Anatolia Region commonly does not show a statistically significant winter precipitation decrease with the SSP2-4.5 and SSP5-8.5 in all terms, which is opposed to Önel and Semazzi (2009). Moreover, the winter precipitation enhancement in the Black Sea Region of Türkiye would be significant but not surpasses 10% in the long period according to the SSP2-4.5 and SSP5-8.5, where Önel and Semazzi (2009) found this increase

10%-50% in the same period, using a high-emission scenario under the earlier version of CMIP, CMIP3.

The summer precipitation decrease is statistically significant and countrywide with the SSP2-4.5, while a decrease in the centre and southern parts of Türkiye is not significant with the SSP5-8.5 in the long term. It is most likely due to the fact that warmer projections with SSP5-8.5 increase convective precipitation events over the central and southern regions of Türkiye. In the medium term, the statistically significant decrease has a similar pattern between the two scenarios in the west and north, while the decrease in the northeast propagates to the south more with the SSP2-4.5. The statistically significant decrease is restricted with the north with the two scenarios in the near-term, except in the same south propagated areas with the SSP2-4.5. It should be noted that our projections show a statistically significant precipitation decrease over eastern Türkiye with the SSP2-4.5 in the medium term, similar to Demircan et al. (2017), who found a 30% summer precipitation decline over the same region in the same term with their dynamically downscaled simulation of three GCMs under the RCP4.5.

The long-term spring precipitation changes are completely different between the SSP2-4.5 (no statistically significant decrease) and the SSP5-8.5 (statistically significant decrease) in terms of statistical significance. However, two scenarios agree on a significant precipitation increase in the northeastern domain. On the other hand, there are almost no changes with the SSP5-8.5, except an increase in northeastern Türkiye, while a statistically significant precipitation decrease pattern is dominant over the country with the SSP2-4.5 in the medium term. A similar pattern is present in the near term, where the decreasing pattern dominance shrinks with the SSP2-4.5.

The fall season is expected to experience countrywide and statistically significant precipitation decrease with the SSP2-4.5 (except the east) and SSP5-8.5 in the long term. However, the decrease is not significant over the country with the SSP2-4.5, except in some parts of the western and southern located regions, while the decrease

is statistically significant over the west, centre, northcentral, and northeastern Türkiye with the SSP5-8.5. In the near term, significant decreases are expected in the southcentral and northcentral Türkiye with the SSP5-8.5 and northcentral and northeastern Türkiye with the SSP5-8.5.

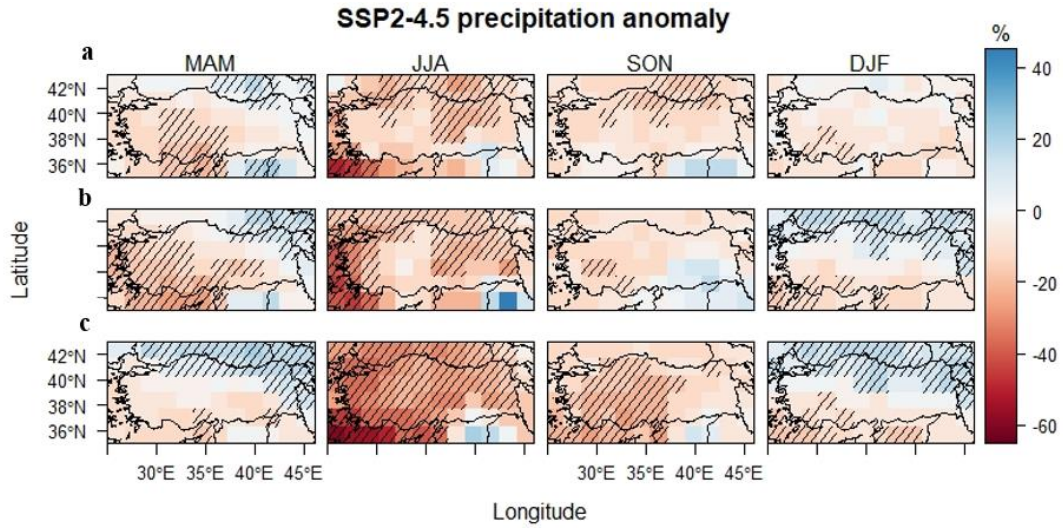


Figure 4.5. SSP2-4.5 precipitation anomaly a) in the near b) medium c) long terms. In the figure, statistically significant changes at the $p=0.05$ level are expressed with the hatched rasters (Bağçacı et al., 2021).

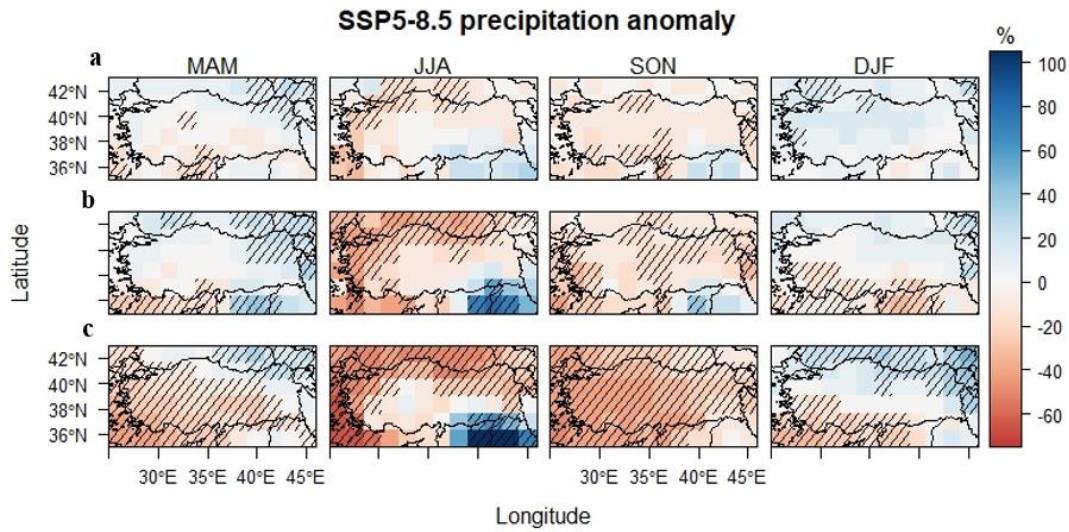


Figure 4.6. SSP5-8.5 precipitation anomaly a) in the short b) medium c) long terms. In the figure, statistically significant changes at the $p=0.05$ level are expressed with the hatched rasters (Bağçacı et al., 2021).

4.1.4.2 Near-surface temperature

The long-term near-surface temperature increase reaches a peak around $3.5\text{ }^{\circ}\text{C}$ with the SSP2-4.5 and $6.5\text{ }^{\circ}\text{C}$ with the SSP5-8.5 in the summer seasons with a relatively homogenous appearance over the Türkiye domain (Fig 4.7 c and Fig. 4.8 c). However, Türkiye's west show maximum warming with at least $0.5\text{ }^{\circ}\text{C}$ more increase, which also can be seen in the medium term (Fig 4.7 b and Fig. 4.8 b). The warming having an alike-pattern does not quantitatively diverge much between the two scenarios yet in the near term (Fig 4.7 a and Fig. 4.8 a).

The warming in the fall season has an increasing pattern along a diagonal corridor between northwest to southeast ($\sim 3\text{ }^{\circ}\text{C}$ and $\sim 5.5\text{ }^{\circ}\text{C}$ warming over the Southeastern Anatolia Region of Türkiye with the SSP2-4.5 and SSP5-8.5, respectively). Indeed, this increasing pattern is also present in the near and medium periods with diminishing values.

The spring season resembles fall, pointing out that the southeastern regions are exposed to maximum seasonal warming in the medium and long period with both scenarios. The near-term warming has a more homogenous pattern, while the fact remains that the southern regions are at least 0.5 °C warmer in this term. It should be noted that spring warming reaches up to 4 °C with the SSP5-8.5 over the Aegean and Mediterranean regions of Türkiye, which demonstrates the vulnerability degree of that regions when also considering the statistically significant precipitation decrease (up to 18%).

The winter warming utmost affects the east of the country, where near-surface temperature increases reach up to 2.5 °C (4.5 °C) with the SSP2-4.5 (SSP5-8.5) in the long term. These values are close to warming values in spring. These are important indicators for the watersheds in the Eastern Anatolia Region since the region is broadly under snow cover today's climate. The near and medium terms share a common picture with diminishing warming values; nevertheless, it may be sufficient to melt snow.

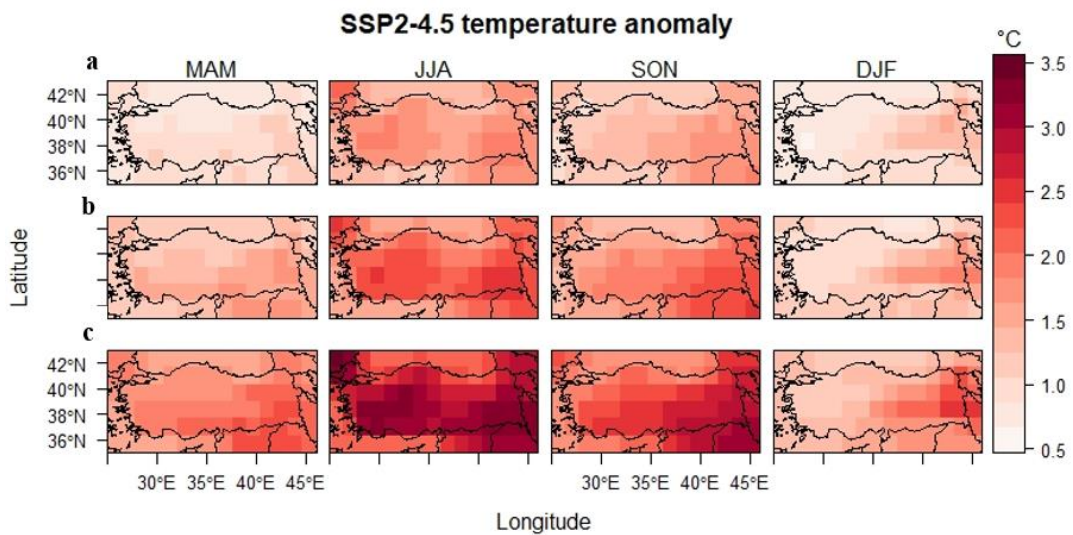


Figure 4.7. SSP2-4.5 near-surface temperature anomaly a) in the short b) medium c) long terms. All the near-surface temperature anomalies in the SSP2-4.5 and SSP5-8.5 are statistically significant at the $p=0.05$ level; thus, no hatching is drawn for the clarity (Bağçacı et al., 2021).

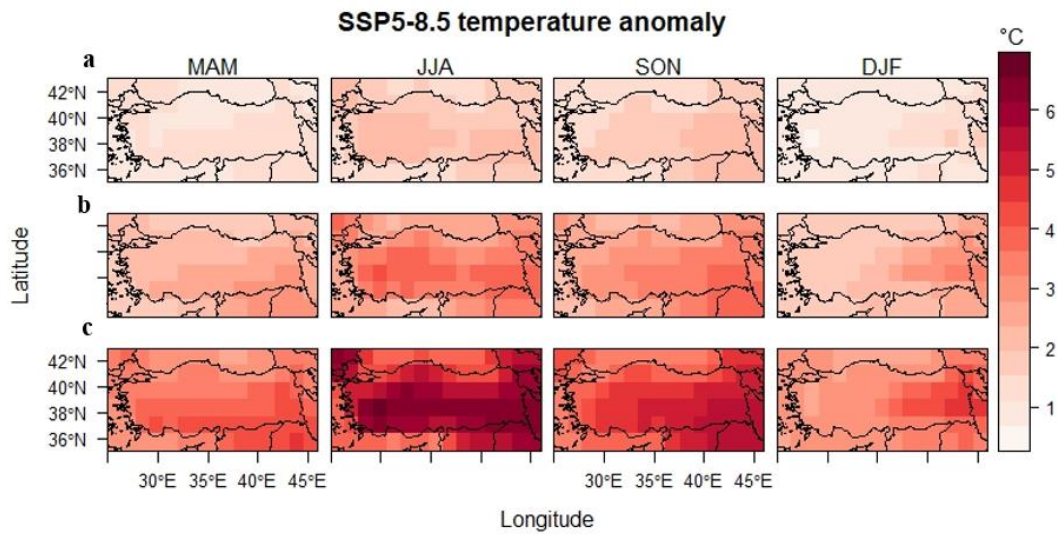


Figure 4.8. SSP5-8.5 near-surface temperature anomaly a) in the short b) medium c) long terms. All the near-surface temperature anomalies in the SSP2-4.5 and SSP5-8.5 are statistically significant at the $p=0.05$ level; thus, no hatching is drawn for the clarity (Bağçaci et al., 2021).

4.1.4.3 Assessment of the annual changes

We have employed the column charts to compare CMIP5 and CMIP6 MMEs' annual statistics under the worst scenarios both for near-surface temperature and precipitation (Fig. 4.9). For warming, standard deviations (sd) are same in the near term with 0.43 °C value, while in the medium term the difference is only 0.03 °C. However, the CMIP6 MME has a 0.73 °C sd value, and CMIP5 MME has a 0.61 °C sd value in the long term, showing that the CMIP6 MME has prone to more warming extremes. The near-term minimum temperature increase is 0.55 °C and 0.87 °C, and the maximum increase is 2.15 and 2.37 °C for CMIP5 and CMIP6, respectively, while the mean increase is the same with a 1.46 °C value. The mean and maximum increase is approximately 0.2 and 0.33 °C more with the CMIP6 (2.78 °C mean increase and 3.61 °C max increase for the CMIP6) than CMIP5 in the medium term, while the difference is not substantial in the minimum warming with a value of nearly 1.6 °C. The minimum and maximum warming values are around 3.15 °C and 5.48

°C, respectively, both for CMIP5 and CMIP6, while the mean increase with the CMIP6 MME (4.34 °C) is 0.1 °C more than CMIP5.

The sd of precipitation is higher with the CMIP6 than CMIP5 in the near and medium terms (CMIP6 MME precipitation sd is 7.8% and 6.6%, and CMIP5 MME precipitation sd is 7% and 5.8% in the near and medium terms, respectively). However, in the long term, CMIP6 MME precipitation sd is 5.8%, and this value is 7% for the CMIP5. It shows CMIP6 MME precipitation projections are more consistent than CMIP5 in the long period. The near-term mean precipitation decline is 2% with the CMIP6, while the maximum increase and maximum decline in precipitation are 14.4% and 16.1%, respectively. CMIP5 MME shows a less maximum increase (6.6%) but more mean decline (4.1%) and maximum decline (19.5%) in the same period. In the medium term, the picture does not change in terms of maximum increase and mean decline, i.e., CMIP6 shows these values of 6.7% and 4.5%, respectively, while CMIP5 shows these values of 5.3% and 7.9%, respectively. However, the maximum decline is ~2.5% more with the CMIP6 than CMIP5 in this term (20.4% for CMIP6 and 18% for CMIP5). The long term mean and maximum declines are close to each other (CMIP6 mean and maximum declines are 9.9% and 24%, respectively, and CMIP5 mean and maximum declines are 10.7% and 22.8%, respectively). However, CMIP6 MMEs' maximum precipitation increase is almost three and a half-fold that of CMIP5 (CMIP6's maximum increase is 8.8% and CMIP5's maximum increase is 2.4%).

These outcomes are coherent with the hypothesis put forth by Gettelman et al. (2019) and Monerie et al. (2020), in which larger anomalies in precipitation anomalies may result from a difference in the ECS between the CMIP6 and CMIP5 GCMs. Analogous to our findings, Almazroui et al. (2020) found an augmented warming characteristic between 1.0 °C and 2.5 °C from CMIP6 over Africa compared to CMIP5 GCMs and underlined that Africa is warming more rapidly than was previously thought. Even on an annual scale, extreme anomalies are more noticeable with the CMIP6 MME. Analogous to Africa, there is also warming acceleration confirmation in Türkiye with the CMIP6 outputs. A quite potent

precipitation rise (14.4%) in highest increase anomaly of the CMIP6 also coincides with this short period. Albeit the mean annual anomalies in the precipitation and the near-surface temperature obtained from CMIP5 and CMIP6 ensembles are not notably distinct, they turn into noteworthy at the regional and seasonal scales, especially for precipitation. However, maximum changes (decrease or increase) in precipitation anomaly are more remarkable for CMIP6, even at an annual scale (Bağçacı et al., 2021).

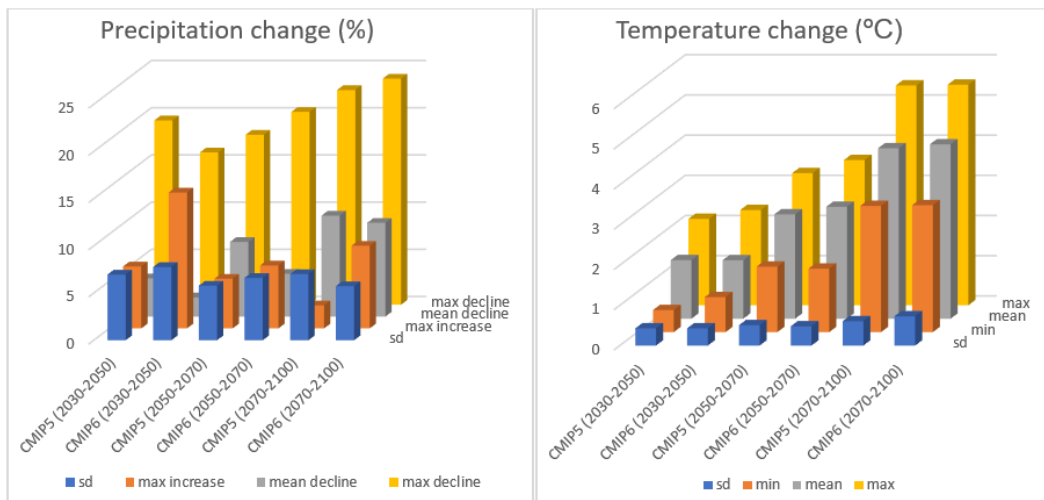


Figure 4.9. Comparison of the precipitation and near-surface temperature anomalies acquired from CMIP5 and CMIP6 under the highest-emission scenarios over Türkiye on an annual basis (Bağçacı et al., 2021).

We have compared correspondent GCMs in CMIP5 and CMIP6 under the highest emission scenarios to understand how precipitation and near-surface temperature projections change as data availability allows. Table 4.1 and Table 4.2 show these correspondent GCMs and their statistics over the Türkiye domain in the near, medium, and long terms. CMIP5 HadGEM projection shows an annual mean precipitation increase in the near and medium terms, while it is almost equal reference period mean in the long term. As for CMIP6 HadGEM projection, it shows no annual mean changes in the near term while showing a decrease in the medium term and a statistically significant potent decrease in the long term. The sd values of

CMIP5 HadGEM increase in the near term, then decrease in the medium term, and finally reach a state near the reference value in the long term. As for CMIP6, this value strongly increase in the near term while more strongly decrease in the medium period and then slightly decrease in the long period. It shows proportional precipitation decline is more robust and accelerated with CMIP6 HadGEM than its counterpart in CMIP5 in an annual scale. Similar situation exists in the CNRM GCMs. In summary, CMIP6 CNRM demonstrates around 3%, 6% and 15% more decline in the near, medium, and long periods, respectively, than its counterpart in CMIP5. However, in this case, CMIP5 CNRM shows a statistically significant annual precipitation decrease in the long term, and CMIP6 CNRM shows a statistically significant decrease in both the medium and long term. As for ACCESS GCM, only CMIP5 ACCESS shows a statistically significant mean decline of precipitation in the long term. There is only CMIP6 ACCESS that exhibits neither decreasing nor increasing tendency in all periods within the CMIP6 GCMs. However, its sd value strongly increase in the medium and long period, showing that extremes are more likely, while preserving mean values. On the other hand, both CMIP GFDL GCMs show a statistically significant precipitation decline in the medium and long periods on an annual scale. Both CMIP GFDL GCMs are more coherent in themselves and project incessantly decline in the annual precipitation (with acceleration; around 5%, 9% and 18% for CMIP5 GFDL, and around 6%, 13% and 17% for CMIP6 GFDL in the near, medium and long periods, respectively) over Türkiye (Bağçacı et al., 2021).

Table 4.1 Annual means and standard deviations of precipitation simulations of the best-performing available CMIP6 GCMs and their counterparts in the CMIP5 for Türkiye based on the RCP8.5 and SSP5-8.5. In the table, statistically significant anomalies at the $p=0.05$ level are expressed with bold characters (Bağçacı et al., 2021).

MODEL		HADGEM2-AO HADGEM-GC-31-MM		ACCESS-1 ACCESS CM-2		GFDL-CM3 GFDL-ESM4		CNRM-CM-5 CNRM-CM6-1-HR		AVERAGE	
Variable		Precipitation (mm)		Precipitation (mm)		Precipitation (mm)		Precipitation (mm)		Precipitation (mm)	
Dataset	Years	Mean	Sd	Mean	Sd	Mean	Sd	Mean	Sd	Mean	Sd
Reference	1986-2005	727.5	112.9	860.4	83.9	697.7	71.1	861.6	105.6	786.8	93.4
CMIP5	2030-2050	767.1	119.1	847.3	73.3	662.7	111.9	857.7	106.1	783.7	102.6
	2050-2070	758.0	101.5	844.0	89.6	637.3	93.8	839.4	86.8	769.7	92.9
	2070-2100	723.8	111.2	777.1	88.5	572.7	89.3	873.4	92.7	736.7	95.4
Reference	1995-2014	640.0	90.8	711.2	77.0	856.3	78.2	1032.8	100.1	810.1	86.5
CMIP6	2030-2050	642.4	129.3	710.2	74.8	809.0	106.8	998.0	108.5	789.9	104.8
	2050-2070	610.7	88.8	711.2	111.6	744.9	97.2	949.1	117.0	754.0	103.7
	2070-2100	560.5	82.1	709.0	100.6	713.9	87.0	887.8	114.7	717.8	96.1
$\Delta(\text{CMIP5} - \text{REF})$	2030-2050	39.6	6.3	-13.1	-10.5	-35.1	40.8	-3.8	0.5	-3.1	9.3
	2050-2070	30.5	-11.4	-16.4	5.7	-60.4	22.7	-22.2	-18.8	-17.1	-0.5
	2070-2100	-3.7	-1.7	-83.3	4.6	-125.0	18.2	11.8	-13.0	-50.1	2.1
$\Delta(\text{CMIP6} - \text{REF})$	2030-2050	2.4	38.5	-1.0	-2.2	-47.3	28.6	-34.9	8.4	-20.2	18.3
	2050-2070	-29.3	-2.0	0.0	34.7	-111.3	19.0	-83.7	16.9	-56.1	17.2
	2070-2100	-79.6	-8.7	-2.2	23.6	-142.4	8.8	-145.0	14.7	-92.3	9.6
$\Delta(\text{CMIP6} - \text{CMIP5})$	2030-2050	-37.2	32.2	12.1	8.3	-12.2	-12.3	-31.0	7.9	-17.1	9.06
	2050-2070	-59.8	9.4	16.5	28.9	-50.9	-3.6	-61.6	35.7	-39.0	17.61
	2070-2100	-75.8	-7.1	81.1	19.0	-17.4	-9.4	-156.8	27.7	-42.2	7.53

Among the CMIP6 GCMs, only CMIP6 MPI give a cooler projection than its counterpart in CMIP5, though not much ($0.1\text{ }^{\circ}\text{C}$), in the long term. Moreover, CMIP6 MPI is $0.4\text{ }^{\circ}\text{C}$ cooler than its counterpart in the near term, which is the maximum difference in coolness among CMIP6 GCMs, while no distinction exists in the medium term. Unlike CMIP6 MPI, CMIP6 MRI gives constantly warmer projections than its counterpart, showing the higher ECS on behalf of the Türkiye domain. The maximum difference in warmth is present with the CMIP6 CNRM with a value of

0.7 °C in the long term, while CMIP6 NorESM is warmer by only 0.2 °C than its counterpart in this period. Except for CMIP6 MPI, the remaining three have higher sd values in the long period than their counterparts in CMIP5, showing that heat extremes are more likely to occur. That is also specified in the preceding parts, where a higher maximum increase and decrease in anomalies are acquired from CMIP6 GCMs. Nonetheless, as indicated in the literature (Gettelman et al., 2019; Monerie et al., 2020), the improvements in the equations designating the model physics to have a remarkable influence on climate variability in near-surface temperature and especially precipitation by the end of this century over Türkiye, regarded as one of the climate hot spots (Bağçacı et al., 2021).

Table 4.2 Annual means and standard deviations of the near-surface temperature simulations of the best-performing available CMIP6 GCMs and their counterparts in CMIP5 for Türkiye based on the RCP8.5 and SSP5-8.5. All the near-surface temperature anomalies in CMIP5 and CMIP6 GCMs are statistically significant at the p=0.05 level (Bağçacı et al., 2021).

MODEL		MRI ESM1 MRI ESM2		MPI-ESM-MR MPI-ESM1-2- HR		CNRM-CM5 CNRM- ESM2-1		NOR-ESM1- M NOR- ESM2-MM		AVERAGE	
Variable		Temperature (C°)		Temperature (C°)		Temperature (C°)		Temperature (C°)		Temperature (C°)	
Dataset	Years	Mean	Sd	Mean	Sd	Mean	Sd	Mean	Sd	Mean	Sd
Reference	1986-2005	9.7	0.4	12.1	0.7	8.3	0.6	13.2	0.6	10.8	0.6
CMIP5	2030-2050	11.2	0.7	13.4	0.7	9.9	0.5	14.9	0.6	12.3	0.6
	2050-2070	12.0	0.5	14.7	0.8	11.3	0.8	16.1	0.6	13.5	0.7
	2070-2100	13.5	0.7	16.2	0.8	12.7	0.8	17.3	0.5	14.9	0.7
Reference	1995-2014	10.9	0.6	12.0	0.5	10.9	0.4	12.6	0.6	11.6	0.6
CMIP6	2030-2050	12.5	0.6	12.8	0.8	12.7	0.6	14.3	0.5	13.1	0.6
	2050-2070	13.9	0.7	14.6	0.8	13.7	0.7	15.6	0.6	14.4	0.7
	2070-2100	15.1	0.8	15.9	0.8	16.0	1.1	17.2	0.8	16.0	0.9
$\Delta(\text{CMIP5} - \text{REF})$	2030-2050	1.5	0.3	1.3	0.0	1.5	-0.1	1.7	0.0	1.5	0.0
	2050-2070	2.3	0.0	2.6	0.1	2.9	0.3	2.9	0.0	2.7	0.1
	2070-2100	3.8	0.3	4.0	0.1	4.4	0.2	4.1	0.0	4.1	0.1
$\Delta(\text{CMIP6} - \text{REF})$	2030-2050	1.6	0.0	0.8	0.3	1.8	0.2	1.7	-0.1	1.5	0.1
	2050-2070	3.0	0.2	2.6	0.2	2.8	0.2	2.9	0.0	2.8	0.2
	2070-2100	4.1	0.2	3.9	0.3	5.1	0.7	4.5	0.1	4.4	0.3
$\Delta(\text{CMIP6} - \text{CMIP5})$	2030-2050	0.1	-0.3	-0.4	0.3	0.2	0.2	0.0	-0.1	-0.04	0.04
	2050-2070	0.6	0.1	0.0	0.1	-0.2	0.0	0.0	-0.1	0.11	0.04
	2070-2100	0.3	-0.1	-0.1	0.2	0.7	0.5	0.4	0.2	0.32	0.20

4.2 Results of the sensitivity of the WRF physics parameterizations

Fig. 4.10 shows the daily mean precipitation statistics of the ground observations and 60 WRF configurations simulations. The mean and median values of the stations are 1.47 mm and 1.33 mm, respectively. The WRF simulations show a high-sensitivity range with mean values between 0.71 mm and 2.03 mm and median values between

0.61 mm and 1.92 mm across the configurations. The configuration numbers between 1 and 12 (except 2 and 6) show far less precipitation than the ground observations. On the other hand, Conf14, Conf18, Conf26, Conf30, Conf38, Conf42, Conf50, and Conf54 give far more precipitation values than the stations. The more reasonable successive configuration range is between Conf39 and Conf49. Conf2, Conf20, Conf27, Conf43, and Conf55 fit better to the stations in terms of box sizes, mean, and median values. However, none of these takes place in the top five performing configurations in terms of correlations. It may be due to the extreme dominance in the correlation calculations. Here the best performing configuration is composed of the new Thompson microphysics scheme (Thompson et al., 2008), the Yonsei University (YSU) planetary boundary layer scheme (Hong et al., 2006), and the Tiedtke cumulus parameterization scheme (Tiedtke, 1989; Zhang et al., 2011).

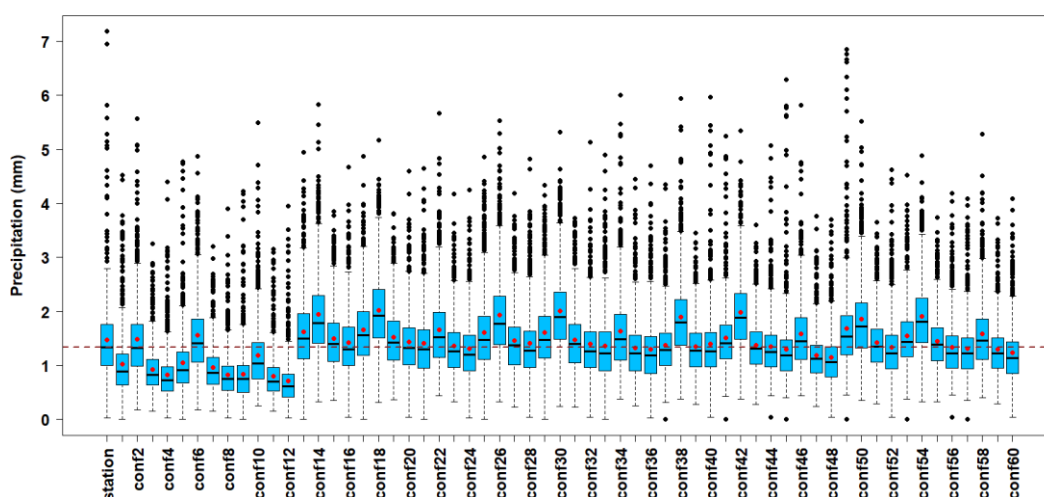


Figure 4.10. The daily mean precipitation statistics of the ground observations and 60 WRF configurations. The first box denotes station statistics. The dashed line belongs to the median value of the stations. The mean values of the boxes are shown with red points, and the median values are shown with the black lines in the boxes.

Fig. 4.11 shows the daily precipitation correlation and RMSE statistics of the configurations with the ground observations. The correlation values are between 0.51 and 0.65. Five configurations form the lower tail outliers giving correlation

values lower than 0.55. The mean and median values are close to each other, around 0.61. On the other hand, the RMSE values are between 4- and 5 mm, and the mean and median values are 4.37- and 4.25 mm, respectively.

The resultant best-performing configuration remarked above was utilized in the long-term PGW runs in the next section. The retrospective simulations between 1995-2014 have shown performance improvement in terms of correlations, except in 1999 and 2014. As for RMSE, it has a similar range to the sensitivity studies conducted here. Please see the next section for further information.

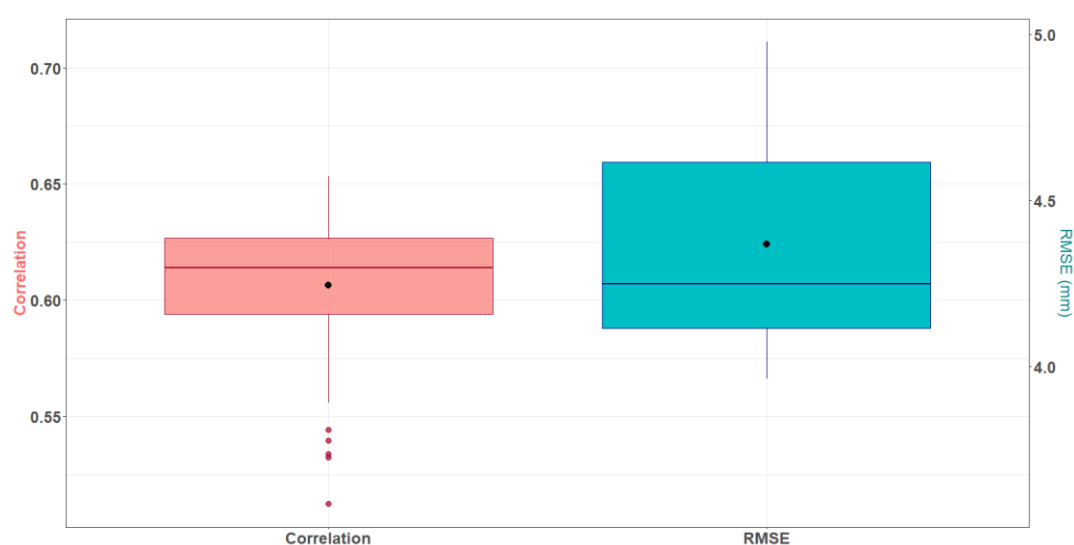


Figure 4.11. The WRF simulations configurations-wide precipitation statistics. The daily precipitation correlations (the left axis with the light pink box) and RMSEs (the right axis with the turquoise box). The black points denote the mean values of the correlations and RMSE.

4.3 Results of the PGW-based dynamic downscaling

4.3.1 Validation

The monthly precipitation correlation between E-OBS and the WRF simulations varies from 0.60 to 0.76, which is the worst series between the gridded datasets for

the 1995-2014 period (Fig. 4.12 a). Similarly, the monthly RMSE values of the E-OBS are in the range of 34-52 mm which is higher than the others. The GPCC and GPCC-HOAPS are in close agreement with each other for correlation and RMSE values, according to the WRF. The monthly correlation of the GPCC-HOAPS varies between 0.70 and 0.79, and the GPCC correlation is only one percent lower than the min-max values of the HOAPS. Similarly, the monthly RMSE values of GPCC-HOAPS are in the range of 29.8 and 39.2 mm, which is 3 mm lower than those of GPCC. The WRF simulations give the best performance with the ground observations of Türkiye for monthly correlation values. The minimum correlation between WRF and stations is 0.74, while the maximum is 0.86. The RMSE values of the stations vary between 29.1 and 39.7 mm, which closely resembles the GPCC and GPCC-HOAPS.

The daily precipitation statistics between WRF simulations and the ground observations of Türkiye were also obtained for the 1995-2014 period (Fig. 4.12 b). The daily correlation values vary between 0.60 and 0.75, and the RMSE values are in the range of 3.8- and 5.4-mm. Owing to the dense network of ground measurements, here we also highlight the spatial correlation between WRF simulations and stations (Fig 4.12 c and d). Fig. 4.12 c shows spatial distributions of the daily correlations between the stations and the WRF simulations in the 1995-2014 period. The daily correlations are no lower than 0.5 and give higher values (up to 0.83) over southeastern Türkiye. The correlation values vary between 0.5-0.6 over the easternmost Mediterranean coasts and northeastern Türkiye and in the range of 0.6-0.7 over the Aegean coasts and northwestern country. Apart from these, the spatial correlations generally have a homogeneous appearance. The wet season (NDJFM) daily correlations are in better agreement between the WRF simulations and stations than the multiyear daily correlations (Fig. 4.12 d). The daily correlations are in the range of 0.7-0.9 in most of the country, while the Aegean coasts and some parts of the Mediterranean coasts have correlations in the band of 0.6-0.7. Besides these, there is no consistent spatial pattern in the wet season daily correlations.

The near-surface temperature statistics are far better agreement between gridded and ground observations and WRF simulations than those in precipitation (Fig. 4.13). The 20-year-long daily near-surface temperature correlations are 0.97 and 0.98 between WRF-EOBS and WRF-ground observations, respectively. The daily RMSE value in the same period is 1.78 °C for WRF-ground and 2.53 °C for WRF-EOBS. The monthly near-surface temperature correlation between WRF and CRU is 0.97, while it is 0.99 between WRF and ground observations. The RMSE values are 2.37 and 1.48 °C between WRF-CRU and WRF-ground observations, respectively.

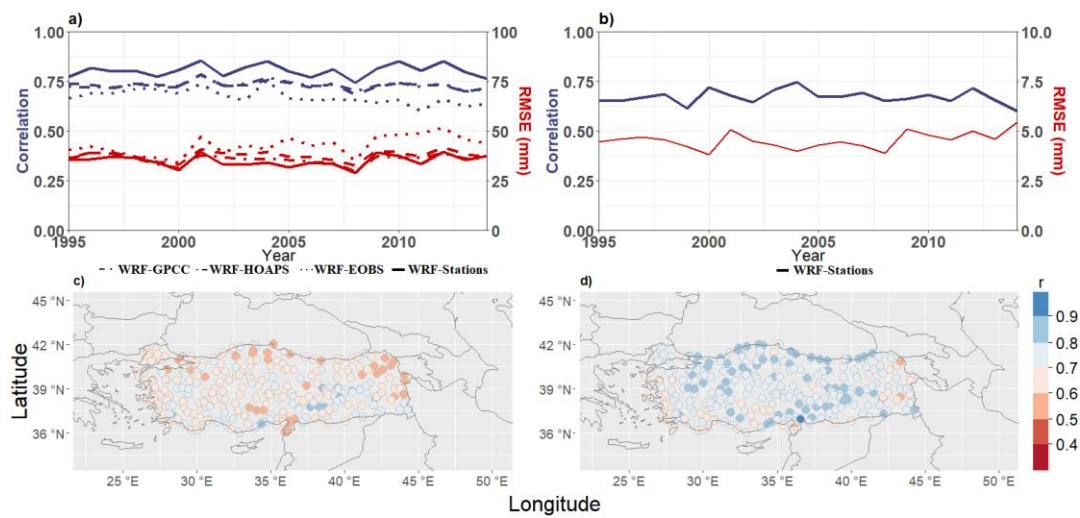


Figure 4.12. The WRF simulations precipitation statistics: a) The monthly precipitation correlation (the left axis with the blue lines) and RMSE (the right axis with the red lines). The solid line denotes the WRF-ground observation statistics, dashed line denotes the WRF-GPCC statistics, dot dashed line denotes WRF-GPCC HOAPS statistics, and dotted line denotes WRF-EOBS statistics. b) As in a, but for daily precipitation statistics between WRF and ground observations. c) The spatial daily precipitation correlations between WRF and ground observations for 1995-2014 in Türkiye domain. d) As in c, but for the wet season (NDJFM).

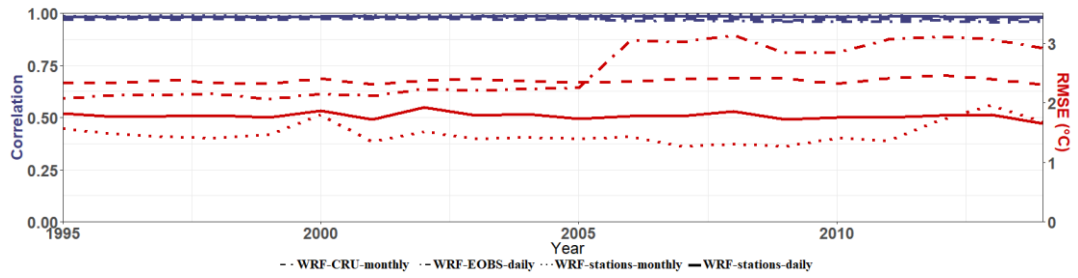


Figure 4.13. The WRF simulations near-surface temperature statistics: The daily and monthly correlation (the left axis with the blue lines) and the daily and monthly RMSE (the right axis with the red lines). The solid line denotes the daily WRF-ground observation statistics, dashed line denotes the monthly WRF-CRU statistics, dot dashed line denotes the daily WRF-EOBS statistics, and dotted line denotes the monthly WRF-ground observation statistics.

4.3.2 Seasonal precipitation change

In a coarser resolution, the GCM ensemble shows a substantial precipitation decrease of up to 100 mm over the Mediterranean and Aegean coasts of the EMBS in winter; such drying reaches into the inner Anatolian Peninsula in the north and Cyprus, Crete, and Syrian Mediterranean coasts in the south, with a gradual decline down to 35-40 mm (Fig. 4.14). The similar pattern can be observed over the north of the Fertile Crescent and with decreasing amounts around 15 mm. On the other hand, the same ensemble expects an increase in precipitation up to 80 mm over the southeast coasts of the Black Sea and southwest coasts of the Caspian Sea. The precipitation increase is around 25-35 mm over the inner domains between these regions, including Caucasus and the northeastern Anatolia. The decreases/increases are statistically significant at a 95% confidence interval. In a higher resolution simulation, the WRF model captures the pattern at a reasonable level, however, with enhanced magnitudes (Fig. 4.15). Here, with the WRF model, the decrease in winter precipitation over the Mediterranean coasts and following inner highlands of Türkiye, which takes most of the annual precipitation through the instrumentality of

its orography, is almost two and half fold that of the GCM ensemble. Such enhanced drying is also present over the pattern-like regions mentioned above. The regions with increased precipitation also cohere except the Russian Black Sea coasts. Here, the precipitation decrease is up to 100 mm. On the other hand, the WRF simulations show a precipitation increase between 100 and 200 mm over Türkiye’s northeastern Black Sea coasts which, is enhanced magnitude than that of the GCM ensemble.

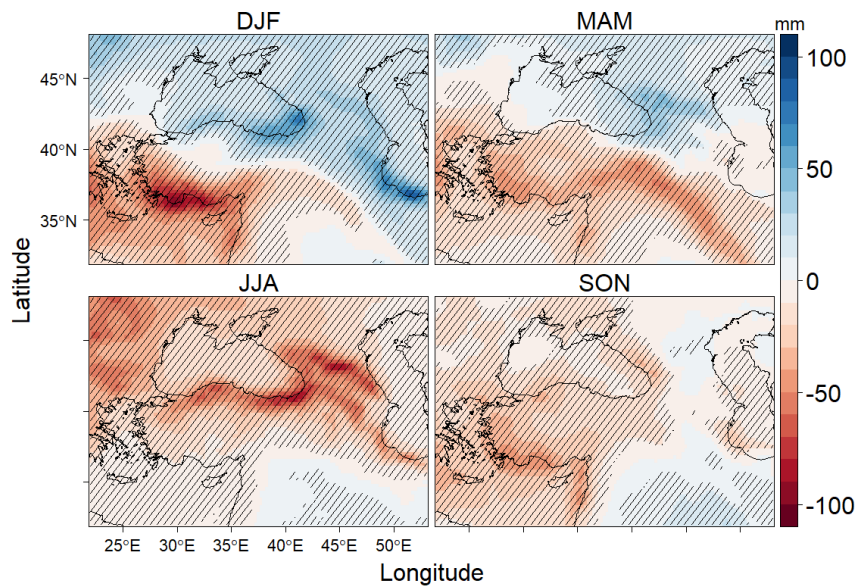


Figure 4.14. The seasonal precipitation change (in the units of mm) between 2071-2100 (future SSP5-8.5 scenario) and 1985-2014 (historical) retrieved from 13 CMIP6 GCM model ensemble. The statistically significant changes at $p \leq 0.05$ level are hatched.

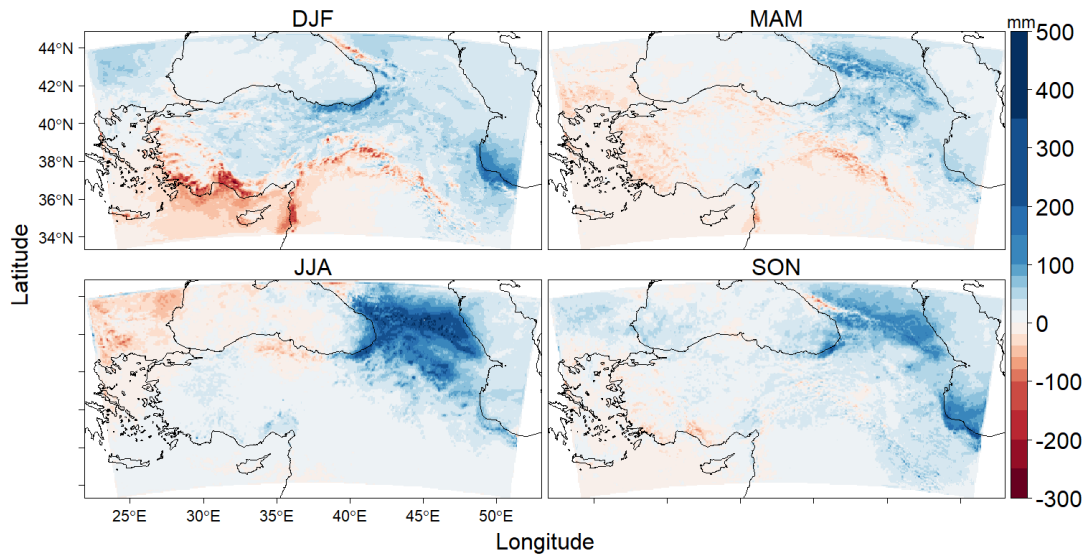


Figure 4.15. The seasonal precipitation change between 1995-2014 and the corresponding pseudo future period in the units of mm obtained from the WRF simulations for the EMBS domain.

The spring season precipitation pattern resembles that in the winter over the southern EMBS, where the precipitation decline amount is mostly less but more widespread. The decline falls by half over Cyprus, Crete and the Mediterranean coasts of Türkiye and Syria and triples over the northern branch of the Fertile Crescent with the GCM ensemble. The WRF simulations yield a sharper decline in the decrease in all those regions and show an increase up to 85 mm over a tiny part of the northwesternmost of the Fertile Crescent. Over the Caucasus and northeastern Anatolia, the precipitation increase resembles; however, with the WRF model, the increase penetrates more south along the mountainous region of Anatolia. The precipitation increase is roughly between 100 and 170 mm with the WRF simulations over the Caucasus, which is four times that of the GCM ensemble. It should be noted that, we observed a reverse sign, i.e., an increase with the WRF model and a decrease with the GCM ensemble, which is statistically significant at $p \leq 0.05$ level in an interrupted area over the southwest coasts of the Caspian Sea.

In summer, the picture becomes more different. The southeastern coasts of the Black Sea and the northwest coast of the Caspian Sea, together with the Caucasus and the

surrounding highlands, experience a high precipitation increase with the WRF simulations (mostly between 100mm and 350 mm, and up to 500 mm for the marginal points), while GCMs expect a high statistically significant decrease up to 90 mm. The southern part of the EMBS and most of the Anatolian plateau, which takes far less precipitation in summer than the other seasons, also shows different signs among the GCM ensemble and WRF simulations, though not as much over the Caucasus and nearby regions. The GCM ensemble shows a decrease up to 20 mm in statistically significant regions at $p \leq 0.05$ level, while the WRF simulations show an increase mostly up to 20 mm (for the marginal points, this amount rises to 100 mm) over the region. It should be noted that precipitation increase does not exceed 2 mm over most of the Syrian and Iraq territory with the GCM ensemble and WRF simulations. When looking at the remaining regions, the picture is more compatible. The GCM ensemble and the WRF model agree on the prominent drying and its amount when excluding marginal points over the northwestern part of the EMBS and the Black Sea coasts of the east of northernmost Anatolia.

The GCM ensemble demonstrates no statistically significant precipitation changes at $p \leq 0.05$ level over the eastern Caucasus and its south, while the WRF simulations amplify precipitation over the same region in the fall season. The precipitation increase exceeds 100 mm over the Caucasus and nearby regions and exceeds 200 mm over Türkiye's eastern Black Sea coast and southwest Caspian Sea coasts with the WRF simulations. The increase also penetrates towards the south and west with diminishing values. However, precipitation decline shares a common picture between the GCM ensemble and the WRF model towards the northwestern part of the Caucasus and the Russian Black Sea coasts. On the other hand, the GCM ensemble shows a statistically significant precipitation decline of around 10 mm over Bulgaria. The WRF simulations show an increase roughly between 10 and 60 mm over the country. The drying and its amount in the southwestern Anatolian plateau, the Mediterranean and Aegean coasts of Türkiye, northern Greece, Greek islands, and Cyprus are in good agreement between the GCM ensemble and the WRF model.

4.3.3 “Dynamic” and “thermodynamical” factors

The CMIP6 GCMs, as their predecessors, show an “anomalous” ridge formation over southern Italy in winter, taking effect over the whole Mediterranean (Fig. 4.16). It moves northwest and approaches the high-pressure system over the North Atlantic in the vicinity of its French and British coasts in spring. The surface anticyclone loses its strength but still governs the low-level circulation over the EMBS. In the summer season, dipole-like SLP pattern formation stands out between the north of the Bay of Bengal and the Eastern Mediterranean. It results in a cyclonic low-level circulation development over the EMBS. In the fall season, the low-pressure system largely diminishes over the Eastern Mediterranean; however, it still exists over the North Africa and Arabian Peninsula in the south and southern EMBS in the north. Another low-pressure system, which seems having an effect on the circulation over the northern EMBS, is located in the eastern Caspian Sea. It also has a diminished appearance compared to summer. Overall, the spring season follows winter, and fall season follows summer over most of the EMBS in terms of circulation pattern.

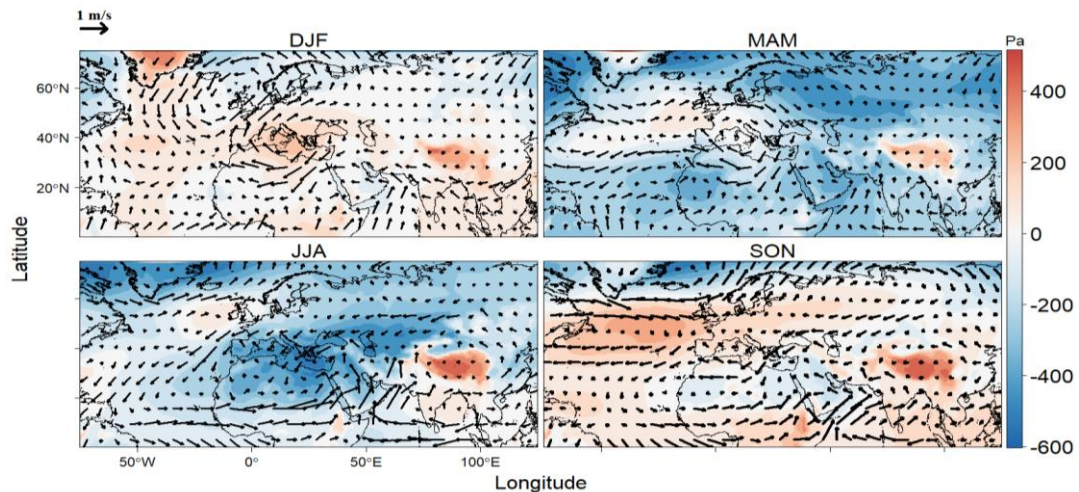


Figure 4.16. The large-scale low-level (850 hPa) circulation (winds as vectors) and SLP (shadings) change signal of the PGW forcing between 2071-2100 (future SSP5-8.5 scenario) and 1985-2014 (historical) retrieved from 13 CMIP6 GCM model ensemble. The wind vectors are in the units of m/s and sea-level pressure is in the units of pascal. The reference vector is presented in the upper left.

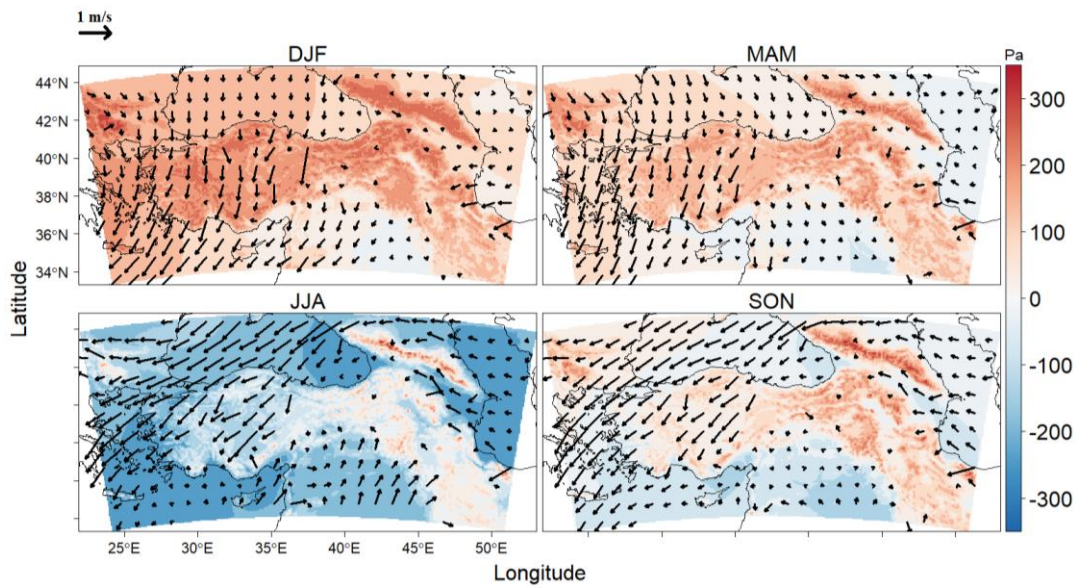


Figure 4.17. The low-level (850 hPa) circulation (winds as vectors) and SLP (shadings) change between 1995-2014 and the corresponding pseudo future period for each season obtained from the WRF simulations for the EMBS domain. The wind vectors are in the units of m/s and sea-level pressure is in the units of pascal. The reference vector is presented in the upper left.

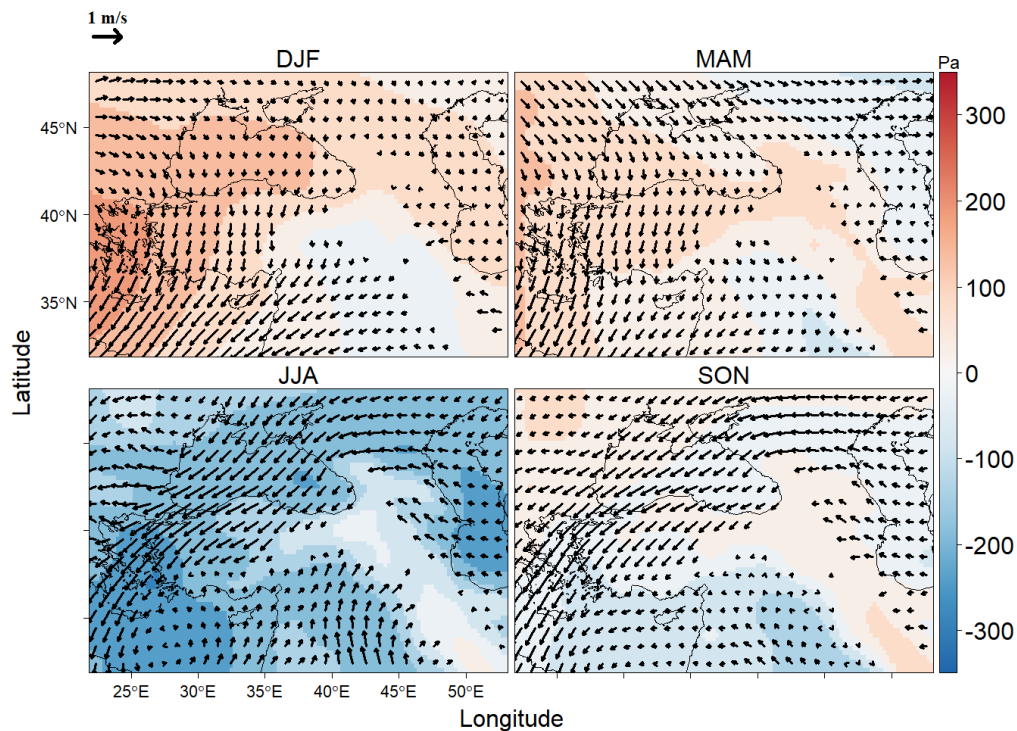


Figure 4.18. The low-level (850 hPa) circulation (winds as vectors) and SLP (shadings) change signal of the PGW forcing between 2071-2100 (future SSP5-8.5 scenario) and 1985-2014 (historical) retrieved from 13 CMIP6 GCM model ensemble for the extended EMBS domain. The wind vectors are in the units of m/s and sea-level pressure is in the units of pascal. The reference vector is presented in the upper left.

Fig. 4.17 shows that the anomalous ridge strengthens the low-level anticyclonic circulation in winter over most of the EMBS region, from the westernmost to the vertical line between the northwestern Caucasus and the Syria-Iraq border in the east. It is consistent with the GCM ensemble simulations, which show anticyclonic response but with less strengthened wind patterns (Fig. 4.18). The wind flow is northwesterly and northerly in the north and northwestern EMBS, which is known to advect dry and cold air in today's climate. The advected air becomes slightly moister for the future period with a relatively small increase in specific humidity between 1-1.5 g/kg in the near-surface and around 1 g/kg in the lower troposphere (Fig. 4.19 and Fig. 4.20). These factors are expected to increase precipitation over

northern Bulgaria and the Black Sea Region of Türkiye by orographic enhancement since the moistened wind patterns are perpendicular to the mountain range. It is the case by a majority; however, the expected picture does not hold over some parts of the southwestern Black Sea Region coasts with the WRF simulations. Here, the precipitation decrease seems related to the mid-tropospheric subsidence (Fig. 4.21). To the south of the EMBS, precipitation dramatically decreases, consistent with the subsidence over almost all levels of the troposphere. The decrease is also prominent towards the inner Anatolian Plateau from the west and the Mediterranean coast, which is coherent with GCM ensemble simulations (Fig. 4.14 and Fig. 4.15). However, the plateau does not react homogeneously in terms of precipitation change as in the ensemble, which is also the case for the vertical pressure velocity showing air ascending/descending. The WRF simulations indicate precipitation decrease over southeast Anatolia and its extension towards Syria and northern Iraq as a result of more strengthened mid-level tropospheric subsidence and high dew-point depression. It shows that the “forced down” effect of the northerlies is limited along a belt, crossing mountain ranges over the southern EMBS. A similar phenomenon as in the northern EMBS may explain the increase in precipitation over the southwest coasts of the Caspian Sea. Here, the wind patterns are easterly and perpendicular to the mountain range resulting in an escalated upward movement of the moist air parcel. Besides, here is one of the rare regions with the Caucasus where the dew-point depression decreases (Fig. 4.22). It may also explain the increased precipitation over the Caucasus except for its northwest margin. Here, the dew-point depression and mid-tropospheric subsidence increase, which seems responsible for precipitation suppression. As for warming, the eastern Anatolian Plateau shows maxima at 8.8 °C, which is more about 2.4 °C than in the GCM ensemble (Fig. 4.22 and Fig. 4.23). The same region broadly loses its snow cover area in winter (not shown). The warming in the remaining regions is not less than 2.2 °C. The land warming is up to 2 °C more than the sea over Türkiye’s Mediterranean and the Black Sea coasts.

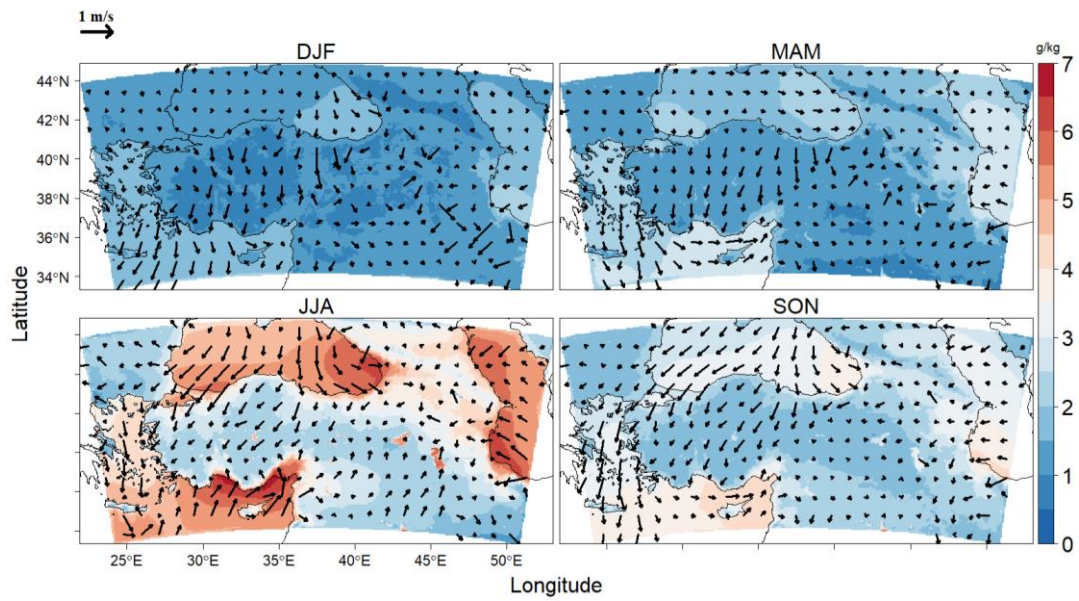


Figure 4.19. The near-surface (at 10-meter for the winds and 2-meter for the specific humidity) wind pattern (vectors) and specific humidity (shadings) change between 1995-2014 and the corresponding pseudo future period for each season obtained from the WRF simulations for the EMBS domain. The wind vectors are in the units of m/s and specific humidity in the units of g/kg. The reference vector is presented in the upper left.

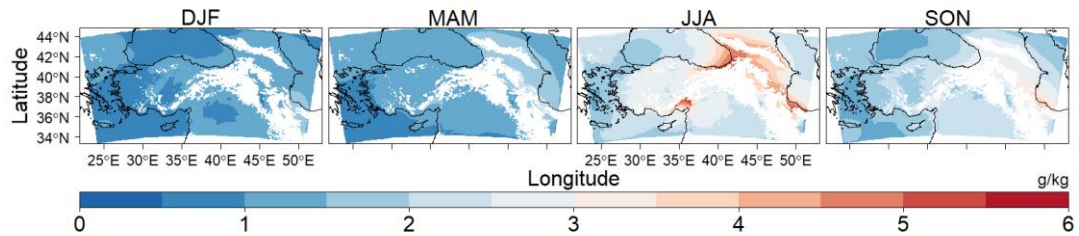


Figure 4.20. The low-level (850 hPa) specific humidity change between 1995-2014 and the corresponding pseudo future period in the units of g/kg for each season obtained from the WRF simulations for the EMBS domain.

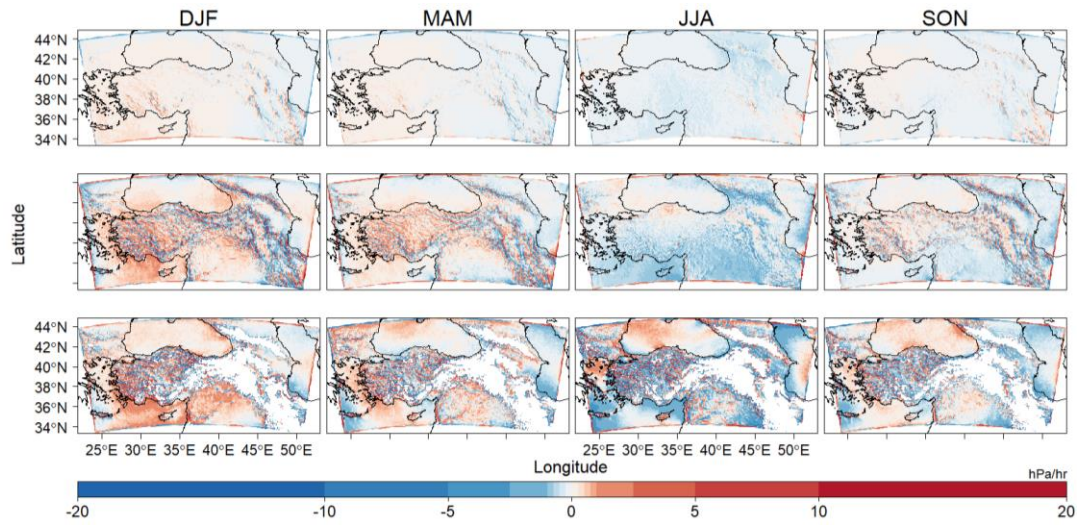


Figure 4.21. The vertical pressure velocity (ω) change between 1995-2014 and the corresponding pseudo future period in the units of hPa/hr for each season obtained from the WRF simulations for the EMBS domain. The ω changes are presented in 200 hPa (in the top), 500 hPa (in the middle), and 850 hPa (in the bottom) pressure levels.

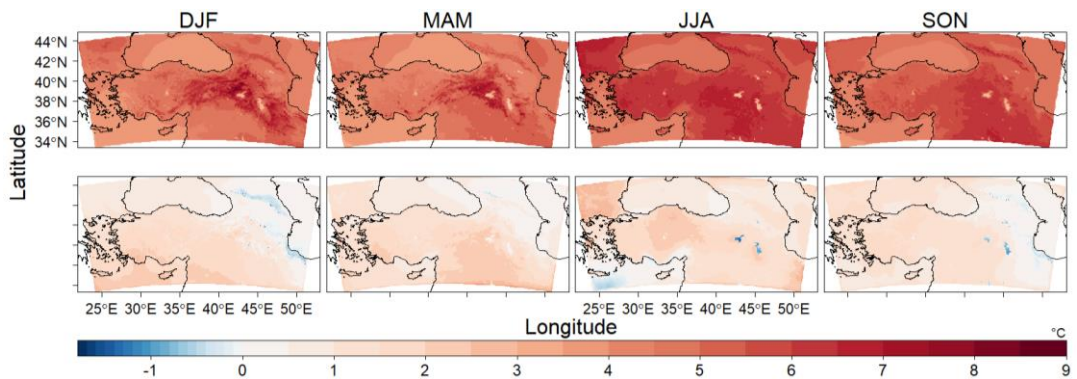


Figure 4.22. The near-surface temperature (at the top) and dew-point depression (at the bottom) change between 1995-2014 and the corresponding pseudo future period in the units of $^{\circ}\text{C}$ for each season obtained from the WRF simulations for the EMBS domain. The dew-point depression was averaged with the values between the near-surface and 700 hPa pressure level.

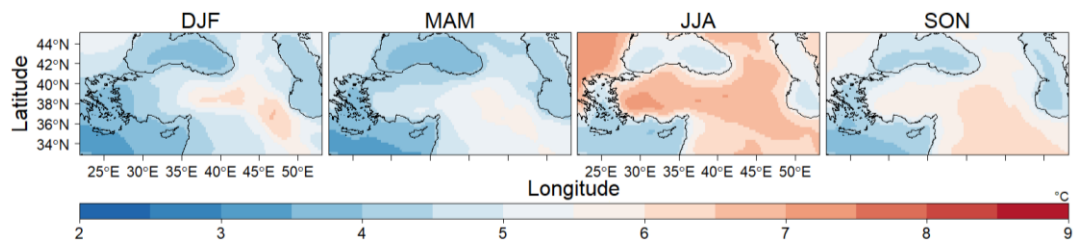


Figure 4.23. The near-surface temperature change signal of the PGW forcing between 2071-2100 (future SSP5-8.5 scenario) and 1985-2014 (historical) retrieved from 13 CMIP6 GCM model ensemble for the extended EMBS domain in the units of °C.

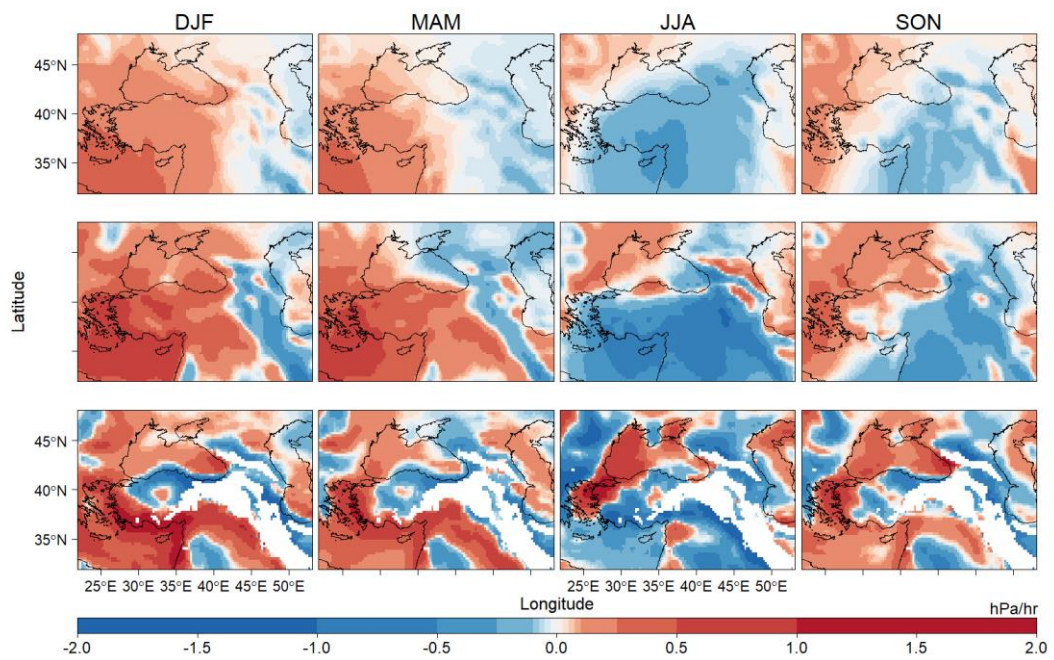


Figure 4.24. The vertical pressure velocity (ω) change signal between 2071-2100 (future SSP5-8.5 scenario) and 1985-2014 (historical) retrieved from 13 CMIP6 GCM model ensemble for the extended EMBS domain in the units of hPa/hr. It should be noted that legend is one-tenth of the WRF simulations.

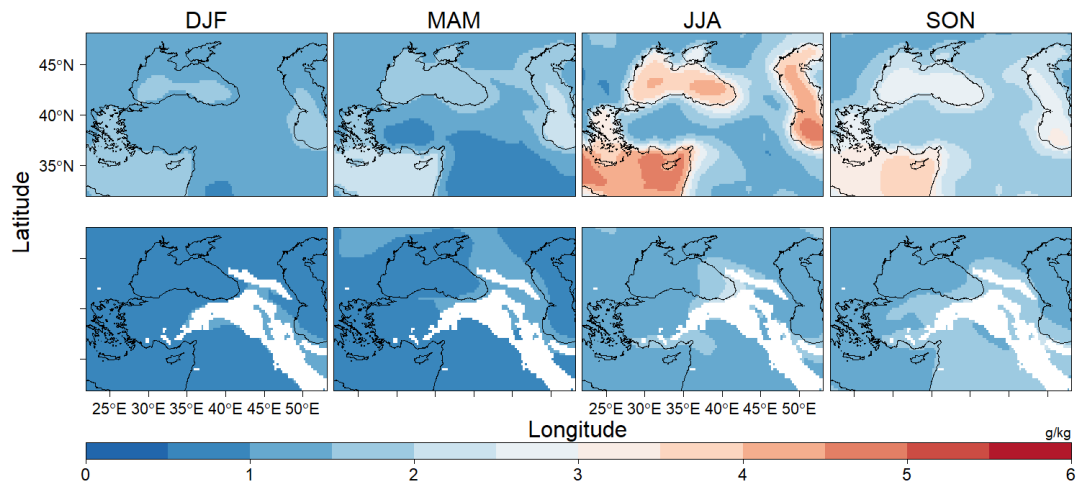


Figure 4.25. The specific humidity change signal of the PGW forcing between 2071-2100 (future SSP5-8.5 scenario) and 1985-2014 (historical) retrieved from 13 CMIP6 GCM model ensemble for the extended EMBS domain in the units of g/kg. The first row shows the near-surface (at 2m) changes, and the second row shows the low-level (at 850 hPa) changes.

Spring season shows a similar low-level circulation pattern as in the winter but with a moister atmosphere (Fig. 4.17, 4.19, 4.20). Precipitation decrease has a similar pattern but is less intense over the southern and southwestern EMBS (Fig. 4.15). It should be noted that the seasonality and regional precipitation differences are typical over most of the EMBS. Therefore, the amount of decrease should not be misleading in the comparison. The precipitation decline over Bulgaria seems related to the substantial low-level subsidence and increased dew-point depression since prevailing wind patterns, which trigger winter rainfall over the northern country, strengthen without changing direction (Fig. 4.17, 4.21, 4.22). Although the anomalous ridge softens the blow, it still manifests itself over the diagonal corridor between the Aegean Sea and the Mediterranean Sea by almost all level subsidence (Fig. 4.16, 4.17, 4.21). It mostly explains precipitation decrease over the regions that fall into the corridor. However, outside the corridor (the western side), Crete Island also experiences a precipitation decrease. The island is in the region where the surface anticyclone strengthens, which may suppress precipitation. Besides, through

the deeper troposphere, dew-point depression increases, making the air drier. Over the eastern side of the corridor, pointing to the easternmost Mediterranean coasts and inner Taurus mountains, the moist air parcel with upward motions (negative omega) causes to increase in precipitation under unchanged wind patterns. The northeast of the EMBS exhibits a pretty different picture. Here, the precipitation increase is dramatic, especially over the Caucasus. The wind patterns are westerly over the north and easterly over the south of the Caspian Sea in line with the sea-level pressure change. The mid and upper tropospheric negative vertical pressure velocity promotes the moist air to ascend along the high-altitude regions located in the eastern EMBS. The orographic enhancement of precipitation is the case over the southwest coast of the Caspian Sea and inland, where the wind blows perpendicularly. Similar to the winter season, near-surface warming shows its seasonal maxima over the eastern Anatolian Plateau and the high-altitude regions of the Taurus mountains with 8 °C, which is more about 2.3 °C than in the GCM ensemble (Fig. 4.22 and Fig. 4.23).

The summer season exhibits the remote effect of the heat low formed over the inland Arabian Peninsula on the EMBS, as asserted by Barcikowska et al. (2019). They showed that the intensification of the Persian trough accompanies the low, characterized by ascending air and convergent flow. They also stated that this effect tends to weaken subsidence over the EMBS and enhance subsidence over the central Mediterranean. It amplifies sea-level pressure dipole differences resulting in strengthened Etesian winds. Here we confirm the authors about the strengthened Persian trough and convergent flow into it (Fig. 4.16, 4.17, 4.21 and Fig. 4.24). We also confirm the tendency to the heat low formation over the eastern Mediterranean, albeit it locates more western than the authors indicated. However, we did not observe a sea-level pressure increase in the boundary over the central Mediterranean. It results in the deflection of the 850 hPa wind patterns from a northerly to a northeasterly direction along the Aegean Sea, albeit Etesians strengthens by conserving its direction at near surface level (Fig. 4.19). A similar opposite sign of sea-level pressure exists over the Black Sea. Here, we observed negative SLP change over the Black Sea, where the low-level wind blows from the Caspian Sea to that

sea, consistent between the GCM ensemble and the WRF (Fig. 4.17 and Fig. 4.18). The weakening of the subsidence over the eastern Mediterranean manifests itself in the southern EMBS, including most of the Anatolian Plateau. Precipitation slightly increases over those regions. It should be noted that the mentioned regions show strong seasonality; hence a slight increase constitutes a high percentage. On the other hand, the land-sea temperature contrast increases with the WRF simulations (Fig. 4.22), i.e., the land warms faster than the sea, which may suppress precipitation in the coastal regions of the southern EMBS (Barcikowska et al., 2019). The low and mid-tropospheric subsidence are accompanied by a precipitation decrease over the northwestern EMBS. The convergent flow does not translate to a substantial precipitation increase over the southern Persian trough. A large discrepancy in summer precipitation is present over the northeastern EMBS centring the Caucasus between the GCM ensemble and the WRF simulations. The WRF simulation shows an anomalous precipitation increase, while the GCM ensemble shows a substantial decrease. In fact, the low-level (850 hPa) circulation change draws a similar picture over the region. Besides, the low and upper-tropospheric (200 hPa) pressure movements have a similar pattern (Fig. 4.21 and Fig. 4.24). However, the vertical pressure velocity has an opposite sign in the mid-troposphere. The WRF simulation exhibits a strong air ascent, while the GCM ensemble shows a descent over the Caucasus in the mid-troposphere. Moreover, the WRF simulations show a more specific humidity increase in near-surface and lower troposphere than the GCM ensemble with an extended area (Fig. 4.19, 4.20 and Fig 4.25). The following section investigates this discrepancy with an additional analysis. The near-surface temperature increase has a more homogenous appearance, where the GCM ensemble shows its seasonal maxima over northwestern EMBS with around 7.3 °C and around 7.2 °C over western Anatolia (Fig. 4.23). The WRF simulations agree for northwestern EMBS in terms of warming amount and expect 0.5 °C less warming for western Anatolia. However, it shows warming maxima over the high altitudes of the Caucasus with values exceeding 7.3 °C (Fig. 4.22).

The fall season demonstrates similar low-level circulation and precipitation patterns as in summer over most of the EMBS (Fig. 4.15 and Fig. 4.17). The most pronounced difference in precipitation change exists in the northwestern domain. Here, the subsidence slightly decreases, and air ascent slightly increases over the mid-troposphere (Fig. 4.21). The wind patterns also slightly tilt, from easterly to northeasterly, making it more perpendicular to the mountain range in Bulgaria. The heat low effect diminishes or even disappears over the western side of the EMBS, including the Aegean Mediterranean coasts and inland Anatolian Peninsula (Fig. 4.17 and Fig. 4.21). The region experience a slight precipitation decrease. There is no substantial low-level wind pattern change over Syria and Iraq, where low-level subsidence and mid-level air ascent are present. Precipitation does not change substantially over the region until the eastern located-mountain range. To the east of the EMBS, where precipitation increase is less but more widespread, the dew-point depression increases less than those in summer (Fig. 4.22). Also, the depression slightly decreases over the northern Caucasus and southern Caspian coasts. These seem responsible for more westward propagated precipitation patterns since near-surface and low-level specific humidity increases are less than in summer. Compared to the summer season, a less intense but still strong precipitation increase signal exists over the Caucasus and Türkiye's eastern Black Sea coast. It seems related to the attenuation of the mid and upper-tropospheric ascent since the circulation pattern is nearly unchanged over the region. The near-surface warming has a similar pattern between the GCM ensemble and the WRF simulation showing that the southeastern EMBS is generally warmer than the other regions with values between 6 and 6.5 °C. However, the WRF simulations also show that the high altitudes of the Caucasus are also one of the most warming places where its marginal points show warming exceeding 6.5 °C. Here, we turn the section by focusing on the anomalous precipitation increase over the Caucasus and nearby regions with an additional analysis, which investigates its future climatic characteristics in more detail.

4.3.4 Additional simulation

We want to emphasize the SST availability of the GCM ensemble members to explain the most likely reason behind the anomalous precipitation increase over the Caucasus and nearby regions, especially in summer. Table 4.3 shows this availability for the Black Sea, the Mediterranean Sea, and the Caspian Sea. Accordingly, in the SST perturbation, we could only utilize SST information from 3 out of 13 GCMs (CMCC-CM2-SR5, CMCC-ESM2, and HadGEM3-GC31-MM) for the Caspian Sea (Table 4.3). It should be noted that, unlike the Caspian Sea, SST datasets are available for 11 GCMs (the remaining two GCMs could not be used for any seas due to not being able to be downloaded appropriately and no regular grid system) over the Black Sea and the Mediterranean Sea. It yields more warming in the Caspian Sea if one considers the long-term seasonal changes of the SST and skin temperature are equal (Fig. 4.26 a). It is most probably due to the employed ensemble size differences for the Caspian Sea (as mentioned above, only three GCM ensemble used for the perturbation of SST forcing for the Caspian Sea for the data availability concerned). Fig. 4.26 a affirms this assumption by yielding almost equal SST and skin temperature in the Black Sea and the Mediterranean Sea. The slight differences are below 0.1 °C, which is probably due to the not used SST. Moreover, these three GCMs (CMCC-CM2-SR5, CMCC-ESM2, and HadGEM3-GC31-MM) consistently yield warmer SST projections than the full ensemble over the Aegean, Mediterranean, and Black seas, besides the Caspian Sea (Fig. 4.26 b). Fig. 4.26 a shows that not only the summer and fall seasons but also the winter and spring seasons give differential heating between SST and skin temperatures. The approximate maximum values of the differential heating are 0.75 °C, 1.1 °C, 0.95 °C, and 0.65 °C for the winter, spring, summer, and fall seasons, respectively.

Table 4.3 SST availability across the CMIP6 GCMs. Cnbu refers to “could not be used”.

CMIP6 GCMs	SST availability		
	Black Sea	Mediterranean Sea	Caspian Sea
AWI-CM-1-1-MR	Cnbu	Cnbu	Cnbu
BCC-CSM2-MR	Yes	Yes	No
CMCC-CM2-SR5	Yes	Yes	Yes
CMCC-ESM2	Yes	Yes	Yes
CNRM-CM6-1-HR	Yes	Yes	No
EC-Earth3	Yes	Yes	No
EC-Earth3-CC	Yes	Yes	No
EC-Earth3-Veg	Yes	Yes	No
FGOALS-f3-L	Cnbu	Cnbu	Cnbu
GFDL-ESM4	Yes	Yes	No
HadGEM3-GC31-MM	Yes	Yes	Yes
MPI-ESM1-2-HR	Yes	Yes	No
MRI-ESM2-0	Yes	Yes	No

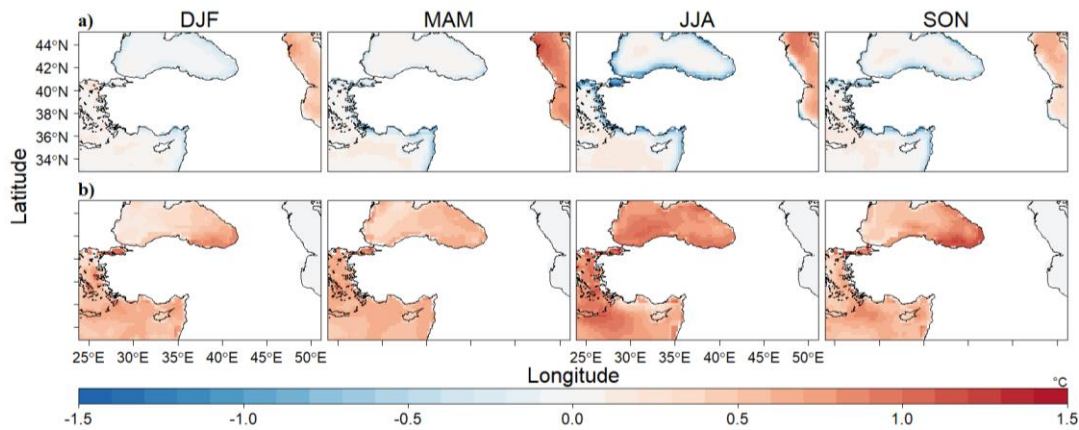


Figure 4.26. The long-term (between 2071-2100 (future SSP5-8.5 scenario) and 1985-2014 (historical) periods) seasonal mean warming differences: a) between sea-surface temperature and skin temperature of all available GCMs, b) between three GCMs (CMCC-CM2-SR5, CMCC-ESM2, HadGEM3-GC31-MM) SST and all available GCM ensemble SST (three GCMs SST increase minus full ensemble SST increase). The coastal regions exhibit a blocky cooler appearance due to the bilinear interpolation process from coarse to fine resolution. It was avoided in the interpolation step of the WRF-preprocess.

Here we perform a ten-year-long simulations over the Caucasus and the nearby regions for the future period to examine the effects of the differential heating. The ten-year-long simulations seem sufficient to obtain precipitation change signals at a quite reasonable level. The simulation is based on the cooling Caspian Sea as much as the approximate maximum values mentioned above. The SST was still updated in this simulation, but spectral nudging was turned off. All remaining physics and dynamic options were the same as in the main simulations. The simulation was performed between pseudo 1994-2004, and the first year was discarded as a spin-up. The reference simulation was kept the same between 1995-2004 but cropped over the region of interest.

The winter season shows the strongest nonlinear reaction in the surface anticyclone and the near-surface temperature on the land, even though the Caspian Sea was cooled less than the spring and summer seasons (Fig. 4.27 and Fig. 4.28). The near-

surface temperature increase on the land approaches up to 2 °C, and a decrease on the Caspian Sea reaches up to 0.45 °C resulting in the attenuation of the land-sea temperature contrast. It enhances the surface anticyclone and accordingly reshapes the low-level circulation (Tuel and Eltahir, 2020). The vertical pressure velocity is more potent for both directions in all tropospheric levels than in the main simulations (Fig. 4.21 and Fig. 4.29). The specific humidity decrease is around 0.6 g/kg in the lower troposphere over the land, while near-surface specific humidity differences are mostly below to 0.1 g/kg compared to the main simulation (Fig. 4.19, 4.20, 4.30). However, the dew point depression decreases more than the main simulation and spreads a more expansive area in the Caucasus and the nearby regions (Fig. 4.28). Overall, these factors offer the distinctive climatic forces; nevertheless, the precipitation response of the region's land areas resembles the main simulation (Fig. 4.15 and Fig. 4.31).

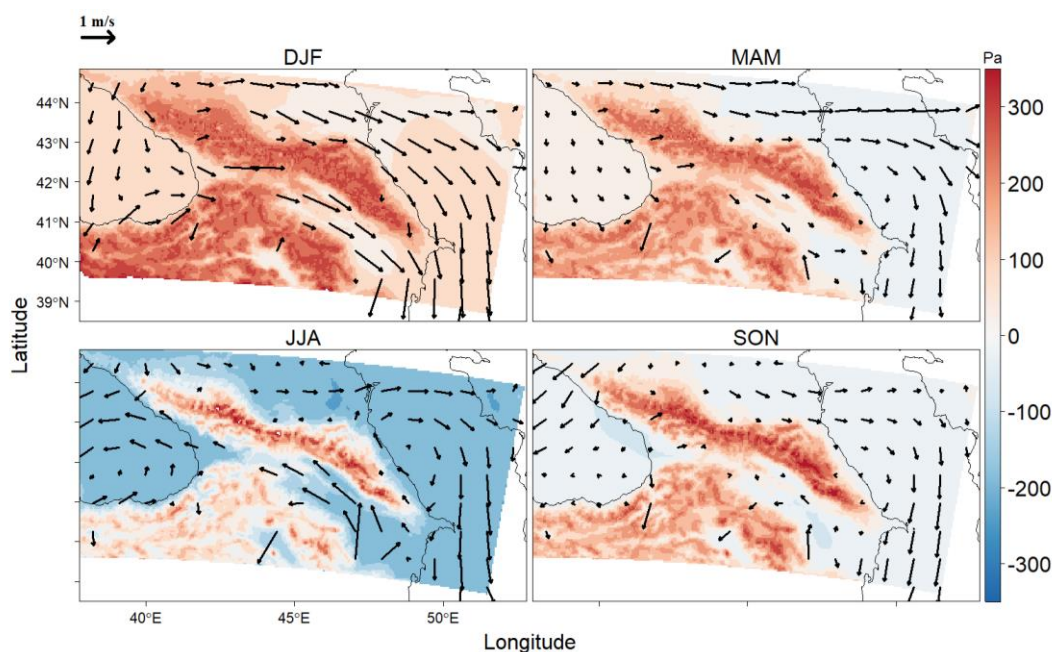


Figure 4.27. The low-level (850 hPa) circulation (winds as vectors) and SLP (shadings) change between 1995-2004 and the corresponding pseudo future period for each season obtained from the WRF simulations for the Caucasus and nearby regions. The wind vectors are in the units of m/s and sea-level pressure is in the units of pascal. The reference vector is presented in the upper left.

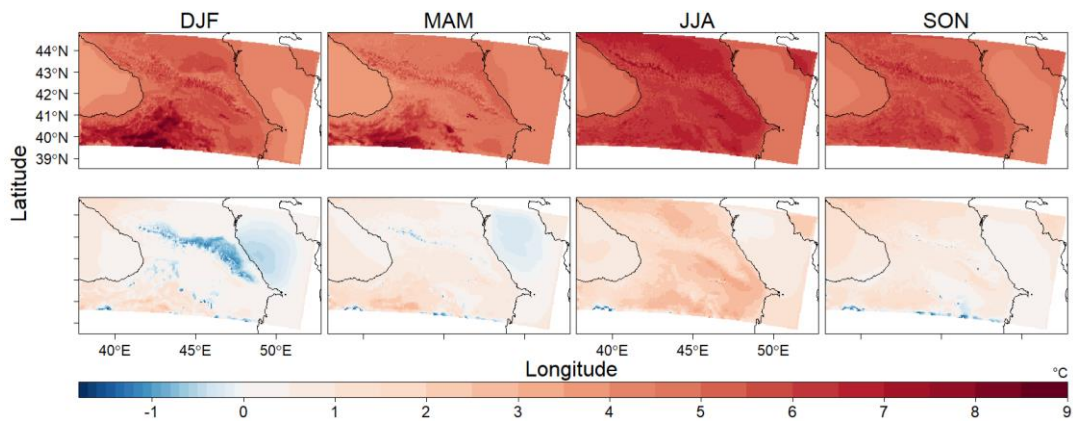


Figure 4.28. The near-surface temperature (at the top) and dew-point depression (at the bottom) change between 1995-2004 and the corresponding pseudo future period in the units of °C for each season obtained from the WRF simulations for the Caucasus and nearby regions. The dew-point depression is averaged with the values between the near-surface and 700 hPa pressure level.

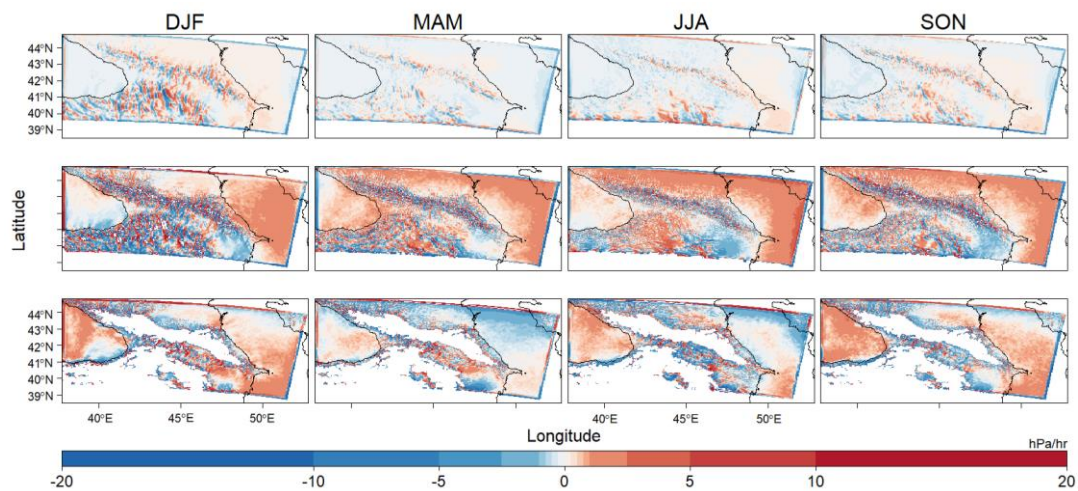


Figure 4.29. The vertical pressure velocity (omega) change between 1995-2004 and the corresponding pseudo future period in the units of hPa/hr for each season obtained from the WRF simulations for the Caucasus and nearby regions. The omega changes are presented in 200 hPa (in the top), 500 hPa (in the middle), and 850 hPa (in the bottom) pressure levels.

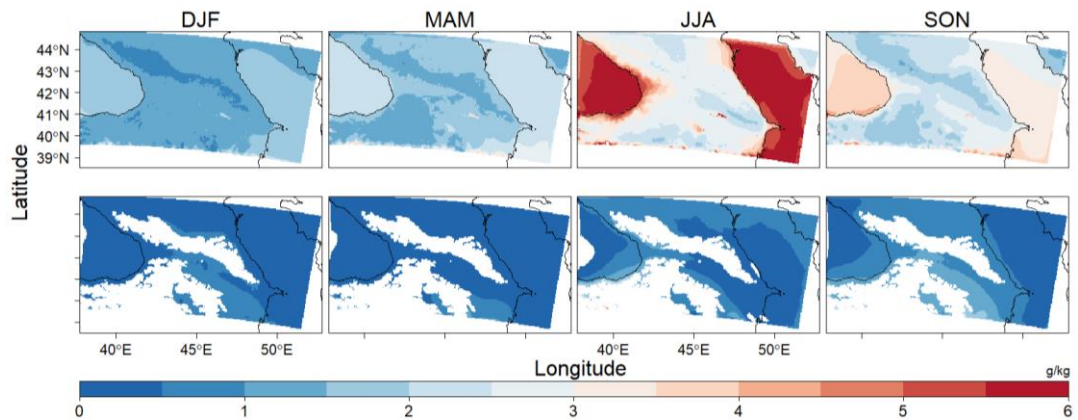


Figure 4.30. The near-surface (2-meter; at the top) and low-level (850 hPa; at the bottom) specific humidity change between 1995-2004 and the corresponding pseudo future period in the units of g/kg for each season obtained from the WRF simulations for the Caucasus and nearby regions.

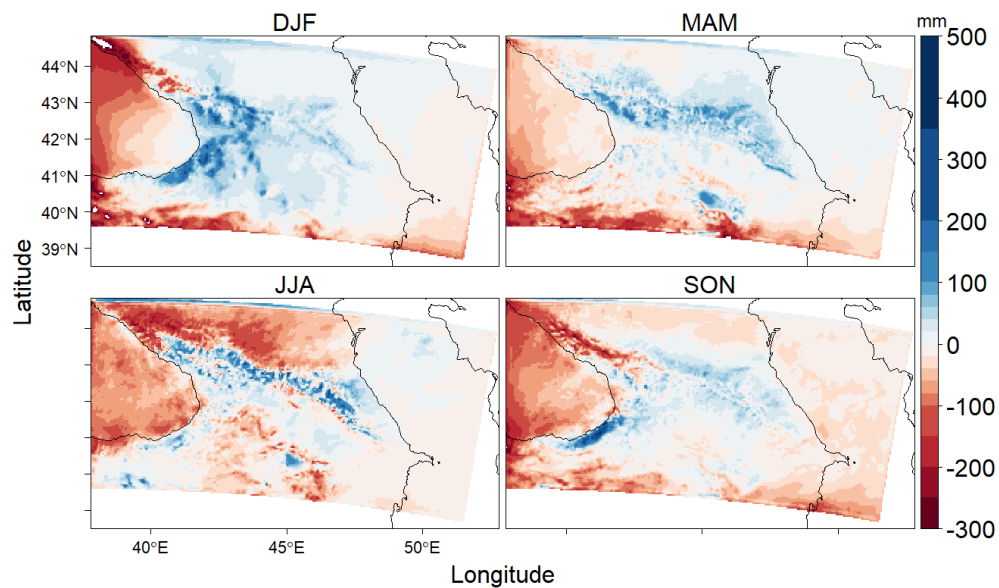


Figure 4.31. The seasonal precipitation change between 1995-2004 and the corresponding pseudo future period in the units of mm obtained from the WRF simulations for the Caucasus and nearby regions.

Cooling the Caspian Sea at 1.1 °C results in around 0.7 °C decrease in near-surface temperature over that sea in spring (Fig. 4.22 and Fig. 4.28). However, the near-surface temperature increase over land is much weaker than in the winter. Therefore, the anticyclonic low-level circulation response is weaker (Fig. 4.27). The mid-

tropospheric subsidence prevails over the region, while the air ascent is more prominent in the lower troposphere (Fig. 4.29). The vertical pressure velocity is stronger in both directions in the upper troposphere. The specific humidity decrease is more potent than in the winter and reaches up to 1.5 g/kg in the lower troposphere over the land (Fig. 4.30). The near-surface specific humidity differences are mostly between 0.2-0.4 g/kg. The precipitation increase draws a similar pattern with the main simulation over the highland areas of Caucasus; however, the remaining regions show a weaker increase or even decreasing patterns (Fig. 4.15 and Fig. 4.31).

The summer season shows a striking reaction against the cooling Caucasus in decreasing low-level specific humidity and changing the direction of the low-level wind field (Fig. 4.17, 4.20, 4.27, 4.30). Cooling the Caspian Sea in summer at 0.95 °C has also broken the SLP change balance between that sea and the Black Sea. The SLP in the Caspian Sea has increased; however, as a nonlinear reaction, the increase in the Black Sea was more. The specific humidity increase in the lower troposphere drops to around one-tenth of the main simulation, albeit the drop in the near-surface not as much dramatic (Fig. 4.19, 4.20, 4.30). The low-level wind field turns its direction 180 degrees over the northern Caucasus and forms a northerly pattern along the eastern Caspian Sea. Nevertheless, the wind pattern resembles the main simulations along the southern Caucasus and the Black Sea. Strong mid-tropospheric subsidence is taking shape over the region, which is strongly contrary to the air ascent observed in the main simulations (Fig. 4.21 and Fig. 4.29). The subsidence even exceeds the expectations of the GCM ensemble (Fig. 4.24). However, there are still air ascent regions in the mid-troposphere and, more commonly, in the upper-troposphere, which may explain the precipitation increase in the heights of the Caucasus (Fig. 4.31). In the additional simulation, this increase mostly does not exceed 200 mm.

The fall season resembles summer but with a weakening low-level circulation and a slightly moistening lower-troposphere (Fig. 4.27 and Fig. 4.30). The subsidence diminishes over the southern Caucasus in the mid-troposphere, serving slightly increased precipitation (Fig. 4.29 and Fig. 4.31). Nevertheless, the increase does not

propagate towards the south as in the main simulation. To the northwestern edge of the Caucasus, the precipitation decrease is more prominent than those in the main simulation showing the effect of a potent contradiction of the vertical pressure velocity and the diverging wind field. Türkiye's eastern Black Sea Region coasts exhibit a substantial precipitation increase, as in the main simulation. Here, the moisture flux does not diverge from the coast to the sea as in summer, and the mid-tropospheric subsidence locally vanishes in the region.

CHAPTER 5

DISCUSSION

We have comprehensively investigated the climatic change over Türkiye and large-scale EMBS across successive and interrelating three studies in the context of this thesis. The first study showed that higher ECS is present with the CMIP6 GCMs when comparing their same family counterpart CMIP5 GCMs in parallel with the literature. However, only one correspondent GCM family (MRI) exists between CMIPs in the best-performing four-member ensembles. Therefore, the effect of the high ECS is not seen fairly between ensembles. On the other hand, near-surface temperature projections spatially resemble each other across the SSP2-4.5 and SSP5-8.5 scenarios. However, the warming range of the SSP5-8.5 is almost twofold that of the SSP2-4.5. The spatial resemblance is also present for precipitation, though not much as temperature. In general, precipitation increase/decrease is more enhanced with the SSP5-8.5 in terms of percent changes. The mean biases considerably decrease with the CMIP6 GCM ensemble compared to CMIP5 GCMs, offering a performance improvement of CMIP6 via better-represented physics with the parameterization schemes.

The CMIP6 GCM ensemble of the first study shows maximum warming in summer with a relatively homogeneous appearance. The fall season also shows high warming values, especially over southeastern Türkiye, showing the summer season extension through the fall season. Summer drying accompanies the warming over the country, which has a similar extension pattern to the fall season. The summer warming and drying over the western and northern Türkiye are consistent with the findings of (Barcikowska et al., 2019). In a coarse resolution, the Black Sea Region experiences a statistically significant summer precipitation decrease (up to 31%) in all future periods and scenarios. It contradicts the high-resolution simulations which are given

in the third study. The cause-and-effect relation is discussed in the following parts of this section.

The winter drying and warming over southern Türkiye are consistent with the findings of (Tuel and Eltahir, 2020), who stated that the anomalous ridge formation over the Mediterranean (with causes) suppresses precipitation. In a coarse resolution, the GCM ensemble projects a precipitation decrease of up to 25% and a near-surface temperature increase of up to 2.5 °C (4.5 °C) under the SSP2-4.5 (SSP5-8.5) over the southern regions towards the end of this century. At the same time, a winter precipitation increase of up to 15% (25%) is expected under the SSP2-4.5 (SSP5-8.5) over the northern regions, particularly the eastern Black Sea Region and northeastern Anatolia. These findings of the first study are well captured in a high-resolution simulations of the third study.

The CMIP6 GCMs show a lower inter-model variability for precipitation and near-surface temperature than that of CMIP5 in the historical period, offering a narrower uncertainty range. Therefore, more consistent projections are expected with the CMIP6. On the other hand, the CMIP6 exhibits a higher anomaly in maximum declines (~2.5%) in the medium term and a lower anomaly in mean declines (~2%) in the near term in annual precipitation in the coming century. Besides, a higher anomaly in the maximum increase (~6.5%) in the long term is projected. Moreover, the higher standard deviation values offer that extreme precipitation and temperature tendencies will prevail over Türkiye in the coming century, according to the CMIP6. It is more prominent in the smaller spatiotemporal scales, demonstrating the significance of the regional impact.

The second study conducted precipitation sensitivity tests to prepare for the long-term PGW runs in a high resolution in the context of the third study. The high sensitivity of the configurations implies the importance of revealing the best-performing one to obtain more reliable climate simulations for the region of interest. The daily precipitation correlation values of the 60 configurations are between 0.51 and 0.65. As for RMSE, this range is between 4- and 5 mm. The resultant best-

performing configuration was distinguished by correlation values since the error values can be reduced by the post-processing tools. The validation step of the third study should not have given the correlation values consistently lower than 0.65 to make sure that the best-performing configuration works properly. It is the case for the retrospective simulations (1995-2014) of the third study, which yield even better results than the best-performing simulation of the second study, except 1999 and 2014. As for RMSE, there is neither prominent performance improvement nor performance decrease was observed with the simulation between 1995 and 2014. These are testimony to the robustness of the retrospective simulations of the third study.

In a high resolution, the third study broadly affirms the findings of the literature and the state-of-the-art CMIP6 GCM ensemble, which show that the Mediterranean is one of the climate change hotspots giving strong warming and drying reactions to the scaling up GHGs concentrations (Giorgi, 2006; Giorgi and Lionello, 2008; Barcikowska et al., 2018; Tuel and Eltahir, 2020; Bağçaci et al., 2021). Nevertheless, it should be annotated the added utility of the WRF simulations. For instance, the GCM ensemble (in both the first and third study) shows maximum warming in the summer season, which has a more homogenous view than the downscaled simulations. In contrast, the WRF simulations show a detailed appearance of maxima over the northeastern Anatolian Plateau in winter, whose effect also propagates into spring. The northeastern plateau is under snow cover in today's winter and early spring, which largely vanishes in future simulations. It causes the snow-albedo feedback to diminish, therefore increasing temperature. Accordingly, it impacts the snowmelt runoff timing, hence water resources which are of critical importance for the region (Sen et al., 2011; Yucel et al., 2015). On the other hand, the winter and spring precipitation climatology is generally well captured with the WRF simulations. We clearly see the impact of the development of the intense anomalous ridge in the circulation and precipitation response. Tuel and Eltahir (2020) showed that the attenuation of land-sea temperature contrast and large-scale upper tropospheric flow changes have a comparable impact on the development of the

anomalous ridge resulting in the decline of winter precipitation (as also in the first study) over the Mediterranean. Here in third study, we did not conduct any component analysis; therefore, we cannot claim which effect is more substantial. Nevertheless, we can confirm that the attenuation of the land-sea temperature contrast yields an anticyclonic environment over the Caucasus and nearby regions. However, our additional simulation shows that attenuation of the land-sea temperature contrast does not directly suppress precipitation over the easternmost coasts of the Black Sea and near inland regions. It is opposed to Tuel and Eltahir (2020), which shows a substantial decrease in those regions. There are some factors which may lie behind this controversy. For example, the differential heating of the Caspian and Black Seas exists between the main and additional simulations, and the region might give a nonlinear reaction to it. The higher resolution we used in the third study might be another factor since the region's topography is extremely complex. Due to the less SST-sensitivity of these seasons in precipitation change compared to the summer and fall, it increases our confidence in simulating the future rain conditions of the region. The parallelism in the WRF simulations and GCM ensemble shows that the outside the large-scale effect of the anomalous ridge developed over the Mediterranean, local circulation changes govern the future precipitation regime more.

Barcikowska et al. (2019) stated that the Etesians and SNAO's cooling effect unable to offset the GHGs-induced strong warming over the region encompassing EMBS. Instead, they claimed that surface warming governs the local atmospheric circulation, and the temperature and precipitation balance, as the heat-low becomes prominent. We should note that we did not do any component analysis in the summer and fall seasons as in winter and spring. Nevertheless, our simulations show that the Etesian winds intensify in summer, which extends over the fall season with a diminishing influence, in parallel with the literature. The GCM ensemble used in the third study also reveals the trace of the SNAO, as Barcikowska et al. (2019) indicated. These factors may partly offset the existing high warming response of the EMBS. However, we see the heat low effect in the summer season over the EMBS.

It not only enhances warming (as also in the first study) but also allows for air ascent movement more to the extent that subsidence weakens in the tropospheric levels. It is probably responsible for the slight precipitation increase (as partly in the first study) over the Anatolian peninsula and southern region since other factors like increased dew-point temperature and land-sea temperature contrast in the summer season favour suppressed precipitation. A decrease in precipitation over the Mediterranean and Aegean coasts of Türkiye in the fall season (as also in the first study) seems related to the diminishing heat-low effect in summer. The region located in the southern Persian trough shows no remarkable precipitation increase, which is probably due to the advected air from the Arabian Desert being dry. The reverse sign in precipitation over the northwestern EMBS, i.e., a decrease in summer and an increase in fall, is thought to be due to subsidence change differences in the low and mid-troposphere and the positioning wind pattern change relative to the mountain range. Moreover, the dewpoint depression increase in summer by nearly 1 °C more than in the fall season. A decrease in precipitation pattern in summer diminishes over the northernmost Black Sea coast of Türkiye in fall season which seems related to the weakening mid-tropospheric subsidence. The remaining regions, except northeastern EMBS, show parallelism for precipitation with these two seasons.

The abnormal appearance of precipitation increase in the summer and fall seasons, which both contradict the GCM ensemble in the first and third studies, over the Caucasus and nearby regions directed us to configure the additional simulation. However, the additional simulation does not directly mean the foolproof climatic future of the region since some uncertainties exist. For example, the Caspian Sea was linearly cooled among the seasons, with approximate maximum differences between long-term SST and skin temperatures. It results in some parts of the Caspian Sea being cooler, though not by much than the predicted skin temperature increase. Moreover, the epicentre of the anomalous precipitation increase was cropped, and spectral nudging was turned off, which allowed the WRF model to evolve freely.

Therefore, the additional simulation should be perceived as a sensitivity test, albeit the factors above impact, giving two scenario range between differential heating.

The main simulations and the GCM ensemble (in the third study) show that the strong anomalous ridge developed over the Mediterranean does not influence circulation in the Caucasus and the nearby regions in the winter and spring seasons. However, the same models show that the region is influenced by the heat low developed over the eastern Mediterranean in the summer and fall seasons. Therefore, turning off the spectral nudging may explain why the summer and fall seasons' circulation changes are more dramatic than the other seasons because the flow along the northeastern Caucasus to the southern boundary of the Caspian Sea reverses. Outside the large-scale effect, the wind patterns here follow SLP decrease maxima over the eastern coast of the Caspian Sea and the southeasternmost of the region in summer. In the fall season, the low-level flow along the region mentioned above has an anticyclonic appearance. Besides these factors, a dramatic decrease in the low-level specific humidity in summer and an increase in the mid-tropospheric subsidence in summer and fall mainly explain precipitation suppression in the region. As a nonlinear response to the cooling Caspian Sea, land surface warming enhancement, except in the highlands of the Caucasus, may be another factor in the suppression of precipitation, as Barcikowska et al. (2019) stated. On the other hand, the authors' findings show a strong precipitation increase over the highlands of the Caucasus in the summer season (their Fig. 7), which conforms with our both simulations (main and additional simulations in the third study). It shows that the statistically significant precipitation decreases obtained with the GCM ensemble (in both first and third study) may be reversed through the added utility of the high-resolution regional climate models.

CHAPTER 6

CONCLUSION

This thesis aimed to ascertain the change in the future climatic outlook of Türkiye and large-scale EMBS with the state-of-the-art CMIP6 GCM ensemble in a coarse resolution and PGW-based dynamic downscaling in a high resolution. The first study compared the CMIP6 to the CMIP5 to see whether any improvement in the climate projections becomes prominent for the Türkiye domain. The results showed the outperformance of CMIP6, particularly for precipitation. The future projections of CMIP6 yield higher near-surface temperature values, and the maximum and minimum anomalies of the individual ensemble members are more prominent than the CMIP5. Moreover, the CMIP6 indicates warming acceleration by demonstrating early near-surface temperature increases in minimum anomalies throughout the near term. The corresponding substantial precipitation enhancement (~8% higher) of the CMIP6 is present in maximum anomaly increases in this near term. The annual mean precipitation decreases are generally fewer with the CMIP6; however, the extremes in the maximum increase/decrease are substantially higher compared to the CMIP5. As a consequence, the drying pattern is less apparent with the CMIP6 GCMs. The underestimated precipitation patterns of the CMIP5, which results in a tendency to the dryer climate conditions, were seen to ameliorate with the CMIP6. The fewer intermodel variability for precipitation and near-surface temperature of the CMIP6 renders a steadier ensemble.

The winter season precipitation pattern becomes different by showing substantial precipitation anomalies over the south (a decrease) and north (an increase) of the Türkiye domain. Spring precipitation spatially resembles winter precipitation with more spread drying, particularly in the long term. These are well captured with the high-resolution WRF simulations in the third study. As for the summer and fall

seasons, a huge contradiction appeared between the first and third studies. The first study showed substantial precipitation decrease over the Aegean and Black Sea Regions, especially in summer. The decrease was more in quantity over the Black Sea Region, which shows smoothed seasonality (four-season rainy) compared to the Aegean Region. However, in the incompleteness of the SSTs of the Caspian Sea, the main WRF simulations of the first study showed an anomalous precipitation increase over the northeastern regions, Caucasus and its surroundings, in the summer and fall seasons. In fact, the winter and spring seasons also had incomplete SSTs for the Caspian Sea, but they were less sensitive than the other two seasons by locating outside the large-scale effects. The main and additional simulations of the third study showed two scenarios for the region's future since the incompleteness of the SSTs prevented a foolproof view in the SST-sensitive seasons. The first scenario indicated that if the Caspian Sea were warmer, much as the values mentioned above, the Caucasus and nearby regions would experience an abnormal precipitation increase. The second scenario remarked that the precipitation would be suppressed if the Caucasus and nearby regions were outside the large-scale heat-low effect. In both cases, the precipitation was expected to increase over the highlands of the Caucasus and Türkiye's eastern Black Sea coasts. The modelling community should be aware of the SST existence in advance, especially in such SST-sensitive areas.

Now, everything is ready to run a hydrologic model (i.e., WRF-Hydro) to see climate change effects on the water resources of Türkiye in the context of future works. The flood and drought risks in vulnerable regions can be revealed with the data obtained in this thesis, and other hydroclimatic risks can be reassessed with the results of WRF-Hydro simulations. The climatic extremes endangering human health (i.e., heat waves) can be searched with the outputs of this thesis. The expected loss of snow cover areas of the country and its results can also be uncovered. With the experiences gained in this thesis, individual dynamical downscaling of the GCMs (providing that the selected GCMs have complete SST information) can be conducted to support or discuss the results obtained here.

REFERENCES

- Ahmed, K., Sachindra, D.A., Shahid, S., Demirel, M.C., Chung, E.S., 2019. Selection of multi-model ensemble of general circulation models for the simulation of precipitation and maximum and minimum temperature based on spatial assessment metrics. *Hydrol. Earth Syst. Sci.* 23, 4803–4824. <https://doi.org/10.5194/hess-23-4803-2019>
- Allen, R.G., Pereira, L.S., Raes, D., Smith, M., 1998. Crop evapotranspiration - Guidelines for computing crop water requirements - FAO Irrigation and drainage paper 56, Irrigation and Drainage. <https://doi.org/10.1016/j.eja.2010.12.001>
- Almazroui, M., Saeed, F., Saeed, S., Nazrul Islam, M., Ismail, M., Klutse, N.A.B., Siddiqui, M.H., 2020. Projected Change in Temperature and Precipitation Over Africa from CMIP6. *Earth Syst. Environ.* <https://doi.org/10.1007/s41748-020-00161-x>
- Alpert, P., Baldi, M., Ilani, R., Krichak, S., Price, C., Rodó, X., Saaroni, H., Ziv, B., Kishcha, P., Barkan, J., Mariotti, A., Xoplaki, E., 2006. Chapter 2 Relations between climate variability in the Mediterranean region and the tropics: ENSO, South Asian and African monsoons, hurricanes and Saharan dust. *Dev. Earth Environ. Sci.* 4, 149–177. [https://doi.org/10.1016/S1571-9197\(06\)80005-4](https://doi.org/10.1016/S1571-9197(06)80005-4)
- Anagnostopoulou, C., Zanis, P., Katragkou, E., Tegoulas, I., Tolika, K., 2014. Recent past and future patterns of the Etesian winds based on regional scale climate model simulations. *Clim. Dyn.* <https://doi.org/10.1007/s00382-013-1936-0>
- Annan, J., Arndt, S., Añel, J.A., Bekki, S., Butler, T., Colette, A., Folberth, C., Folberth, G.A., Goelzer, H., Grewe, V., Gross, L., Halloran, P., Ham, D., Hargreaves, J., Huybrechts, P., Jackson, B., Järvi, L., Jöckel, P., Kala, J., Kato, T., Kerkweg, A., Knote, C., Koller, J., Kurtz, W., Lauer, A., Lawrence, D.,

- Levy, C., Lo, M.-H., Maddison, J.R., Mann, G., Marras, S., Marsh, R., Marti, O., Maussion, F., McCluskey, C., Mills, R., Morgenstern, O., Munhoven, G., Müller, C., Neal, J., Neale, R., O'Connor, F., Peylin, P., Phipps, S., Pissot, I., Poulet, T., Pye, H., Remy, S., Robel, A., Roche, D., Sander, R., Sandu, A., Sato, H., Sierra, C., Stenke, A., Topping, D., Tost, H., Ullrich, P., Unterstrasser, S., Valcke, S., van Heerwaarden, C., Wang, Q., Wickert, A., Williams, J., Yool, A. (Eds.), Eyring, V. (Coord.), 2020. Special issue | Coupled Model Intercomparison Project Phase 6 (CMIP6) Experimental Design and Organization [WWW Document]. Geosci. Model Dev. URL https://www.geosci-model-dev.net/special_issue590.html (accessed 5.23.20).
- Argüeso, D., Hidalgo-Muñoz, J.M., Gámiz-Fortis, S.R., Esteban-Parra, M.J., Dudhia, J., Castro-Díez, Y., 2011. Evaluation of WRF parameterizations for climate studies over southern Spain using a multistep regionalization. *J. Clim.* <https://doi.org/10.1175/JCLI-D-11-00073.1>
- Bağçacı, S.Ç., Yucel, I., Duzenli, E., Yilmaz, M.T., 2021. Intercomparison of the expected change in the temperature and the precipitation retrieved from CMIP6 and CMIP5 climate projections: A Mediterranean hot spot case, Turkey. *Atmos. Res.* <https://doi.org/10.1016/j.atmosres.2021.105576>
- Barcikowska, M.J., Kapnick, S.B., Feser, F., 2018. Impact of large-scale circulation changes in the North Atlantic sector on the current and future Mediterranean winter hydroclimate. *Clim. Dyn.* <https://doi.org/10.1007/s00382-017-3735-5>
- Barcikowska, M.J., Kapnick, S.B., Krishnamurty, L., Russo, S., Cherchi, A., Folland, C.K., 2019. Changes in the future summer Mediterranean climate: contribution of teleconnections and local factors. *Earth Syst. Dyn. Discuss.* 1–43. <https://doi.org/10.5194/esd-2018-85>
- Boucher, O., Servonnat, J., Albright, A.L., Aumont, O., Balkanski, Y., Bastrikov, V., Bekki, S., Bonnet, R., Bony, S., Bopp, L., Braconnot, P., Brockmann, P., Cadule, P., Caubel, A., Cheruy, F., Codron, F., Cozic, A., Cugnet, D.,

D'Andrea, F., Davini, P., de Lavergne, C., Denvil, S., Deshayes, J., Devilliers, M., Ducharne, A., Dufresne, J.L., Dupont, E., Éthé, C., Fairhead, L., Falletti, L., Flavoni, S., Foujols, M.A., Gardoll, S., Gastineau, G., Ghattas, J., Grandpeix, J.Y., Guenet, B., Guez, L.E., Guilyardi, E., Guimberteau, M., Hauglustaine, D., Hourdin, F., Idelkadi, A., Joussaume, S., Kageyama, M., Khodri, M., Krinner, G., Lebas, N., Levavasseur, G., Lévy, C., Li, L., Lott, F., Lurton, T., Luysaert, S., Madec, G., Madeleine, J.B., Maignan, F., Marchand, M., Marti, O., Mellul, L., Meurdesoif, Y., Mignot, J., Musat, I., Ottlé, C., Peylin, P., Planton, Y., Polcher, J., Rio, C., Rochetin, N., Rousset, C., Sepulchre, P., Sima, A., Swingedouw, D., Thiéblemont, R., Traore, A.K., Vancoppenolle, M., Vial, J., Vialard, J., Viovy, N., Vuichard, N., 2020. Presentation and Evaluation of the IPSL-CM6A-LR Climate Model. *J. Adv. Model. Earth Syst.* <https://doi.org/10.1029/2019MS002010>

Bozkurt, D., Sen, O.L., 2013. Climate change impacts in the Euphrates-Tigris Basin based on different model and scenario simulations. *J. Hydrol.* 480, 149–161. <https://doi.org/10.1016/j.jhydrol.2012.12.021>

Bozkurt, D., Turuncoglu, U., Sen, O.L., Onol, B., Dalfes, H.N., 2012. Downscaled simulations of the ECHAM5, CCSM3 and HadCM3 global models for the eastern Mediterranean-Black Sea region: Evaluation of the reference period. *Clim. Dyn.* 39, 207–225. <https://doi.org/10.1007/s00382-011-1187-x>

Chang, W., Stein, M.L., Wang, J., Kotamarthi, V.R., Moyer, E.J., 2016. Changes in spatiotemporal precipitation patterns in changing climate conditions. *J. Clim.* <https://doi.org/10.1175/JCLI-D-15-0844.1>

Chen, F., Dudhia, J., 2001. Coupling and advanced land surface-hydrology model with the Penn State-NCAR MM5 modeling system. Part I: Model implementation and sensitivity. *Mon. Weather Rev.* [https://doi.org/10.1175/1520-0493\(2001\)129<0569:CAALSH>2.0.CO;2](https://doi.org/10.1175/1520-0493(2001)129<0569:CAALSH>2.0.CO;2)

Cornes, R.C., van der Schrier, G., van den Besselaar, E.J.M., Jones, P.D., 2018. An

- Ensemble Version of the E-OBS Temperature and Precipitation Data Sets. *J. Geophys. Res. Atmos.* <https://doi.org/10.1029/2017JD028200>
- Demircan, M., Gürkan, H., Eskioglu, O., Arabaci, H., Coşkun, M., 2017. Climate Change Projections for Turkey: Three Models and Two Scenarios. *Turkish J. Water Sci. Manag.* 1, 22–43. <https://doi.org/10.31807/tjwsm.297183>
- Dutheil, C., Menkes, C., Lengaigne, M., Vialard, J., Peltier, A., Bador, M., Petit, X., 2020. Fine-scale rainfall over New Caledonia under climate change. *Clim. Dyn.* <https://doi.org/10.1007/s00382-020-05467-0>
- Duzenli, E., Tabari, H., Willems, P., Yilmaz, M.T., 2018. Decadal variability analysis of extreme precipitation in Turkey and its relationship with teleconnection patterns. *Hydrol. Process.* 32, 3513–3528. <https://doi.org/10.1002/hyp.13275>
- Duzenli, E., Yucel, I., Pilatin, H., Yilmaz, M.T., 2021. Evaluating the performance of a WRF initial and physics ensemble over Eastern Black Sea and Mediterranean regions in Turkey. *Atmos. Res.* 248. <https://doi.org/10.1016/j.atmosres.2020.105184>
- ECMWF, 2020. E-OBS daily gridded meteorological data for Europe from 1950 to present derived from in-situ observations [WWW Document]. <https://doi.org/10.24381/cds.151d3ec6>
- Erler, A.R., Peltier, W.R., 2017. Projected hydroclimatic changes in two major river basins at the Canadian west coast based on high-resolution regional climate simulations. *J. Clim.* <https://doi.org/10.1175/JCLI-D-16-0870.1>
- Eshel, G., Farrell, B.F., 2000. Mechanisms of eastern Mediterranean rainfall variability. *J. Atmos. Sci.* [https://doi.org/10.1175/1520-0469\(2000\)057<3219:MOEMRV>2.0.CO;2](https://doi.org/10.1175/1520-0469(2000)057<3219:MOEMRV>2.0.CO;2)
- Eyring, V., Bony, S., Meehl, G.A., Senior, C.A., Stevens, B., Stouffer, R.J., Taylor, K.E., 2016. Overview of the Coupled Model Intercomparison Project Phase 6

- (CMIP6) experimental design and organization. *Geosci. Model Dev.* 9, 1937–1958. <https://doi.org/10.5194/gmd-9-1937-2016>
- Flaounas, E., Bastin, S., Janicot, S., 2011. Regional climate modelling of the 2006 West African monsoon: Sensitivity to convection and planetary boundary layer parameterisation using WRF. *Clim. Dyn.* <https://doi.org/10.1007/s00382-010-0785-3>
- Flaounas, E., Drobinski, P., Bastin, S., 2013. Dynamical downscaling of IPSL-CM5 CMIP5 historical simulations over the Mediterranean: Benefits on the representation of regional surface winds and cyclogenesis. *Clim. Dyn.* <https://doi.org/10.1007/s00382-012-1606-7>
- Forster, P.M., Maycock, A.C., McKenna, C.M., Smith, C.J., 2020. Latest climate models confirm need for urgent mitigation. *Nat. Clim. Chang.* <https://doi.org/10.1038/s41558-019-0660-0>
- Fujihara, Y., Tanaka, K., Watanabe, T., Nagano, T., Kojiri, T., 2008. Assessing the impacts of climate change on the water resources of the Seyhan River Basin in Turkey: Use of dynamically downscaled data for hydrologic simulations. *J. Hydrol.* 353, 33–48. <https://doi.org/10.1016/j.jhydrol.2008.01.024>
- Garrido, J.L., González-Rouco, J.F., Vivanco, M.G., Navarro, J., 2020. Regional surface temperature simulations over the Iberian Peninsula: evaluation and climate projections. *Clim. Dyn.* <https://doi.org/10.1007/s00382-020-05456-3>
- GDM, 2019. Official statistics/ parameter analysis [WWW Document]. URL <https://www.mgm.gov.tr/FILES/resmi-istatistikler/parametreAnalizi/Turkiye-Ortalama-Sicaklik-2019.pdf>
- Gettelman, A., Hannay, C., Bacmeister, J.T., Neale, R.B., Pendergrass, A.G., Danabasoglu, G., Lamarque, J.F., Fasullo, J.T., Bailey, D.A., Lawrence, D.M., Mills, M.J., 2019. High Climate Sensitivity in the Community Earth System Model Version 2 (CESM2). *Geophys. Res. Lett.* 46, 8329–8337. <https://doi.org/10.1029/2019GL083978>

- Giorgi, F., 2006. Climate change hot-spots. *Geophys. Res. Lett.* 33. <https://doi.org/10.1029/2006GL025734>
- Giorgi, F., Lionello, P., 2008. Climate change projections for the Mediterranean region. *Glob. Planet. Change* 63, 90–104. <https://doi.org/10.1016/j.gloplacha.2007.09.005>
- Gorguner, M., Kavvas, M.L., 2020. Modeling impacts of future climate change on reservoir storages and irrigation water demands in a Mediterranean basin. *Sci. Total Environ.* <https://doi.org/10.1016/j.scitotenv.2020.141246>
- Gorguner, M., Kavvas, M.L., Ishida, K., 2019. Assessing the impacts of future climate change on the hydroclimatology of the Gediz Basin in Turkey by using dynamically downscaled CMIP5 projections. *Sci. Total Environ.* <https://doi.org/10.1016/j.scitotenv.2018.08.167>
- Grell, G.A., Dudhia, J., Stauffer, D.R., 1994. A Description of the Fifth Generation Penn State/NCAR Mesoscale Model (MM5), NCAR TECHNICAL NOTE.
- Grose, M.R., Narsey, S., Delage, F.P., Dowdy, A.J., Bador, M., Boschat, G., Chung, C., Kajtar, J.B., Rauniyar, S., Freund, M.B., Lyu, K., Rashid, H., Zhang, X., Wales, S., Trenham, C., Holbrook, N.J., Cowan, T., Alexander, L., Arblaster, J.M., Power, S., 2020. Insights From CMIP6 for Australia’s Future Climate. *Earth’s Futur.* 8. <https://doi.org/10.1029/2019EF001469>
- Guo, J., Huang, G., Wang, X., Li, Y., Lin, Q., 2018. Dynamically-downscaled projections of changes in temperature extremes over China. *Clim. Dyn.* <https://doi.org/10.1007/s00382-017-3660-7>
- Harris, I., Jones, P.D., Osborn, T.J., Lister, D.H., 2014. CRU TS3.22: Climatic Research Unit (CRU) Time-Series (TS) Version 3.22 of High Resolution Gridded Data of Month-by-month Variation in Climate (Jan. 1901- Dec. 2013). *NCAS Br. Atmos. Data Centre*, 23 Sept. 2014. <https://doi.org/10.5285/18BE23F8-D252-482D-8AF9-5D6A2D40990C>

- Hersbach, H., Bell, B., Berrisford, P., Horányi, A., Sabater, J.M., Nicolas, J., Radu, R., Schepers, D., Simmons, A., Soci, C., Dee, D., 2019. Global reanalysis: goodbye ERA-Interim, hello ERA5. *ECMWF Newsl.* 17–24. <https://doi.org/10.21957/vf291hehd7>
- Hong, J.Y., Ahn, J.B., 2015. Changes of early summer precipitation in the Korean Peninsula and nearby regions based on RCP simulations. *J. Clim.* <https://doi.org/10.1175/JCLI-D-14-00504.1>
- Hong, S.Y., Noh, Y., Dudhia, J., 2006. A new vertical diffusion package with an explicit treatment of entrainment processes. *Mon. Weather Rev.* <https://doi.org/10.1175/MWR3199.1>
- Hunt, K.M.R., Turner, A.G., Shaffrey, L.C., 2020. The impacts of climate change on the winter water cycle of the western Himalaya. *Clim. Dyn.* <https://doi.org/10.1007/s00382-020-05383-3>
- Iacono, M.J., Delamere, J.S., Mlawer, E.J., Shephard, M.W., Clough, S.A., Collins, W.D., 2008. Radiative forcing by long-lived greenhouse gases: Calculations with the AER radiative transfer models. *J. Geophys. Res. Atmos.* <https://doi.org/10.1029/2008JD009944>
- Ikeda, K., Rasmussen, R., Liu, C., Newman, A., Chen, F., Barlage, M., Gutmann, E., Dudhia, J., Dai, A., Luce, C., Musselman, K., 2021. Snowfall and snowpack in the Western U.S. as captured by convection permitting climate simulations: current climate and pseudo global warming future climate. *Clim. Dyn.* <https://doi.org/10.1007/s00382-021-05805-w>
- Janjic, Z.I., 1994. The step-mountain eta coordinate model: further developments of the convection, viscous sublayer, and turbulence closure schemes. *Mon. Weather Rev.* [https://doi.org/10.1175/1520-0493\(1994\)122<0927:TSMECM>2.0.CO;2](https://doi.org/10.1175/1520-0493(1994)122<0927:TSMECM>2.0.CO;2)
- Janjić, Z.I., 2000. Comments on “Development and Evaluation of a Convection Scheme for Use in Climate Models.” *J. Atmos. Sci.*

[https://doi.org/10.1175/1520-0469\(2000\)057<3686:codaeo>2.0.co;2](https://doi.org/10.1175/1520-0469(2000)057<3686:codaeo>2.0.co;2)

Jiang, Z., Li, W., Xu, J., Li, L., 2015. Extreme precipitation indices over China in CMIP5 models. Part I: Model evaluation. *J. Clim.* 28, 8603–8619. <https://doi.org/10.1175/JCLI-D-15-0099.1>

Kadioğlu, M., Tulunay, Y., Borhan, Y., 1999. Variability of Turkish precipitation compared to El Niño events. *Geophys. Res. Lett.* 26, 1597–1600. <https://doi.org/10.1029/1999GL900305>

Kain, J.S., Kain, J., 2004. The Kain - Fritsch convective parameterization: An update. *J. Appl. Meteorol.* [https://doi.org/10.1175/1520-0450\(2004\)043<0170:TKCPAU>2.0.CO;2](https://doi.org/10.1175/1520-0450(2004)043<0170:TKCPAU>2.0.CO;2)

Karki, R., Ul Hasson, S., Gerlitz, L., Schickhoff, U., Scholten, T., Böhner, J., 2017. Quantifying the added value of convection-permitting climate simulations in complex terrain: A systematic evaluation of WRF over the Himalayas. *Earth Syst. Dyn.* <https://doi.org/10.5194/esd-8-507-2017>

Kessler, E., 1969. On the Distribution and Continuity of Water Substance in Atmospheric Circulations, in: *On the Distribution and Continuity of Water Substance in Atmospheric Circulations.* https://doi.org/10.1007/978-1-935704-36-2_1

Klein, C., Heinzeller, D., Bliefernicht, J., Kunstmann, H., 2015. Variability of West African monsoon patterns generated by a WRF multi-physics ensemble. *Clim. Dyn.* <https://doi.org/10.1007/s00382-015-2505-5>

Knutti, R., 2010. The end of model democracy? *Clim. Change.* <https://doi.org/10.1007/s10584-010-9800-2>

Knutti, R., Sedláček, J., 2013. Robustness and uncertainties in the new CMIP5 climate model projections. *Nat. Clim. Chang.* <https://doi.org/10.1038/nclimate1716>

Kouadio, K., Bastin, S., Konare, A., Ajayi, V.O., 2020. Does convection-permitting

simulate better rainfall distribution and extreme over Guinean coast and surroundings? *Clim. Dyn.* <https://doi.org/10.1007/s00382-018-4308-y>

Kutiel, H., Benaroch, Y., 2002. North Sea-Caspian pattern (NCP) - An upper level atmospheric teleconnection affecting the Eastern Mediterranean: Identification and definition. *Theor. Appl. Climatol.* 71, 17–28. <https://doi.org/10.1007/s704-002-8205-x>

Lauer, A., Zhang, C., Elison-Timm, O., Wang, Y., Hamilton, K., 2013. Downscaling of climate change in the hawaii region using CMIP5 results: On the choice of the forcing fields*. *J. Clim.* <https://doi.org/10.1175/JCLI-D-13-00126.1>

Li, L., Li, W., Jin, J., 2014. Improvements in WRF simulation skills of southeastern United States summer rainfall: physical parameterization and horizontal resolution. *Clim. Dyn.* <https://doi.org/10.1007/s00382-013-2031-2>

Li, Y., Li, Z., Zhang, Z., Chen, L., Kurkute, S., Scaff, L., Pan, X., 2019. High-resolution regional climate modeling and projection over western Canada using a weather research forecasting model with a pseudo-global warming approach. *Hydrol. Earth Syst. Sci.* <https://doi.org/10.5194/hess-23-4635-2019>

Lim, S.-Y.H., Jade, J.-O., 2006. The WRF Single-Moment 6-Class Microphysics Scheme (WSM6). *J. Korean Meteorol. Soc.*

Lin, Y.L., Farley, R.D., Orville, H.D., 1983. Bulk parameterization of the snow field in a cloud model. *J. Clim. Appl. Meteorol.* [https://doi.org/10.1175/1520-0450\(1983\)022<1065:BPOTSF>2.0.CO;2](https://doi.org/10.1175/1520-0450(1983)022<1065:BPOTSF>2.0.CO;2)

Lionello, P., Bhend, J., Buzzi, A., Della-Marta, P.M., Krichak, S.O., Jansà, A., Maheras, P., Sanna, A., Trigo, I.F., Trigo, R., 2006. Chapter 6 Cyclones in the Mediterranean region: Climatology and effects on the environment. *Dev. Earth Environ. Sci.* 4, 325–372. [https://doi.org/10.1016/S1571-9197\(06\)80009-1](https://doi.org/10.1016/S1571-9197(06)80009-1)

Liu, C., Ikeda, K., Rasmussen, R., Barlage, M., Newman, A.J., Prein, A.F., Chen, F., Chen, L., Clark, M., Dai, A., Dudhia, J., Eidhammer, T., Gochis, D., Gutmann,

- E., Kurkute, S., Li, Y., Thompson, G., Yates, D., 2017. Continental-scale convection-permitting modeling of the current and future climate of North America. *Clim. Dyn.* <https://doi.org/10.1007/s00382-016-3327-9>
- Mastrantonas, N., Herrera-Lormendez, P., Magnusson, L., Pappenberger, F., Matschullat, J., 2021. Extreme precipitation events in the Mediterranean: Spatiotemporal characteristics and connection to large-scale atmospheric flow patterns. *Int. J. Climatol.* <https://doi.org/10.1002/joc.6985>
- McSweeney, C.F., Jones, R.G., Booth, B.B.B., 2012. Selecting ensemble members to provide regional climate change information. *J. Clim.* <https://doi.org/10.1175/JCLI-D-11-00526.1>
- McSweeney, C.F., Jones, R.G., Lee, R.W., Rowell, D.P., 2015. Selecting CMIP5 GCMs for downscaling over multiple regions. *Clim. Dyn.* <https://doi.org/10.1007/s00382-014-2418-8>
- Meyer, J.D.D., Jin, J., 2017. The response of future projections of the North American monsoon when combining dynamical downscaling and bias correction of CCSM4 output. *Clim. Dyn.* <https://doi.org/10.1007/s00382-016-3352-8>
- Meyer, J.D.D., Jin, J., 2016. Bias correction of the CCSM4 for improved regional climate modeling of the North American monsoon. *Clim. Dyn.* <https://doi.org/10.1007/s00382-015-2744-5>
- Molinari, J., Dudek, M., 1992. Parameterization of convective precipitation in mesoscale numerical models: a critical review. *Mon. Weather Rev.* [https://doi.org/10.1175/1520-0493\(1992\)120<0326:POCPIM>2.0.CO;2](https://doi.org/10.1175/1520-0493(1992)120<0326:POCPIM>2.0.CO;2)
- Monerie, P.A., Wainwright, C.M., Sidibe, M., Akinsanola, A.A., 2020. Model uncertainties in climate change impacts on Sahel precipitation in ensembles of CMIP5 and CMIP6 simulations. *Clim. Dyn.* <https://doi.org/10.1007/s00382-020-05332-0>

- Morrison, H., Thompson, G., Tatarskii, V., 2009. Impact of cloud microphysics on the development of trailing stratiform precipitation in a simulated squall line: Comparison of one- and two-moment schemes. *Mon. Weather Rev.* <https://doi.org/10.1175/2008MWR2556.1>
- O'Neill, B.C., Tebaldi, C., Van Vuuren, D.P., Eyring, V., Friedlingstein, P., Hurtt, G., Knutti, R., Kriegler, E., Lamarque, J.F., Lowe, J., Meehl, G.A., Moss, R., Riahi, K., Sanderson, B.M., 2016. The Scenario Model Intercomparison Project (ScenarioMIP) for CMIP6. *Geosci. Model Dev.* 9, 3461–3482. <https://doi.org/10.5194/gmd-9-3461-2016>
- Önol, B., 2012. Effects of coastal topography on climate: High-resolution simulation with a regional climate model. *Clim. Res.* <https://doi.org/10.3354/cr01077>
- Önol, B., Semazzi, F.H.M., 2009. Regionalization of climate change simulations over the eastern Mediterranean. *J. Clim.* 22, 1944–1961. <https://doi.org/10.1175/2008JCLI1807.1>
- Overland, J.E., Wang, M., Bond, N.A., Walsh, J.E., Kattsov, V.M., Chapman, W.L., 2011. Considerations in the selection of global climate models for regional climate projections: The Arctic as a case study. *J. Clim.* <https://doi.org/10.1175/2010JCLI3462.1>
- Ozturk, T., Ceber, Z.P., Türkeş, M., Kurnaz, M.L., 2015. Projections of climate change in the Mediterranean Basin by using downscaled global climate model outputs. *Int. J. Climatol.* 35, 4276–4292. <https://doi.org/10.1002/joc.4285>
- Patrick, E., 2017. Drought characteristics and management in Central Asia and Turkey, *FAO Water Reports (FAO)*.
- Pinkerton, K.E., Rom, W.N., 2014. Global climate change and public health, *Global Climate Change and Public Health*. <https://doi.org/10.1007/978-1-4614-8417-2>
- Pleim, J.E., 2007a. A combined local and nonlocal closure model for the atmospheric boundary layer. Part II: Application and evaluation in a mesoscale

- meteorological model. *J. Appl. Meteorol. Climatol.*
<https://doi.org/10.1175/JAM2534.1>
- Pleim, J.E., 2007b. A combined local and nonlocal closure model for the atmospheric boundary layer. Part I: Model description and testing. *J. Appl. Meteorol. Climatol.* <https://doi.org/10.1175/JAM2539.1>
- Pohl, B., Crétat, J., Camberlin, P., 2011. Testing WRF capability in simulating the atmospheric water cycle over Equatorial East Africa. *Clim. Dyn.*
<https://doi.org/10.1007/s00382-011-1024-2>
- Posada-Marín, J.A., Rendón, A.M., Salazar, J.F., Mejía, J.F., Villegas, J.C., 2019. WRF downscaling improves ERA-Interim representation of precipitation around a tropical Andean valley during El Niño: implications for GCM-scale simulation of precipitation over complex terrain. *Clim. Dyn.*
<https://doi.org/10.1007/s00382-018-4403-0>
- Poupkou, A., Zanis, P., Nastos, P., Papanastasiou, D., Melas, D., Tourpali, K., Zerefos, C., 2011. Present climate trend analysis of the Etesian winds in the Aegean Sea. *Theor. Appl. Climatol.* <https://doi.org/10.1007/s00704-011-0443-7>
- Powers, J.G., Klemp, J.B., Skamarock, W.C., Davis, C.A., Dudhia, J., Gill, D.O., Coen, J.L., Gochis, D.J., Ahmadov, R., Peckham, S.E., Grell, G.A., Michalakes, J., Trahan, S., Benjamin, S.G., Alexander, C.R., Dimego, G.J., Wang, W., Schwartz, C.S., Romine, G.S., Liu, Z., Snyder, C., Chen, F., Barlage, M.J., Yu, W., Duda, M.G., 2017. The weather research and forecasting model: Overview, system efforts, and future directions. *Bull. Am. Meteorol. Soc.*
<https://doi.org/10.1175/BAMS-D-15-00308.1>
- Rasmussen, R., Liu, C., Ikeda, K., Gochis, D., Yates, D., Chen, F., Tewari, M., Barlage, M., Dudhia, J., Yu, W., Miller, K., Arsenault, K., Grubišić, V., Thompson, G., Gutmann, E., 2011. High-resolution coupled climate runoff simulations of seasonal snowfall over Colorado: A process study of current and

- warmer climate. *J. Clim.* <https://doi.org/10.1175/2010JCLI3985.1>
- Rodwell, M.J., Hoskins, B.J., 2001. Subtropical anticyclones and summer monsoons. *J. Clim.* [https://doi.org/10.1175/1520-0442\(2001\)014<3192:SAASM>2.0.CO;2](https://doi.org/10.1175/1520-0442(2001)014<3192:SAASM>2.0.CO;2)
- Rodwell, M.J., Hoskins, B.J., 1996. Monsoons and the dynamics of deserts. *Q. J. R. Meteorol. Soc.* <https://doi.org/10.1256/smsqj.53407>
- Schneider, U., Hänsel, S., Finger, P., Rustemeier, E., Ziese, M., 2022. GPCP Full Data Monthly Product Version 2022 at 0.25°: Monthly Land-Surface Precipitation from Rain-Gauges built on GTS-based and Historical Data [WWW Document]. *Glob. Precip. Climatol. Cent.* https://doi.org/10.5676/DWD_GPCP/FD_M_V2022_025
- Schröder, M., Becker, A., Dietzsch, F., Fennig, K., Graw, K., Gutenstein, M., Hollmann, R., Niedorf, A., Ziese, M., 2019. HOAPS/GPCP global daily precipitation data record with uncertainty estimates using satellite and gauge based observations (at 1.0° and 2.5°, at 0.5° only Europe) [WWW Document]. *Glob. Precip. Climatol. Cent.* https://doi.org/10.5676/DWD_CDC/HOGP_050/V002
- Sellar, A.A., Walton, J., Jones, C.G., Wood, R., Abraham, N.L., Andrejczuk, M., Andrews, M.B., Andrews, T., Archibald, A.T., de Mora, L., Dyson, H., Elkington, M., Ellis, R., Florek, P., Good, P., Gohar, L., Haddad, S., Hardiman, S.C., Hogan, E., Iwi, A., Jones, C.D., Johnson, B., Kelley, D.I., Kettleborough, J., Knight, J.R., Köhler, M.O., Kuhlbrodt, T., Liddicoat, S., Linova-Pavlova, I., Mizielinski, M.S., Morgenstern, O., Mulcahy, J., Neining, E., O'Connor, F.M., Petrie, R., Ridley, J., Rioual, J.C., Roberts, M., Robertson, E., Rumbold, S., Seddon, J., Shepherd, H., Shim, S., Stephens, A., Teixeira, J.C., Tang, Y., Williams, J., Wiltshire, A., Griffiths, P.T., 2020. Implementation of U.K. Earth System Models for CMIP6. *J. Adv. Model. Earth Syst.* 12. <https://doi.org/10.1029/2019MS001946>

- Sen, O.L., Ezber, Y., Bozkurt, D., 2019. Euro-Mediterranean climate variability in boreal winter: a potential role of the East Asian trough. *Clim. Dyn.* <https://doi.org/10.1007/s00382-018-4573-9>
- Şen, Ö.L., Gökürk, O.M., Bozkurt, D., 2015. Changing climate : a great challenge for Turkey. *J. Black Sea/Mediterranean Environ.*
- Sen, O.L., Unal, A., Bozkurt, D., Kindap, T., 2011. Temporal changes in the Euphrates and Tigris discharges and teleconnections. *Environ. Res. Lett.* <https://doi.org/10.1088/1748-9326/6/2/024012>
- Simpson, I.R., Seager, R., Shaw, T.A., Ting, M., 2015. Mediterranean summer climate and the importance of middle east topography. *J. Clim.* <https://doi.org/10.1175/JCLI-D-14-00298.1>
- Skamarock, W.C., Klemp, J.B., Dudhia, J., Gill, D.O., Barker, D.M., Wang, W., Powers, J.G., 2008. A description of the advanced research WRF version 3, NCAR Tech. Note, NCAR/TN-468+STR. Natl. Cent. Atmos. Res. Boulder, Color.
- Skamarock, W.C., Klemp, J.B., Dudhia, J., Gill, D.O., Liu, Z., Berner, J., Wang, W., Powers, J.G., Duda, M.G., Barker, D.M., Huang, X.-Y., 2019. A Description of the Advanced Research WRF Model Version 4, National Center for Atmospheric Research: Boulder, CO, USA.
- Stouffer, R.J., Eyring, V., Meehl, G.A., Bony, S., Senior, C., Stevens, B., Taylor, K.E., 2017. CMIP5 scientific gaps and recommendations for CMIP6. *Bull. Am. Meteorol. Soc.* 98, 95–105. <https://doi.org/10.1175/BAMS-D-15-00013.1>
- Taylor, K.E., Stouffer, R.J., Meehl, G.A., 2012. An overview of CMIP5 and the experiment design. *Bull. Am. Meteorol. Soc.* <https://doi.org/10.1175/BAMS-D-11-00094.1>
- Thompson, G., Field, P.R., Rasmussen, R.M., Hall, W.D., 2008. Explicit forecasts of winter precipitation using an improved bulk microphysics scheme. Part II:

- Implementation of a new snow parameterization. *Mon. Weather Rev.* <https://doi.org/10.1175/2008MWR2387.1>
- Tiedtke, M., 1989. A comprehensive mass flux scheme for cumulus parameterization in large-scale models. *Mon. Weather Rev.* [https://doi.org/10.1175/1520-0493\(1989\)117<1779:ACMFSF>2.0.CO;2](https://doi.org/10.1175/1520-0493(1989)117<1779:ACMFSF>2.0.CO;2)
- Trigo, I.F., Bigg, G.R., Davies, T.D., 2002. Climatology of cyclogenesis mechanisms in the Mediterranean. *Mon. Weather Rev.* [https://doi.org/10.1175/1520-0493\(2002\)130<0549:COCMIT>2.0.CO;2](https://doi.org/10.1175/1520-0493(2002)130<0549:COCMIT>2.0.CO;2)
- Trigo, R., Xoplaki, E., Zorita, E., Luterbacher, J., Krichak, S.O., Alpert, P., Jacobeit, J., Sáenz, J., Fernández, J., González-Rouco, F., Garcia-Herrera, R., Rodo, X., Brunetti, M., Nanni, T., Maugeri, M., Türke, M., Gimeno, L., Ribera, P., Brunet, M., Trigo, I.F., Crepon, M., Mariotti, A., 2006. Chapter 3 Relations between variability in the Mediterranean region and mid-latitude variability. *Dev. Earth Environ. Sci.* 4, 179–226. [https://doi.org/10.1016/S1571-9197\(06\)80006-6](https://doi.org/10.1016/S1571-9197(06)80006-6)
- Tuel, A., Eltahir, E.A.B., 2020. Why Is the Mediterranean a Climate Change Hot Spot? *J. Clim.* 33, 5829–5843. <https://doi.org/10.1175/JCLI-D-19-0910.1>
- Türkeş, M., Erlat, E., 2006. Influences of the North Atlantic oscillation on precipitation variability and changes in Turkey. *Nuovo Cim. della Soc. Ital. di Fis. C.* <https://doi.org/10.1393/ncc/i2005-10228-8>
- Tyrlis, E., Lelieveld, J., 2013. Climatology and dynamics of the summer Etesian winds over the eastern Mediterranean. *J. Atmos. Sci.* <https://doi.org/10.1175/JAS-D-13-035.1>
- Ulbrich, U., May, W., Li, L., Lionello, P., Pinto, J.G., Somot, S., 2006. Chapter 8 The Mediterranean climate change under global warming. *Dev. Earth Environ. Sci.* 4, 399–415. [https://doi.org/10.1016/S1571-9197\(06\)80011-X](https://doi.org/10.1016/S1571-9197(06)80011-X)
- van Vuuren, D.P., Edmonds, J.A., Kainuma, M., Riahi, K., Weyant, J., 2011. A

- special issue on the RCPs. *Clim. Change* 109, 1–4.
<https://doi.org/10.1007/s10584-011-0157-y>
- Wang, J., Kotamarthi, V.R., 2015. High-resolution dynamically downscaled projections of precipitation in the mid and late 21st century over North America. *Earth's Futur.* <https://doi.org/10.1002/2015EF000304>
- Wyser, K., Kjellström, E., Koenig, T., Martins, H., Döscher, R., 2020. Warmer climate projections in EC-Earth3-Veg: The role of changes in the greenhouse gas concentrations from CMIP5 to CMIP6. *Environ. Res. Lett.* 15.
<https://doi.org/10.1088/1748-9326/ab81c2>
- Xoplaki, E., 2002. Climate variability over the Mediterranean. PhD Thesis. University of Bern, Switzerland.
- Xoplaki, E., González-Rouco, J.F., Luterbacher, J., Wanner, H., 2004. Wet season Mediterranean precipitation variability: Influence of large-scale dynamics and trends. *Clim. Dyn.* <https://doi.org/10.1007/s00382-004-0422-0>
- Yilmaz, K.K., Yazicigil, H., 2011. Potential impacts of climate change on Turkish water resources: A review. *NATO Sci. Peace Secur. Ser. C Environ. Secur.* https://doi.org/10.1007/978-94-007-1143-3_12
- Yu, G., Wright, D.B., Li, Z., 2020. The Upper Tail of Precipitation in Convection-Permitting Regional Climate Models and Their Utility in Nonstationary Rainfall and Flood Frequency Analysis. *Earth's Futur.* <https://doi.org/10.1029/2020EF001613>
- Yucel, Ismail, Güventürk, A., Sen, O.L., 2015. Climate change impacts on snowmelt runoff for mountainous transboundary basins in eastern Turkey. *Int. J. Climatol.* 35, 215–228. <https://doi.org/10.1002/joc.3974>
- Yucel, I., Onen, A., 2014. Evaluating a mesoscale atmosphere model and a satellite-based algorithm in estimating extreme rainfall events in northwestern Turkey. *Nat. Hazards Earth Syst. Sci.* 14, 611–624. <https://doi.org/10.5194/nhess-14->

611-2014

- Yucel, I., Onen, A., Yilmaz, K.K., Gochis, D.J., 2015. Calibration and evaluation of a flood forecasting system: Utility of numerical weather prediction model, data assimilation and satellite-based rainfall. *J. Hydrol.* <https://doi.org/10.1016/j.jhydrol.2015.01.042>
- Zhang, C., Wang, Y., Hamilton, K., 2011. Improved representation of boundary layer clouds over the southeast pacific in ARW-WRF using a modified tiedtke cumulus parameterization scheme. *Mon. Weather Rev.* <https://doi.org/10.1175/MWR-D-10-05091.1>
- Zhang, H., Gao, Y., Xu, J., Xu, Y., Jiang, Y., 2019. Decomposition of future moisture flux changes over the Tibetan Plateau projected by global and regional climate models. *J. Clim.* <https://doi.org/10.1175/JCLI-D-19-0200.1>
- Zhang, Z., Colle, B.A., 2018. Impact of dynamically downscaling two CMIP5 models on the historical and future changes in winter extratropical cyclones along the East Coast of North America. *J. Clim.* <https://doi.org/10.1175/JCLI-D-18-0178.1>
- Zhao, Z., Di, P., Chen, S. hua, Avise, J., Kaduwela, A., DaMassa, J., 2020. Assessment of climate change impact over California using dynamical downscaling with a bias correction technique: method validation and analyses of summertime results. *Clim. Dyn.* <https://doi.org/10.1007/s00382-020-05200-x>
- Ziv, B., Saaroni, H., Alpert, P., 2004. The factors governing the summer regime of the eastern Mediterranean. *Int. J. Climatol.* <https://doi.org/10.1002/joc.1113>

CURRICULUM VITAE

Surname, Name: Baęçacı, Soner aęatay

EDUCATION

Degree	Institution	Year of Graduation
MS	Seluk University Civil Engineering	2018
BS	Eskşehir Osmangazi University Civil Engineering	2014
High School	Hacı Malike Mehmet Bileydi Anadolu High School, Antalya	2009

WORK EXPERIENCE

Year	Place	Enrollment
Nov 2015- Current	Karamanoęlu Mehmetbey University	Research Assistant

FOREIGN LANGUAGES

Advanced English

PUBLICATIONS

1. Baęçacı, S. ., Yucel, I., Yilmaz, M. T. (in preparation). Dynamic downscaling of the ERA5 and the CMIP6 GCM ensemble based on the pseudo-global warming method to a high resolution over the Eastern Mediterranean Black Sea region.
2. Baęçacı, S. ., Yucel, I., Duzenli, E., Yilmaz, M. T. (2021). Intercomparison of the expected change in the temperature and the precipitation retrieved from CMIP6 and CMIP5 climate projections: A Mediterranean hot spot case, Turkey. Atmospheric Research, 256, 105576.

3. Sarlak, N., Bagcaci, S. C. (2020). The Assesment of Empirical Potential Evapotranspiration Methods: A Case Study of Konya Closed Basin. *TEKNIK DERGI*, 31(1), 9755-9772.
4. Agha, O. M. A. M., Baęçacı, S. Ç., Şarлак, N. (2017). Homogeneity analysis of precipitation series in North Iraq. *IOSR Journal of Applied Geology and Geophysics*, 5(03), 57-63.
5. Bagcaci, S. C., Sarlak, N. (2019). Karaman ili potansiyel evapotranspirasyon tahmini. *Toprak Su Dergisi*, 1-8.

Conference Proceedings

1. Tokatlı Bulent, Baęçacı S.Ç., Sarlak N. (2018). Kentsel Hidrolojik Döngüde Yesil Çatı Etkisi (English Translation: The Green Roof Effect in the Urban Hydrological Cycle). 3rd International Energy and Engineering Congress (Full Text/Oral Presentation) (Paper No:4441090)
2. Baęçacı S. Ç., Sarlak N., Buyukyildiz M. (2017). The Copula Application on Drought Risk of Adana Province of Turkey. International Congress of Health and Environment (Abstract/Oral Presentation) (Paper No:3621675)
3. Baęçacı S. Ç., Sarlak N. (2017). Estimation of Potential Evapotranspiration in Karaman Province. 5th International Participation Soil and Water Resources Congress (Abstract/Oral Presentation) (Paper No:3606144)
4. Baęçacı S. Ç., Buyukyildiz M., Sarlak N., Dogan S. (2017). Drought Indices: The Case of Erzincan. ICOCEE-Cappadocia (Abstract/Oral Presentation (Paper No:3621666)

HOBBIES

Nature trip, Popular science, Literature, Music, Meditation, Documentaries